NTNU – Trondheim
Norwegian University of
Science and Technology

Recrystallisation Behaviour in Extruded Profiles of Non-Dispersoid Containing Al-Mg-Si Alloys

Christian Oen Paulsen

Preface & Acknowledgements

This master degree thesis is submitted as a part of a master programme in Materials Science and Engineering at Norwegian University of Science and Technology (NTNU). It has been submitted as the final product of Materials Technology, Master's Thesis TMT4905 with Professor Knut Marthinsen as supervisor and Post-doctorate Kai Zhang as co-supervisor. The project is a part of the COSMETEX research project financed by SAPA and The Research Council of Norway with NTNU and SINTEF as research partners.

The experimental work in this project has been done in laboratories at Department of Materials Science and Engineering. I would like to thank the lab managers, Trygve Schancke and Yingda Yu for help at the laboratory and with Scanning Electron Microscope (SEM). Thanks are due to The Research Council of Norway for providing funding along with SAPA who also provided the materials. I would especially like to thank Post-doctorate Kai Zhang for helping me analysing data, valuable discussions and always being helpful.

I would also like to express a special gratitude to my supervisor, Professor Knut Marthinsen, for sharing his knowledge and providing guidance throughout this project.

Abstract

Hot extrusion of non-dispersoid containing aluminium alloys commonly ends with a fully or partially recrystallised grain structure. However, the recrystallisation mechanisms, whether static or dynamic (taking place during deformation) are still not clarified. This report investigates extruded axisymmetric Al-Mg-Si alloys with respect to evolution in texture and microstructure in a spontaneously recrystallised material (i.e. during extrusion) and in a material which is deformed after extrusion and then recrystallised during subsequent annealing at different temperatures. Comparison between the post-heat treated and spontaneously recrystallised material have been done to characterise and identify differences in the recrystallisation behaviour and possible difference in mechanisms. Some simulations have also been conducted by the softening model *ALSOFT* to compare the experimental results with the model predictions.

The spontaneously recrystallised material showed a texture which differed from the material which recrystallised during post-extrusion heat treatment. This demonstrate a difference in recrystallisation behaviour and possibly the nucleation mechanisms. *ALSOFT* simulations seemed to give reasonable grain size results when comparing them to the experimental results in this project. However, the relative contribution from different nucleation mechanism predicted by *ALSOFT* did not comply well with experimental data.

The recrystallisation texture software *RDB_texture* was successfully implemented into Matlab. *RDB_texture* was created for rolling, therefore, some modifications to the Matlab implementation was made to make it applicable for axisymmetric extruded round bars. Most notably it is possible to choose both orthorhombic and triclinic specimen symmetry. The simulated textures were compared with experimentally found textures in order to identify input parameters giving the best agreement with experimental results.

By simulating recrystallisation texture, a set of weighting factors for different nucleation mechanisms giving the best agreement with statically recrystallised samples was determined. This was when having $\sim 65\%$ cube nucleation, $\sim 30\%$ grain boundary nucleation and some PSN. For spontaneously recrystallised samples, the best agreement was found with mainly 100% cube nucleation as the input value to the software.

Samandrag

Varmekstrudering av aluminiumslegeringer utan dispersoider resulterer vanlegvis med ein fullstendig eller delvis rekrystallisert kornstruktur. Det er imidlertidleg ikkje forstått kva for rekrystallisasjonsmekanisme som finner stad. Det har tidlegare vore indikasjonar på at dynamisk rekrystallisasjon skjer ved deformasjon ved høge temperaturar. Denne rapporten undersøker ekstruderte Al-Mg-Si legeringer med tanke på tekstur- og mikrostrukturutvikling i spontant rekrystalliserte (dvs. under ekstrudering) og i materiale som er deformert etter ekstrudering og dertetter rekrystallisert ved varmebehandling ved forskjellige temperaturar. Samanlikning mellom varmebehandla og spontant rekrystallisert materiale har blitt gjort for å karakterisere og finne forskjellar i rekrystallisasjonsoppførsel og moglege forskjellar i rekrystallisasjonsmekanismane. Simuleringar med mjukningsmodellen *ALSOFT* vart gjort for å samanlikne dei eksperimentelle resultata med modellerte resultat.

Det spontant rekrystalliserte materialet hadde ein tekstur som skilde seg frå det materialet som vart rekrystallisert ved hjelp av varmebehandling. Dette tyder på ein forskjell i rekrystalisasjonsoppførsel, det kan og tyde på at det er forskjellar i nukleasjonsmekanismane. *ALSOFT*-simuleringar gav gode prediksjoner for kornstorleik samanlikna med eksperimentelle resultat. Dei relative bidraga frå dei ulike nukleasjonsmekanismane spådd av *ALSOFT* stemde dårleg med eksperimentelle resultat.

Matlabimplenteringa av programvaren for rekrystallisasjonstekstur, *RDB_texture*, var velluka. *RDB_texture* var i utgangspunktet utvikla for valsing, derfor vart det gjennomført nokre endringar på modellen for at den skulle verte gjeldane for ekstrudering av runde profilar. Den viktigaste endringa er at det er mogleg å velge båe triklin og ortorombisk symmetry. Dei simulerte teksturane vart samanlikna med eksperimentelt funne teksturar for å finne inputverdier som gav best overeinskomst med eksperimentelle resultat.

Eit sett med vektfaktorar for dei forskjellige nukleasjonsmekanismane som gav best overeinskomst med statisk rekrystalliserte materiale, vart funne for tekstursimuleringa. Dette var ved å ha 65% kubenukleasjon, 30% korngrensenukleasjon og resten PSN. For spontant rekrystalliserte prøver var den beste overeinskomsten ved å ha tett på 100% kubenukleasjon som inputverdi til denne programvaren.

Table of Contents

List of Figures

List of Tables

List of Equations

List of Abbreviations

6463 Aluminium-Magnesium-Silicon alloy

AA3103H18 Aluminium-Manganese alloy in cold rolled condition

AA6xxx Aluminium 6000 Series

B2 Extruded sample at 450°C, spontaneously recrystallised during extrusion

BCC Body Centred Cubic Unit Cell

D04 Extruded sample at 300°C, deformed microstructure after extrusion

DRX Dynamic Recrystallisation

E24 Extruded sample at 550°C, spontaneously recrystallised during extrusion

E6 Extruded sample at 400°C, spontaneously recrystallised during extrusion

EBSD Electron Backscattering Diffraction

ED Extrusion Direction

FCC Face Centred Cubic Unit Cell

FEM Finite Element Method

GB Grain Boundary

GOF Goodness of Fit

NTNU Norwegian University of Science and Technology

ODF Orientation Distrubution Function

PF Pole Figure

PSN Particle Stimulated Nucleation

SEM Scanning Electron Microscope

T Temperature

TD Transverse Direction

Tm Melting Point Temperature

1 Introduction

1.1 Background

Aluminium is a widely used material in many industries, from transport industry with cars and aeroplanes to food preservation and home appliances. The reason for this is favourable combinations of properties like; strength to weight ratio, electrical properties, ductility, formability and corrosion properties [1]. Aluminium 6xxx series (low-alloyed Al-Mg-Si alloys) is a typical alloy used in consumer marked components, in particular, consumer electronics. In these parts the surface finish is important and to get this, these parts undergo a surface treatment, like anodising. The final anodised surface is dependent on the surface and sub-surface microstructure and texture. Today such components with desired properties and surface appearance are commonly obtained by machining the component from a block of aluminium.

1.2 Objective

This master project is closely related to the IPN research project COSMETEX funded by SAPA[1] and part address the need for a more fundamental understanding of mechanisms related to recrystallisation during extrusion of non-dispersoid containing AA6xxx series alloys, and structure-property relationships of extruded profiles of these alloys (e.g. with respect to anisotropy, strength and ductility). The overall goal for COSMETEX is to be able to extrude aluminium components intended for the consumer electronic market. By being able to extrude these parts the production rate will go up with less loss of material than today. The main challenge is the ability to produce extruded profiles with consistent (homogeneous) grain size and texture through the thickness as well as longitudinal along the extrusion length. This will be done by looking at the difference in grain structure and texture in material that recrystallised during/after extrusion and material recrystallised by heat treatment after extruding. Any differences may indicate that recrystallisation is driven by different mechanisms in the different cases. This master project contributes to the overall research goal of the COSMETEX project towards a better understanding of the microstructure development in non-dispersoid containing extruded aluminium alloys.

The master project will be a continuation and follow-up to the specialisation project TMT4500. The objective is to understand and hopefully being able to model the recrystallisation behaviour during/after extrusion with a special

---

[1]Next generation extrusion technology for high-performance applications - COSMETEX

focus on the texture evolution of an extruded profile. The work will combine detailed experimental characterisation and modelling/simulations based on available software for recrystallisation texture calculations (*RDB_texture* (O. Engler, R&D Hydro Bonn)) and recrystallisation kinetics and grain structure (*ALSOFT*):

The specific objectives of this master thesis, are listed below:

1. Careful experimental characterisation (by SEM/EBSD) of the nucleation of recrystallisation and recrystallisation evolution (kinetics) with focus on orientation distribution and density of recrystallisation nucleation of a selection of extruded and extruded/annealed samples.

2. Identify possible differences in recrystallised microstructure and texture of extruded profiles which spontaneously recrystallised during/after extrusion and extruded profiles which are recrystallised during post extrusion annealing.

3. Provide experimental data (from post-extrusion annealing) of recrystallisation kinetics and recrystallised grain size and texture which can be used to validate and/or further develop the softening model *ALSOFT*.

4. Implement and adapt an in-house code for the recrystallisation texture software *RDB_texture* in Matlab.

5. The *RDB_texture* software is developed for orthorhombic symmetry (sheet rolling) and needs to be modified to applicable to the axisymmetry of extruded round bars used in the COSMETEX project.

2 Background Theory

2.1 Properties of Aluminium 6000 Serie Alloys

AA6xxx series are aluminium-magnesium-silicon alloys that can be precipitation hardened, where the precipitated particles are of the Mg_xSi_y type. This alloy has good surface appearance and responds well on surface treatments as anodising [2]. The alloying elements will effect the maximum extrusion speed; if the alloy is extruded to fast the surface may tear. A higher content of Si or Mg will reduce the maximum extrusion speed before tearing [2]. On the other hand, it is desirable to have Mg and Si particles since they increase the strength. Al-Mg-Si alloys are known to have good corrosion properties in both natural and artificial environments and the most used aluminium alloy in extruded profiles, due to the alloys high formability. By adding 0.5-0.7% Mn or 0.1-0.3% Cr the material get grain refined, 0.3-0.9% Cu increases the strength, but if the additions exceed 0.5% Cu the corrosion resistance will be reduced [3]. Mn and Cr along with Zr may be added to the material to form dispersoids. These dispersoids influence the nucleation and recrystallisation behaviour of the material and may even prevent recrystallisation. Dispersoids are small particles and during grain growth these particles may pin and retard the movement of grain boundaries [4].

Mn containing dispersoids are formed during the homogenisation heat treatment and the shape of these are affected by the heating rate [5, 6]. Rapid heating gives needled-shaped dispersoids, heterogeneously distributed, whilst slower heating gives more homogeneously distributed spherically shaped dispersoids. The edge regions of needle-shaped dispersoids are shown to be preferential sites for nucleating new recrystallised grains [5].

2.2 Extrusion

Extrusion of metal is a process where a solid block of metal is forced through a die, changing the metals' shape and microstructure [7]. Extrusion takes place at elevated temperatures and 90% of all extruded aluminium is Al-Mg-Si alloys [2]. Before extrusion, the billet is preheated to the desired extrusion temperature and then, soon after, the billet is forced through the die. The material goes from a large cross-section area to a much smaller one in a very short time. A typical processing route for extruded aluminium is shown in Figure 2.1. Here the temperature profile is also shown. During the homogenisation process casting defects as trapped gas bubbles and microsegregation are being removed [8]. After the extrusion and forming the final step is age-

ing. Here the final product is held at a temperature to precipitate second phase particles. This is done to provide strength [7, 8].
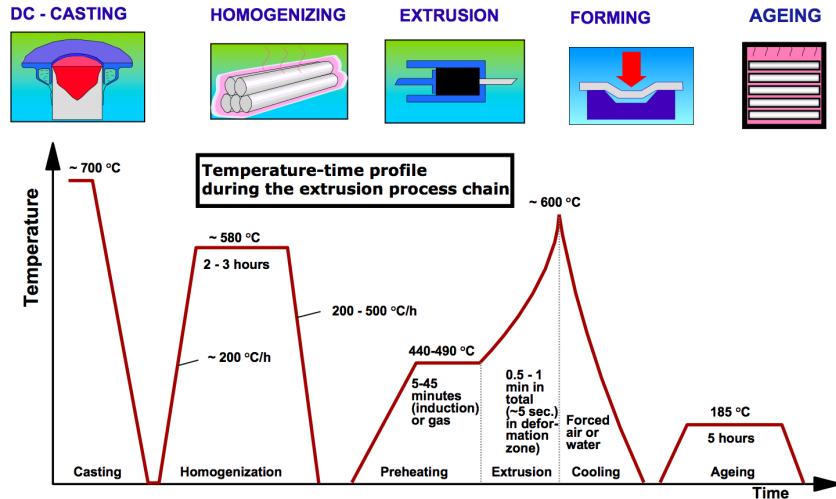
Figure 2.1: Typical production process for an extruded aluminium alloy. The curve shows the temperature profile during the processing route. The figure is taken from lecture notes in TMT4260, NTNU 2014.
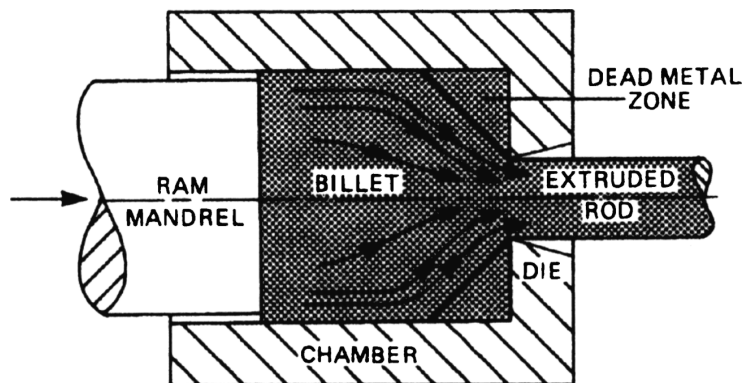
Figure 2.2: Illustration of the extrusion process. The figure is taken from Verlinden et. al (2007) [9].

When the block of metal goes through the die, a lot of deformation is introduced and if the temperature is high enough, the deformed microstructure may start to recrystallise. Figure 2.2 illustrates the extrusion process. In Figure 2.3 it is possible to see an example on how the grain structure evolves during the extrusion process. Here it possible to see the dead zone building

up in the corner of the chamber and how the metal flows through the die and starts recrystallising soon after exiting the die. In the enlarged part of the extruded rod, it can be seen that the deformed fibrous structure continues into the extrusion rod for a short distance. Then new recrystallised grains start to form.
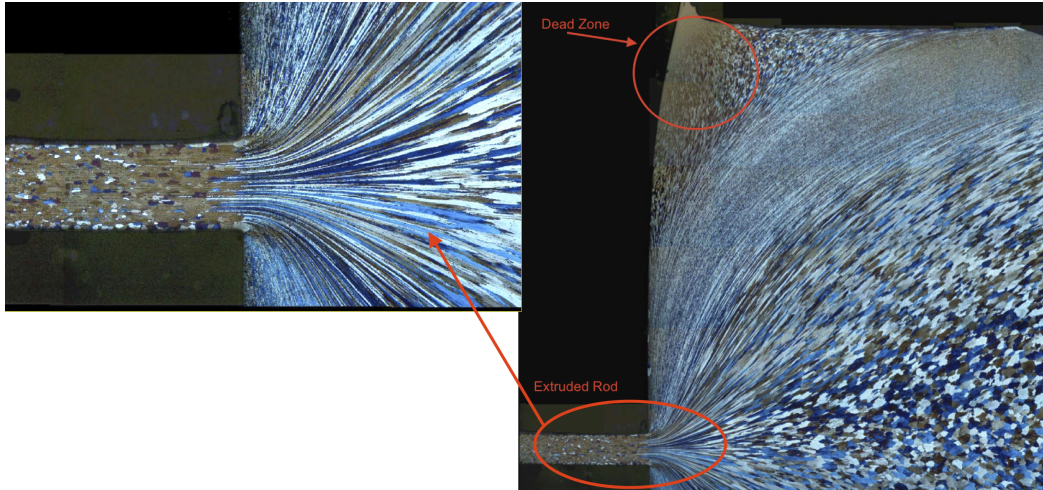
Figure 2.3: Grain structure evlolution during the extrusion process. The dead zone and extruded rod are labelled in the figure, with an enlargement of the extruded rod. The Figure is adapted from lecture notes in TMT4260, NTNU 2014.

As described in Section 2.1, different alloying elements affect the recrystallised microstructure. An extruded AA6005 alloy with different additions of Mn and Cr can be seen in Figure 2.4. Here the retardation effect of Mn and Cr on recrystallisation is illustrated. When only a small amount of Mn is added there is not a large difference, but when both Mn and Cr are being added (Figure 2.4(c)) the grain structure changes quite significantly with only a few very large recrystallised grains in the sub-surface region and the area in the middle of the profile is not recrystallised at all.
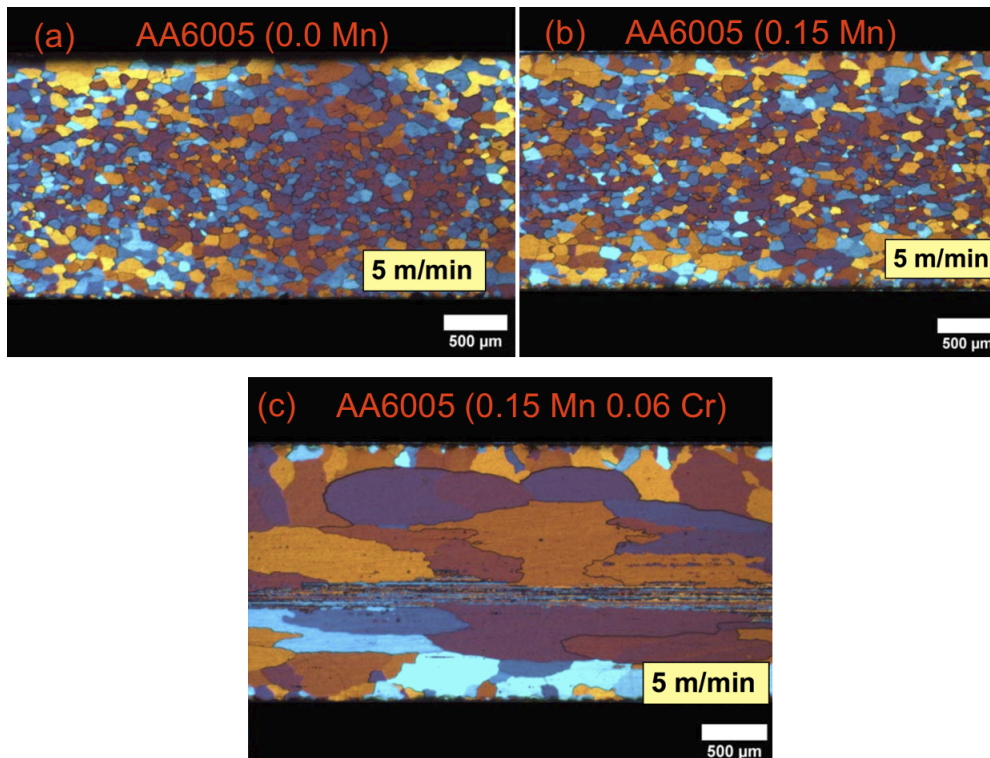
Figure 2.4: Grain structure of extruded AA6000 with different additions of Mn and Cr. In (a) there are no Mn or Cr added, (b) 0.15 Mn have been added, (c) 0.15 Mn and 0.06 Cr have been added. The Figure is adapted from lecture notes in TMT4260, NTNU 2014.

The force required to feed the billet through the die is dependent on alloying elements, ram speed, temperature and die shape [2, 7]. In Figure 2.5 the extrusion pressure is plotted against ram travel. The extrusion pressure is force divided by the cross-sectional area of the billet. The initial rise in the graph is due to the compression of the billet. Then metal starts to flow through the die at the maximum pressure, the breakthrough pressure. After this, the pressure required decreases with decreasing billet length left in the container. At the end of the stroke, the pressure builds up rapidly because then the billet is thin and the metal has to flow radially to exit the die. This leaves a lot of defects in this part of the extruded profile and the extrusion is often stopped before this happens [7].
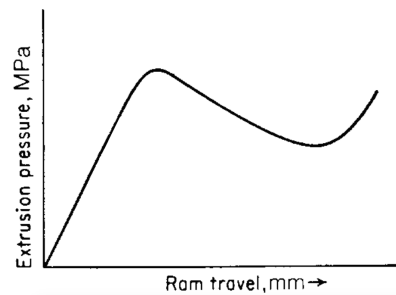
Figure 2.5: Extrusion pressure vs. ram travel. The figure is adapted from Dieter (1986) [7].

The deformation of the billet is more or less uniform except close to the die, here the material is exposed to a high strain-rate and after exiting the die strain-rate is zero. In the corner of the die a "dead zone" builds up, this region is labelled in Figure 2.2 and 2.3. This happens since the metal in the centre flows easier than the metal closer to the container surface and, therefore, is held back by friction and also the die exit will be at the centre of the billet. When the ram gets to the built up dead zone the pressure starts to build up [7, 10].

2.3 Microstructure Development

When a billet is extruded at a high enough temperature and the profile exiting the die is recrystallised, the sequence of events is not clear. There is an ongoing debate on whether the material deforms and recrystallise all at the same time, in no particular order, or if the deformation occur first and then the material spontaneously recrystallise after the deformation is completed and the material has left the die. The first case is named "Dynamic Recrystallisation" and the latter "Static Recrystallisation".

2.3.1 Static Recrystallisation

After a material is deformed, for instance during extrusion at low temperature, it contains a lot of stored energy [4]. In order to release this energy, the recovery process starts and dislocations begin to annihilate. The different steps of recovery can be seen in Figure 2.6. The next step, or more precisely; an alternative reaction in releasing the stored energy, is by nucleation and growth of new strain-free grains to obtain a recrystallised microstructure. Recrystallisation and recovery are competing processes and when recrystallisation starts, the deformed substructure is consumed and the driving force for recovery is gone. During heat treating, there are in general three different processes leading to change in microstructure after deformation [9]:
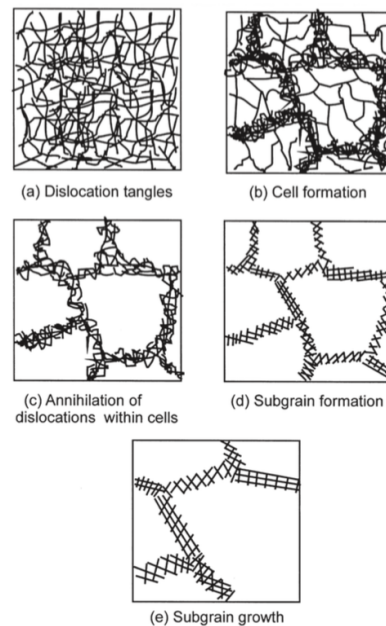
Figure 2.6: The different stages of recovery. The figure is taken from Humphreys & Hatherly (2002) [4].

- *Recovery*; Related to releasing of stored energy and movement of dislocations.

- *Recrystallisation*; Related to releasing of stored energy and movement of high angle grain boundaries.

- *Grain Growth*; Reducing surface energy and movement of high angle grain boundaries.

These processes are illustrated in Figure 2.7. In Figure 2.7(a) a material in the deformed state is shown and this will be the equivalent to the dislocation tangles in Figure 2.6(a). After sub-grains have formed during the recovery (Figure 2.7(b)), new dislocation-free grains starts to form within the deformed/recovered structure (Figure 2.7(c)). These grow at the expense of old grains and a new recrystallised grain structure is formed (Figure 2.7(d)). If the material is annealed further this may lead to grain growth (Figure 2.7(e)) [4].
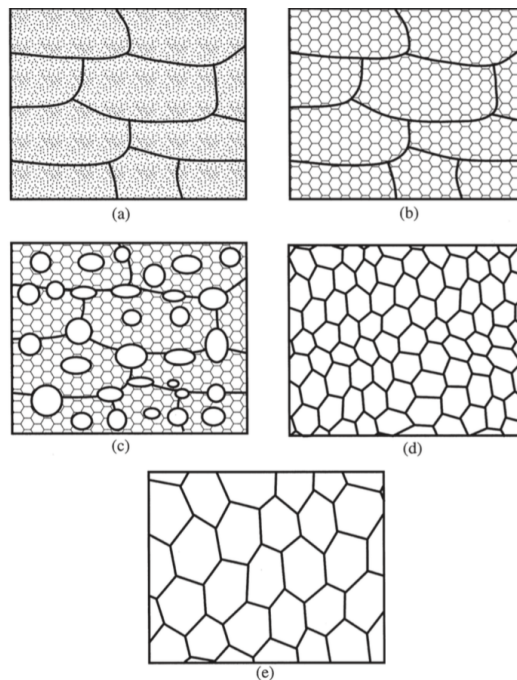
Figure 2.7: The different steps of the main annealing process. (a) deformed state, (b) after recovery, (c) partially recrystallised structure, (d) fully recrystallised structure and (e) after some grain growth. The figure is adapted from Humphreys & Hatherly (2002) [4].

There are several mechanisms for the nucleation of recrystallising and the formation of a new grain structure. One option is new grains nucleating on old grain boundaries which have a preferred orientation similar to the deformed grain and give rise to a texture similar to the deformation texture, only weaker [4]. Preferred orientations of grains are called texture. It is possible for recrystallised grains to nucleate in the deformation zone around non-deformable particles (PSN, particle stimulated nucleation) [4]. An illustration of PSN is shown in Figure 2.8, which shows iron with oxide inclusions and where recrystallisation has started from these oxide particles. The texture of PSN recrystallised grains will, in general, be different than recrystallised grains from grain boundary nucleation [4]. Typically PSN gives rise to a weak random texture. Cube texture is a nucleation component during recrystallisation of deformed aluminium and comes from band-like structures, called 'cube bands', which are present in the deformed structure [11, 12].
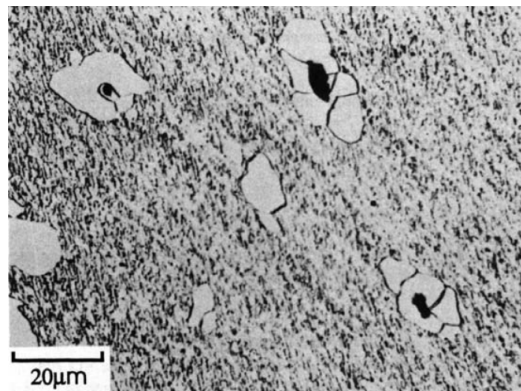
Figure 2.8: Particle stimulated nucleation of recrystallisation. The figure is taken from Leslie et. al (1963) [13].

2.3.2 Dynamic Recovery & Recrystallisation

In materials with a high stacking fault energy, like Al, α-iron and most BCC metals, dynamic recovery may occur. This is exemplified in Figure 2.9(a). The rise in stress at the start of the curve is a result of deformation and work hardening, dislocation multiplication. At this stage a microstructure of low angle grain boundaries and sub-grains develops. Eventually the dislocation multiplication is balanced by recovery i.e. dislocation annihilation and work hardening and recovery reach an equilibrium and a steady-state is reached and where dislocation multiplication and annihilation are balanced upon further straining, as seen in Figure 2.9(a) [4, 7]. At elevated temperatures, T > $0.5T_m$, dislocations in these materials can move relatively easy with cross slip,

climb and unpin at nodes in this temperature region. The strain rate and temperature are often incorporated into one parameter, the Zener-Holloman parameter, this is given in Equation 2.1 [4].

$$Z = \dot{\varepsilon} \exp\left(\frac{Q}{RT}\right) \tag{2.1}$$

Here T is temperature, R the universal gas constant, Q the activation energy and $\dot{\varepsilon}$ the strain rate. This parameter is particularly useful because it can correlate stress, temperature and strain rate during hot-working. During this process strain rate and temperature generally are known and the stress may not be measurable [4].

Dynamic recrystallisation (DRX) typically occurs in materials with low, medium stacking fault energy, like Cu, Ni and γ-iron [4]. In these materials, recovery is suppressed (due to the formation of stacking faults, which prevents cross-slip) and very little dislocation annihilation take place before the density of dislocations is high enough for recrystallisation to start. The result is the peak in Figure 2.9(b). After this peak the material recrystallises and the dislocation density goes down and the stress needed to continue the deformation levels out. The grain size in dynamical recrystallised metal

Figure 2.9: The stress-strain-curve for a hot-worked metal showing (a) dynamic recovery; (b) dynamic recrystallisation. The figure is taken from Dieter (1986) [7].

is directly correlated to the strain rate, this makes it possible to adjust the recrystallised grain size with strain rate [8].

Since aluminium is a high stacking fault material, DRX is not supposed to take place. Still it has been reported that DRX also can take place during hot deformation of aluminium alloys [14–16]. However, it is still not clear to which extent and under which conditions it may occur. In particular, which role it plays for the alloy and extrusion conditions considered in this project.

2.4 Texture

Texture is the tendency of grains in a material to orient themselves in certain directions, which may give rise to anisotropic properties, e.g. strength and ductility. A possible consequence of anisotropy is exemplified by the drawn cup shown in Figure 2.10. The cup to the right has a strong cube texture resulting in the material deforming differently in different directions.

Figure 2.10: Effect of earing on deep drawn cups, strong texture to the right and weak to the left. The figure is taken from aluMATTER [17].

A common procedure to present texture data is by pole figures [4]. Pole figures provides a representation on how the grains are oriented in the sample, the figure is created by stereographic projections as shown in Figure 2.11. When the material is deformed by extrusion or wire drawing, the deformation occurs along a single axis and an inverse pole figure are often used to represent the texture [4]. It is possible to represent the pole figure with the individual points going through the crystallographic plane or by having contour lines indicating the density of points, as seen in Figure 2.11d) and e) respectively.

Deformation texture is the result of two main factors, i.e. geometrical constraints (e.g. plane strain, uniaxial tension (like wire drawing)) and crystallographic constraints [8]. The latter refers to the number and type of slip systems in the material (12 in aluminium). Other factors that can play a role are the temperature at which the deformation occurs and the original texture present. In Figure 2.12 an example of (100) and (111) pole figures of an axisymmetric circular extruded profile is shown. In the (100) pole figure, two symmetric <111>-fibres can be seen, along with a <100>-fibre (labelled in the figure). These texture components are present as bands because of the rotational symmetry (around ED; vertical axis in Figure 2.12) in the extruded profile. Without this particular rotational symmetry these components would be presented as individual maxima like the ones in Figure 2.11e), but here they are "smeared" throughout the figure due to the rotational symmetry around the A1 axis. The same is the case in the (111) pole figure, but here <111> and <100> can be seen as two "parallel" fibres. The pole figures in Figure 2.12 contain two texture components and these have the typical appearance of an extruded axisymmetric circular profile.
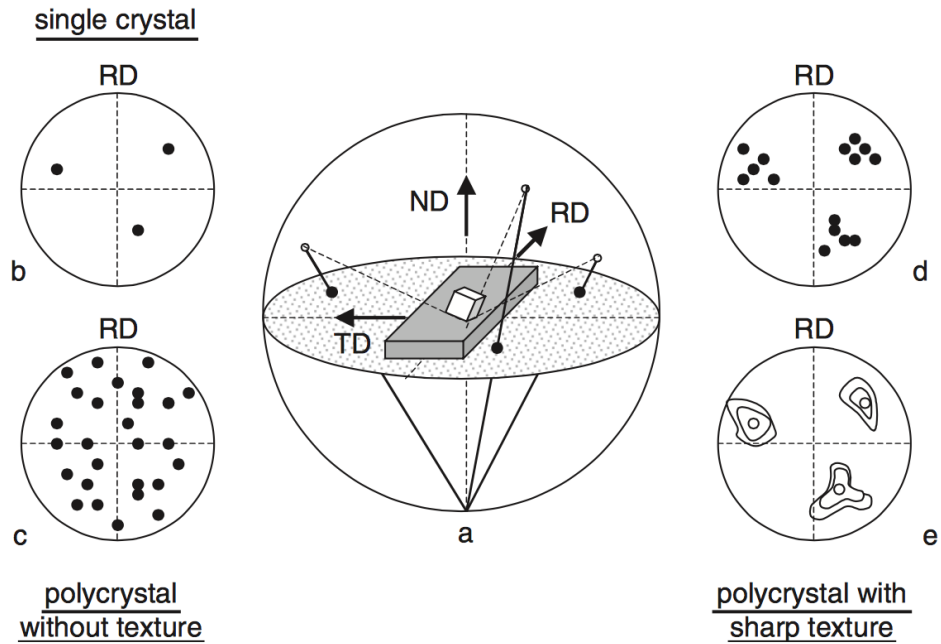
Figure 2.11: Construction of a (100) pole figure. (a) Stereographic projection of the (100) poles; (b) projection of the (100) poles of one grain on the equatorial plane; (c) projection of the (100) poles of a polycrystal; (d) projection of the (100) poles of a textured polycrystal; (e) contour map of the (100) pole density distribution. The figure is taken from Verlinden et. al (2007) [18].
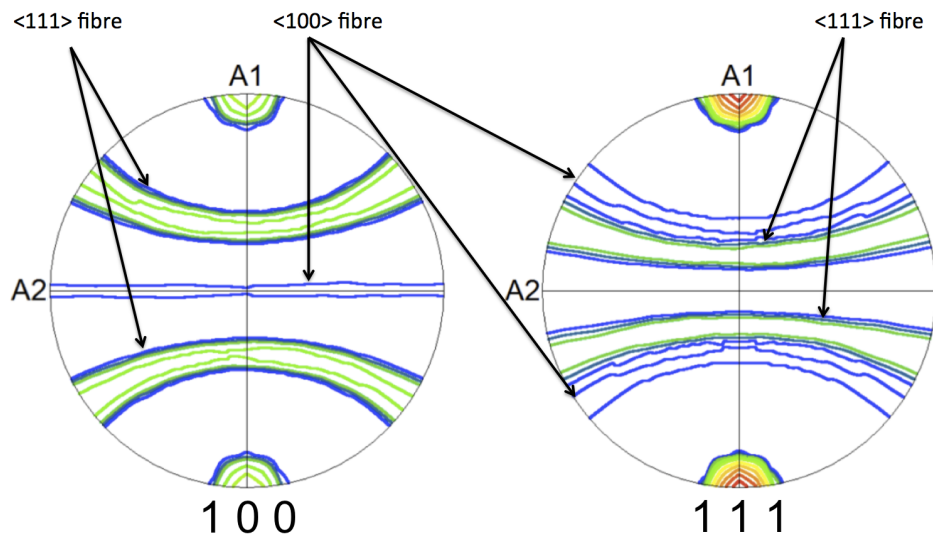
Figure 2.12: (100) and (111) pole figures, courtesy of Kai Zhang.

Another way of representing texture data is the Orientation Distribution Function (ODF). These figures are 2-dimensional representations of the 3-dimensional Euler space. This is defined by three angles, the most commonly used notation is the one suggested by Bunge (1965 & 1982) [19, 20]; φ_1, Φ and φ_2. With ODF's, an orientation is represented in the 3-dimensional coordinate system with φ_1, Φ and φ_2 as axes, this is the Euler space. Alongside pole figures, ODF's are the most commonly used method for presenting texture data. In Figure 2.13 the Euler space is displayed with an orientation g. Each orientation g corresponds to a point in the Euler space whose coordinates are given by the three Euler angles φ_1, Φ and φ_2 describing the orientation. The way to obtain and calculate this g is described in Engler & Randle (2009) [21]. This g links the Euler angles to each point in the Euler space. An ODF is a graphical representation of different cross-sections in the three-dimensional orientation space defined by the Euler angles.
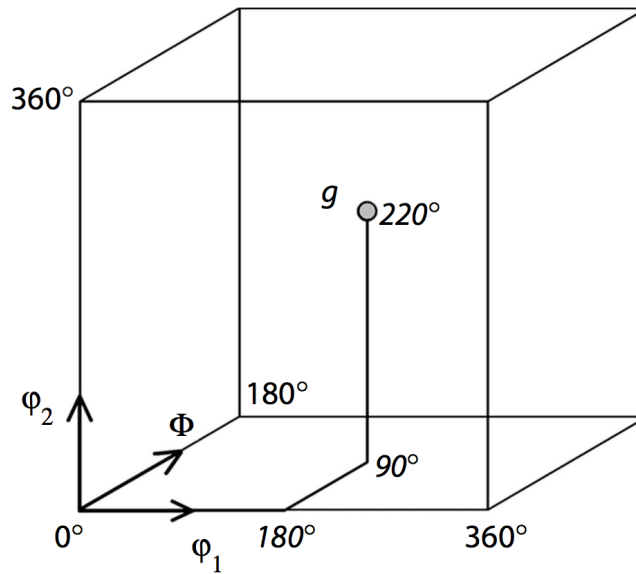
Figure 2.13: Representation of orientations in a the Euler space. Figure taken from Engler & Randle (2009) [21].

Euler angles are defined in the range of $0° \leq \varphi_1$, $\varphi_2 \leq 360°$ and $0° \leq \Phi \leq 180°$, which is the maximum size of the Euler space. If there is any symmetry in the specimen, will this reduce this range due to an equivalent description of a given orientation [22]. A rolled component will have an orthorhombic sample symmetry, here the range will be $0° \leq \varphi_1$, Φ, $\varphi_2 \leq 90°$ [22]. For extruded components with triclinic sample symmetry the range will be; $0° \leq \Phi$, φ_2

$\leq 90°$ and $0°\leq \varphi_1 \leq 360°$ [22]. In Figure 2.14 an ODF plot can be seen with strong cube texture, the range of this plot is $0°\leq \Phi$, $\varphi_2 \leq 90°$ and $0°\leq \varphi_1 \leq 360°$, i.e. it has triclinic sample symmetry.
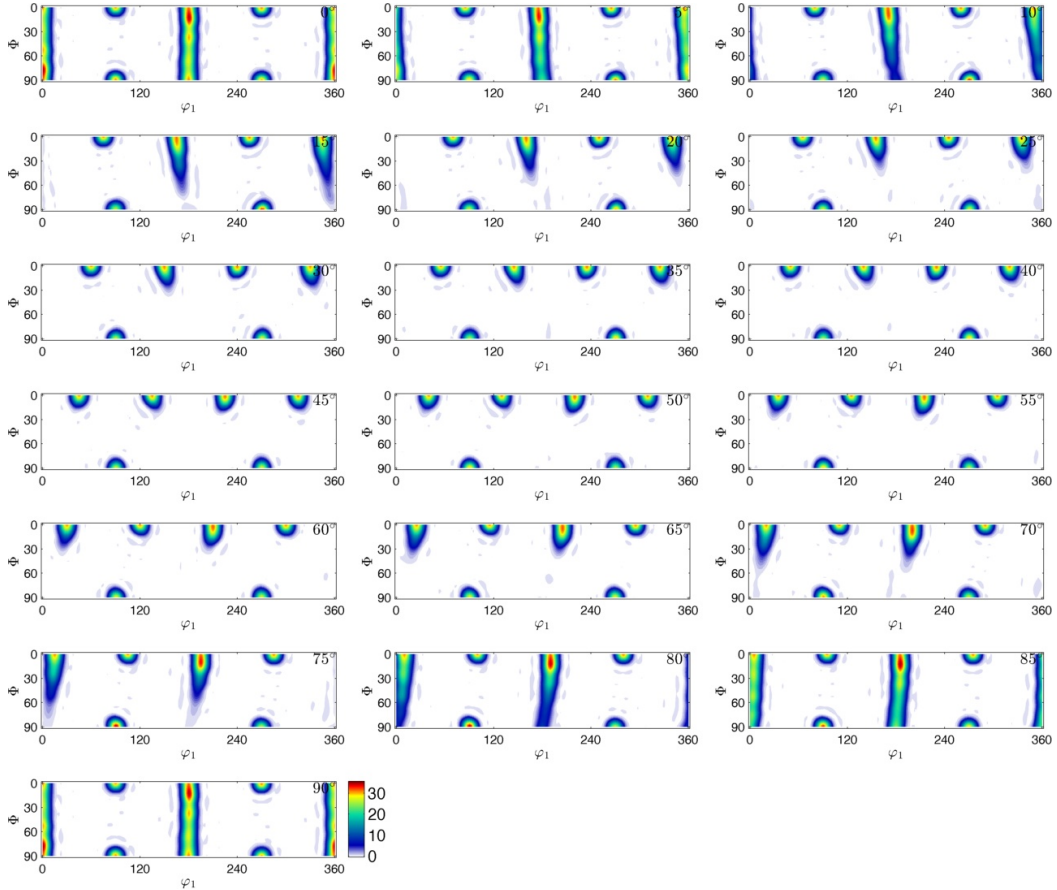
Figure 2.14: ODF with strong cube texture.

ODF's are very useful for comparing textures between two materials, this can be done by using the goodness of fit (GOF) Equation 2.2 [21]. In this equation, a lower number will indicate a better fit, with zero as the lowest possible number and then the two ODF's are identical. This is typically desirable when comparing simulated and experimentally found data.

$$\frac{\int \left[f_{sim}(g) - f_{\exp}(g)\right]^2 dg}{\int \left[f_{\exp}(g)\right]^2 dg} \qquad (2.2)$$

With dg being

14

$$dg = \frac{1}{8\pi^2} \sin \Phi d\varphi_1 d\Phi d\varphi_2 \qquad (2.3)$$

2.5   Electron Backscatter Diffraction

In a scanning electron microscope it is possible to obtain a diffraction pattern from the near material surface, this is done by the electron backscattering diffraction (EBSD) technique. An electron beam is "shot" onto a tilted specimen. Primary electrons from the electron beam diffracted will exit the specimen surface and hit a screen and generate the diffraction pattern [23]. In Figure 2.15 a sketch of the electron path can be seen. The diffraction pattern obtained can be interpreted to determine the orientation of the grains. After the pattern is retrieved a software is needed to index them before further analyses can be conducted.
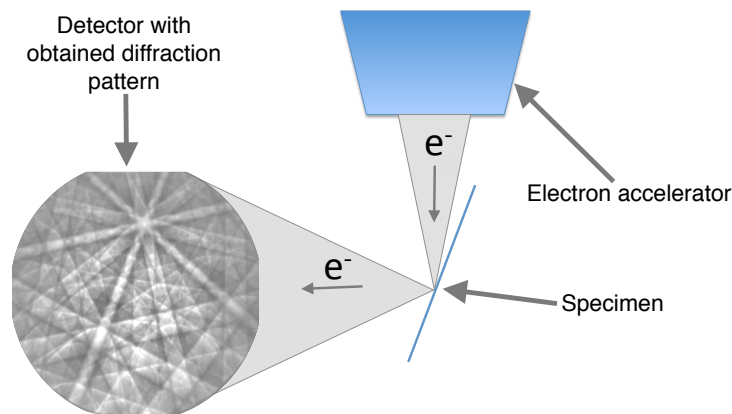
Figure 2.15: How the electron beam hits the specimen and obtains the diffraction pattern. Based on a figure from lecture notes in TMT4300, NTNU 2013.

It has previously been shown that analysing using EBSD compared to optical microscope gives different result when the same area is analysed [24]. This is due to the fact that EBSD better reads data from small grains. The settings in the SEM and EBSD software will also affect the quantifiable data. First when the settings are all the same the results are comparable to each other.

For the diffraction pattern to be visible, proper sample preparation is important. All the near surface deformation zones have to be removed to see the "real" microstructure. When grinding and polishing, a small deformation zone is introduced into the surface layer. A method for clearing the

final deformation layer after polishing is electropolishing. This is a technique where the metal is connected to an anode and immersed into an electrolyte and current runs through the sample and the metal starts dissolving at the surface. It works like reversed plating and is an active, controlled corrosion process [25].

2.6 Surface Finish & Microstructure

An important surface finishing method is anodising. Aluminium is the material most associated with this practice [26]. Anodising is done for several reasons, in general, to increase surface, corrosion or mechanical properties or enhance the decorative appearance. The microstructure and texture of the surface structure influence the final outcome of the anodised surface. Anodising has a different effect on differently oriented grains. The cosmetic appearance of the final anodised product will be dependent on the texture. When extruding, it is a challenge to maintain the same microstructure along the length of the profile and getting consistent results, especially at the charge welds, i.e. at the boundary region where the material from successive extrusion bolts "overlap". Extruded profiles being anodised will then have different appearance along the profile length.

2.7 Modelling

2.7.1 *ALSOFT*

ALSOFT is a model for simulation of the softening behaviour of deformed Al-alloys. It accounts for the combined effect of recovery and recrystallisation during annealing. The reader is referred to the sources listed and Appendix A for further detail on the models main concepts and mathematical implementation [27–32]. In the following, basic concepts in terms of main assumptions and equations are presented.

In *ALSOFT*, the microstructure is characterised by an average sub-grain size, δ, and dislocation density, ρ, inside the sub-grains. The driving pressure for recrystallising is due to dislocations within the cells and sub-grain size. This is calculated according to Equation 2.4:

$$P_D(t) = \alpha \frac{\gamma_{SB}}{\delta(t)} + \frac{1}{2} G b^2 \rho(t) \tag{2.4}$$

Here α is a constant, γ_{SB} is the sub-grain boundary energy, G is shear modulus and b is Burgers vector ($b = 0.286$ nm in aluminium).

16

ALSOFT was primarily developed for rolling conditions i.e. plane strain deformation. For these conditions the following nucleation mechanisms have been identified; PSN, nucleation from old grain boundaries and nucleation from retained cube bands. These are the ones considered in *ALSOFT* [27, 33], with the total density of nucleation sites given in Equation 2.5:

$$N_{Tot} = N_{Cube} + N_{GB} + N_{PSN} \tag{2.5}$$

The density of the different nucleation sites is given by Equation 2.6, 2.7 and 2.8:

$$N_{Cube} = \overline{\delta}_C A(\varepsilon) R_s (1 - R_c) S_C^* \tag{2.6}$$

$\overline{\delta}_C$ is the average cube sub-grain size, $A(\varepsilon)$ is the surface area per unit volume of cube grains of initial grain size $\overline{D}$, undergone a deformation of an effective strain ε. R_s is the fraction cube bands surrounded by the {123}<634> deformation texture component and S_c^* is the density of the sub-grains inside the cube regions with diameters larger than a critical value. $(1 - R_c)$ is included because a cube band with another cube grain as a neighbour will not provide nuclei [27, 30].

$$N_{GB} = 2C_{GB} \left(1 - R_c\right) S_{GB}^* A(\varepsilon) \tag{2.7}$$

Here the different factors have the corresponding meaning as in Equation 2.6 with C_{GB} is a modelling constant which determines the strength of the grain boundary nucleation [27, 30].

$$N_{PSN} = C_{PSN} N_0 \exp\left(-\frac{4\gamma_{GB} L}{P_D - P_Z}\right) \tag{2.8}$$

C_{PSN} is a constant and P_Z is the Zener pressure, a resistance towards recrystallisation due to the presence of dispersoids [34]. $N_0 = H/L$, where H and L are characteristic distribution parameters in large sized particles distribution [27].

The recrystallisation kinetics is based on the assumption of site saturation nucleation kinetics and random distribution of nucleation sites, thus the following transformation equation is given:

$$\frac{dX(t)}{dt} = (1 - X(t)) N_{Tot} 4\pi \cdot r(t)^2 \cdot G(t) \tag{2.9}$$

X(t) is fraction recrystallised after an annealing time t, r(t) is the size of recrystallised grains and G(t) is their growth rate, given by Equation 2.10. The growth rate and size of recrystallised grains are related by Equation 2.11.

$$G(t) = M(t) \cdot (P_D(t) - P_Z(t)) \tag{2.10}$$

$$\frac{dr}{dt} = G(t) \tag{2.11}$$

M(t) is given by Equation 2.12 and is the mobility of boundaries (assumed to be independent of orientations).

$$M(t) = \frac{M_0}{c_{ss}^{eff} kT} \exp\left(-\frac{U_{RX}}{RT}\right) \tag{2.12}$$

U_{RX} is an activation energy, c_{ss}^{eff} is an effective solid solution level (weighted sum of different solute [32]) and accounts for solute drag through an inversely proportional with the boundary mobility. After the fraction recrystallised is determined and the total density of nucleation sites is found, the grain size in the transformed regions can be found by using Equation 2.13.

$$D = (X/N_{Tot})^{1/3} \tag{2.13}$$

These equations give the basis for recrystallisation behaviour in *ALSOFT*, with the assumptions given in the above text. It has been indicated in previous work; however, that the model requires further developments, especially with the presence of dispersoids [30]. Since it is also originally developed for rolling and it is not clear how well it applies for extrusion, especially in the near surface region where the material experience a significant shear deformation and the nucleation mechanisms may be different from plane strain conditions.

2.7.2 *ALFLOW*

ALFLOW can be used to obtain some of the values used as input for *AL-SOFT* simulations. Extensive presentations of the work hardening part of the model are given elsewhere [35–37] and only brief descriptions of the analytical expressions constituting the core elements of this submodel is presented in the following, with the emphasis on flow stress and microstructure evolution equations.

The flow stress, τ, at a constant microstructure is commonly defined in terms of a thermal component, τ_t, and an athermal component, $\hat{\tau}_a$, so that $\tau = \tau_t + \hat{\tau}_a$. The thermal component is due to short-range interactions between mobile dislocations and intersecting stored ones, dragging of jogs and elements in solid solution. The athermal component characterises the rate and temperature independent interaction of dislocations with long-range barriers. In the treatments by Nes and co-workers [36–38] the stress required for dislocation migration is written in Equation 2.14.

$$\tau = \tau_t + \hat{\tau}_p + \alpha_1 Gb\sqrt{\rho_i} + \alpha_2 Gb(1/\Delta^*) \tag{2.14}$$

Where G is the shear modulus, b the magnitude of the Burgers vector, $\hat{\tau}_p$ is the flow stress contribution due to non-deformable particles (Orowan by-pass stress; $\hat{\tau}_p = Gb/\lambda$, where λ is the particle spacing), ρ_i is the dislocation density in the sub-grain interior, and Δ^* is the separation of boundaries, counting all type of boundaries. The parameters α_1 and α_2 are constants (typical values 0.3 and 2, respectively). This flow-stress expression rests on the classical works by Seeger (1957) [39] and Friedel (1964) [40] where the major effect due to the stored dislocation sub-structure (in Seeger's and Friedel's treatments the Frank network) on the flow stress is assumed to be of long range type, i.e. athermal in nature.

The present model treats the microstructure evolution during plastic deformation in terms of three parameters; the cell size, δ, the dislocation density within cells, ρ_i, and the sub-boundaries misorientation, φ. It follows that an analytical description will require three evolution equations, i.e. one for each microstructural element. On the basis of previous treatments [36, 37] these evolution equations can be written in compact form as follows:

$$\frac{d\rho_i}{d\gamma} = \frac{1}{(1 + f(q_b^2 - 1))}\frac{2}{bL_{eff}} - \frac{\rho_i \nu_i}{\dot{\gamma}} \tag{2.15}$$

$$\frac{d\delta}{d\gamma} = -\frac{2\delta^2 \rho_i}{\kappa_0 \varphi}\frac{SL^2}{L_{eff}} + \frac{b\nu_\delta}{\dot{\gamma}} \tag{2.16}$$

$$\frac{d\varphi}{d\gamma} = f\left(\rho_i, \delta, \varphi\right) \tag{2.17}$$

Equation 2.15 and 2.16 reflect the combined result of athermal storage of dislocations (first term at the right side in these equations) and their dynamic

recovery (second term). In these storage terms, L and L_{eff}, refer, respectively, to the slip-length in a pure metal single crystal and the effective one in a pure metal or alloy polycrystal. S is a cell/sub-boundary storage parameter. $\dot{\gamma}$ is the strain rate, ν is the dipole collapse frequency, κ_0 is a geometric constant (approximately equal to 3) and q_b is a scaling parameter. Solving Equation 2.15 and 2.16 for a given deformation history in terms of strain rate, temperature and accumulated strain (e.g. provided by FEM-simulations) provides the sub-structure in the form of cell interior dislocation density and sub-grain size at the end of deformation, from which the stored energy/driving force for recrystallisation then can be calculated by Equation 2.4.

The equations given here forms the basis for the evolution in microstructure for *ALFLOW*. In Appendix B a more detail description of the main concepts and mathematical expressions used have been listed. The results from these can be used as input values for *ALSOFT* simulations to predict the recrystallisation kinetics and recrystallised grain size.

2.7.3 Recrystallisation Texture Simulations

The model implemented in the present work is a continuation of Engler's work (1997 & 1999) [41, 42], including some further developments. A schematic of the basis for Engler's model, *RDB_texture*, is shown in figure 2.16.
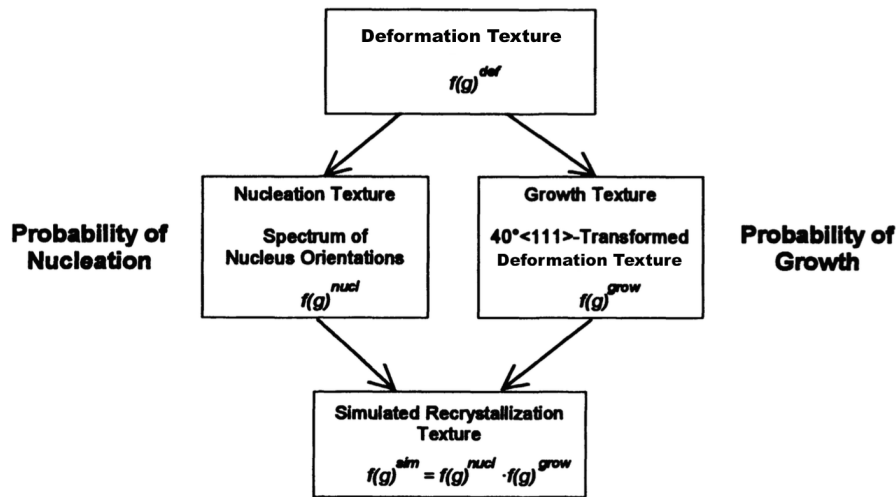
Figure 2.16: Schematic of the model. Figure adapted from Engler (1999) [42].

At first the model needs a data set containing data of the deformation texture, denoted $f(g)^{def}$. This data set is used to generate a set of functions which then

are multiplied to get the simulated texture. For rolling it has been shown that the recrystallised grains in aluminium can be related to the rolling texture by a 40°<111> rotation [43, 44]. The reason for this relationship is due to a growth advantage of boundaries of this relationship and gives the growth function $f(g)^{Growth}$. This relationship is found empirically for rolled profiles, the assumption is also used in this model, although it is for extrusion.

The nucleation mechanisms considered in *RDB_texture* are the same as in *ALSOFT*; PSN, grain boundary nucleation and cube nucleation, this is denoted $f(g)^{nucl}$ and described by Equation 2.18. x_{Cube}, x_{GB} and x_{PSN} are the weighting factors for the different nucleation mechanisms, corresponding to the efficiency of each of them ($x_{Cube} + x_{GB} + x_{PSN} = 1$).

$$f(g)^{nucl} = x_{cube} \cdot f(g)^{nucl}_{Cube} + x_{GB} \cdot f(g)^{nucl}_{GB} + x_{PSN} \cdot f(g)^{nucl}_{PSN} \qquad (2.18)$$

The different nucleation functions are created by using the same ideas as in Engler (1997 & 1999) and Vatne et. al (1996) [27, 41, 42]. $f(g)^{nucl}_{PSN}$ was created by doing a 35°<112> rotation of the deformed structure as described in Engler (1996 & 1997) [12, 41]. This gives rise to a relatively weak texture component. When recrystallised grains nucleate at old grain boundaries, the new grains are closely related to the deformation texture [12]. As a result is $f(g)^{nucl}_{GB}$ found by weakening the deformation texture by using Equation 2.19 [42].

$$f(g)^{nucl}_{GB} = \frac{1}{2} \cdot f(g)^{def} + \frac{1}{2} \cdot f(g)^{random} \qquad (2.19)$$

In Equation 2.19 $f(g)^{random}$ is equal to 1 since this is a random ODF. The final nucleation mechanism considered is cube nucleation, in this model it is assumed to be the <100>-fibre, i.e. the ideal orientation for deformed FCC metals [45].

The final simulated texture is found by Equation 2.20. By multiplying the growth function with the nucleation function, the 40°<111> directions will be the preferred growth direction for the nucleated texture.

$$f(g)^{Simulated} = f(g)^{Growth} \cdot f(g)^{Nucleation} \qquad (2.20)$$

The recrystallisation texture simulations in this report have been modelled in Matlab with MTEX added. MTEX is a texture analysis software available as a free Matlab toolbox, which contains functions to load, manipulate and present EBSD data [46, 47]. The deformation texture, from where all the

functions are developed, is typically a file containing experimentally found EBSD data with orientations from a deformed sample or simulated deformation textures. When doing the 40°<111> rotation on the deformation data there are eight different possible growth directions, due to symmetry (it is four different <111> directions and each of them can be rotated 40°or -40°). It has been reported that not all of these directions are probable growth directions, only some of them will grow faster than other directions [48, 49]. If this is not taken into account there might be a randomisation of the growth texture [48].

3   Experimental & Modelling Procedures

3.1   Material

In this project, all the material is from the same alloy, i.e. an aluminium 6463 alloy. This is a non-dispersoid Al-Mg-Si alloy with the chemical composition shown in Table 3.1. In extruded aluminium alloys, dispersoids are usually introduced to prevent recrystallisation and in this project it is desirable to have the recrystallisation to occur spontaneously at the die exit. For the present alloy and applications, on the other hand, a homogeneous recrystallised structure is desired. The present alloy is also low on other alloying elements (in terms of the content of Mg and Si) with a moderate ageing potential. However, as the potential applications of these extruded materials are mainly electronic devices (in the form

Figure 3.1: The extruded sample to the right and prepared sample to the left.

of cover plates and similar), strength is not an important issue. Due to the low content of Mn (or any other dispersoid forming elements) it will not form dispersoids.

Table 3.1: Chemical composition of material

Composition [wt%]					
Si	**Mg**	**Mn**	**Ti**	**Ga**	**Al**
0.4	0.5	0.096	0.01	0.012	Balance

The material was produced by direct chill casting and homogenised according to standard industrial practice before being extruded. SAPA Finspång delivered the sample and they made an extrusion set-up at their facility for trials where the samples are quenched a few seconds ($\sim$1.5s) after they exit the die. From Figure 3.2 a picture of the extrusion equipment and in Figure 3.3 a sketch on how the press works can be seen. In Table 3.2 the extrusion parameters from the different samples considered in this work are listed. The intention of quenching soon after the material exits the die is to possibly preserve the deformed microstructure and make it possible to examine the microstructure of the extruded profile at this state. The fairly low extrusion

temperatures for D04 is chosen to avoid spontaneous recrystallisation and being able to "freeze" the deformation structure of the extruded profiles.

Figure 3.2: The extrusion equipment used to make the samples in this report. Figure courtesy of SAPA Finspång.
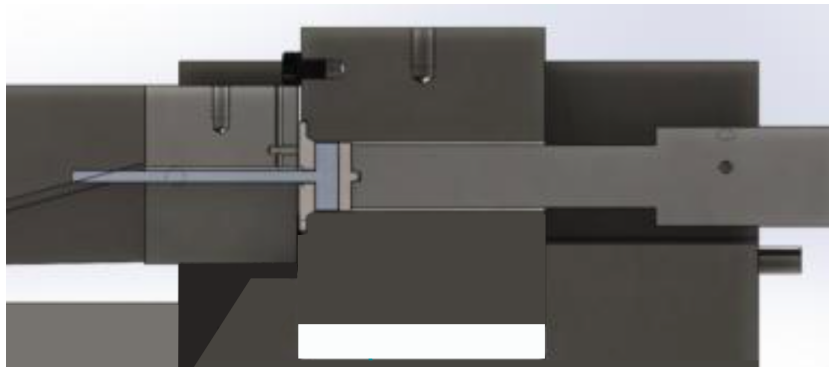
Figure 3.3: A sketch of the extrusion equipment used to make the samples in this report. Figure courtesy of SAPA Finspång.

Table 3.2: Extrusion parameters

Sample name	Ram speed [mm/s]	Initial diameter [mm]	Final diameter [mm]	Strain ϵ	Temp. [°C]
D04	4.5	20	3	3.8	300
E6	4.5	20	3	3.8	400
B2	4.5	20	3	3.8	450
E24	4.5	20	3	3.8	550

3.2   Heat Treatment

The heat treatment was performed by putting the sample in a salt bath, at different temperatures and times, Table 3.3 gives the heat treatment parameters. After being in the salt bath, the samples went into a bucket filled with water at ∼22°C. Cooling time took 1-2 seconds, the sample was taken manually into the water bucket. After heat treatment, the samples were prepared as described in Section 3.3. The column to the right in Table 3.3 indicates from which part across the profile length the different samples were taken out and analysed.

Table 3.3: The different samples analysed and heat treatments performed

Sample	Temperature	Time	Sample position in the profile
B2	-	-	1.5 cm from die and 0.5 cm from tip
E24	-	-	2 mm from the die
E6	-	-	In the middle
D04	-	-	In the middle
D04	450°C	10s	In the middle
D04	450°C	120s	In the middle
D04	450°C	10s + 600s	In the middle
D04	500°C	10s	In the middle

3.3   Sample Preparation

The specimens were cut on a Struers Discotom-2 in lengths of 1.5-2.5 cm and then mounted in a specimen holder with Epofix Cold-Setting Resin, grinding was done with Struers RotoPol-31, as seen in Figure 3.4 and polishing with Struers TegraPol-31. The grinder and polisher are very similar, with both the specimen holder and paper/disc rotating. Struers grinding paper and polishing discs were used, polished until 1 μm. The final step of sample preparations was electropolishing, Struers Lectropol-5 where the settings shown in Table 3.4 were used. The electropolishing was done by holding the specimen with a clip as shown in Figure 3.5. In Figure 3.6 a close up of a polished sample can be seen, the white part on the sample end is where the clip is held and thus preventing this area from being electropolished. When electropolishing the final deformation layer, introduced by grinding and polishing, is being removed from the surface and the "true" microstructure is revealed.

Table 3.4: Electropolishing settings

Setting	Electropolishing
Voltage	20 V
Area	0.5 cm^2
Time	15s
Solution	A2 [50]
Solution temperature	-30°C
Flow rate	2
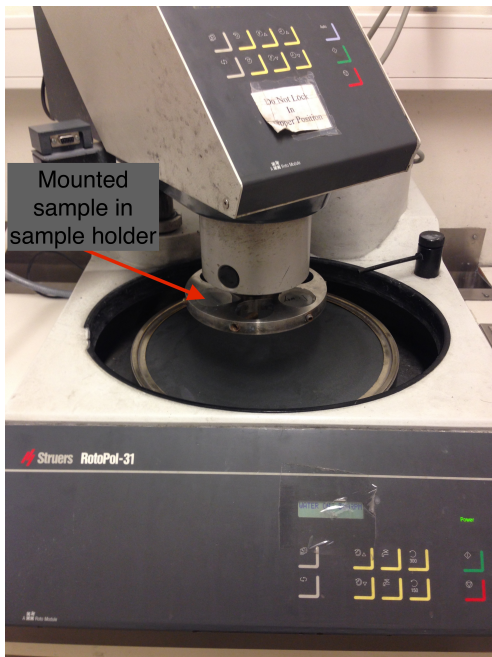
Figure 3.4: Setup for grinding and polishing
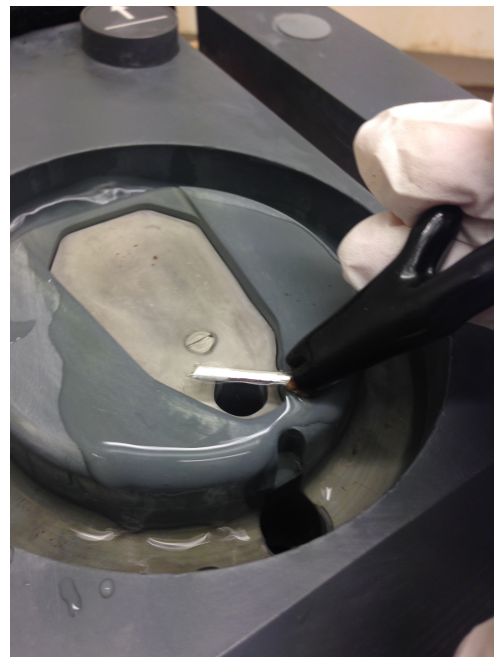
Figure 3.5: Setup for electropolishing

3.4 Electron Backscattering Diffraction

A Zeiss Supra 55VP SEM with an EBSD detector was used to obtain diffraction patterns from the sample surface. The SEM settings can be seen in Table 3.5. All the samples were analysed across the transverse area, from centre-to-surface. Figure 3.6 illustrates where on the sample surface the EBSD scans were performed. The centre-to-surface scans were performed twice and merged together. For all the samples, except for B2 (die), this resulted in a surface-to-surface scanned area. For B2 (die) this resulted in a larger surface-to-centre scanned area.

Table 3.5: Settings on SEM during EBSD analysis

Setting	EBSD
Accelerating Voltage	20 kV
Current Mode	High current
Working Distance	25 mm
Aperture Diameter	300 μm
Tilt Angle	70°
Step Size	3 mm
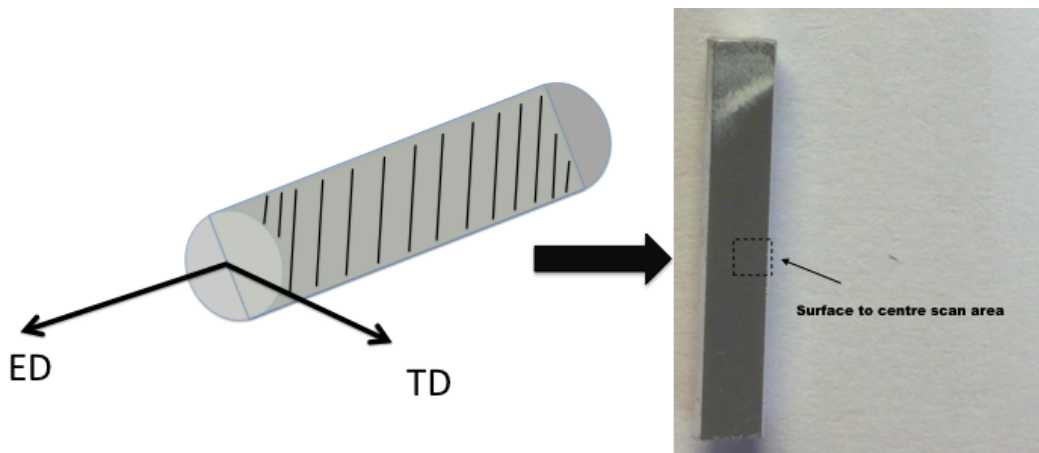
Figure 3.6: The shaded area in the illustration to the left indicates which area analysed. Electropolished sample with the scanned area marked to the right.

The NORDIFF software was used to obtain diffraction pattern from the SEM and the pattern was indexed by the EDAX OIM software. TSL OIM software was used to create grain maps, finding grain sizes, fraction recrystallised and exporting the scanned data for texture analyses in Matlab. The Matlab implementation of *RDB_texture* was used for plotting pole figures and ODF's from the experimental data. A filter was applied to take away possible erroneous indexed points from the EBSD scan for all analyses. All scanned points with a confidence index lower than 5% were removed. When calculating the grain size a built-in function in TSL OIM was used to calculate the diameter. To be defined as a grain in this calculation, a grain needed to contain at least 5 scanned points. When finding area fraction recrystallised grains, a recrystallised grain was defined as a grain with a spread in orientation within the grain lower than 2°. In TSL OIM, there is a built-in function performing this calculation.

3.5 Input Values & Settings for Simulations

3.5.1 *ALSOFT*

A Matlab implementation of the softening model *ALSOFT* was used to illustrate how fraction recrystallised and recrystallised grain size evolve as a function of time depending for different initial deformation conditions and annealing temperature. The calculations are based on a set of model parameters previously used to calculate the post-extrusion annealing behaviour of an AA6060 alloy (similar to the present alloy), experimentally found data for the present alloy and simulated data from the extrusion process for samples considered in this project. The calculations are intended to briefly show how different deformation conditions and annealing temperatures (chosen according to the actual experimental conditions used in this work) affect the recrystallisation kinetics and the recrystallised grain size and for some rough semi-quantitative comparisons with the actual experimental results. Except for the values in Table 3.6 and 3.7 and annealing temperatures, the different input model parameters for the AA6060 alloy are given in Table 1 in Appendix A [51]. The chemical composition of this 6060 alloy are given in Table 3.8, and as seen it is very similar to the composition of the alloy studied in this work (i.e. AA6463, cf. Table 3.1 and 3.8).

Table 3.6: Simulation parameters for *ALSOFT* as obtained from *ALFLOW* and FEM analysis, courtesy of Kai Zhang [52].

	Int. disl. density [m^2]	Int. sub-grain size	Temp. at int. def.	Strain rate at int. def.	True strain after int. def.
D04 - 300	5.22E+13	1.14 μm	373°C	104 s^{-1}	3.94
D04 - 1200	5.67E+13	1.05 μm	374°C	203 s^{-1}	5.02
D04 - 1350	6.15E+13	0.93 μm	374°C	388 s^{-1}	6.24
B2 - 300	2.61E+13	2.91 μm	496°C	102 s^{-1}	3.97
B2 - 1200	3.01E+13	2.51 μm	496°C	198 s^{-1}	5.23
B2 - 1350	3.24E+13	2.33 μm	496°C	375 s^{-1}	6.18

Table 3.7: Experimentally found values for input into *ALSOFT*, courtesy of Kai Zhang [52].

Parameters	Experimentally found values
Volume fraction particles	0.004
Mean particle size [μm]	1.4
Initial (as-cast) grain size [μm]	9

Table 3.8: Alloy composition used as input data in *ALSOFT*

Element	AA6060 [wt%]
Si	0.43
Fe	0.20
Mg	0.48
Mn	0.02
Al	Balance

The simulation parameters considered in the calculations (Table 3.6 and 3.7) have been obtained from the COSMETEX research group ([52]). These are based on FEM calculations by the FEM code HyperExtrude and subsequently use of the work hardening model *ALFLOW* [35–37, 53] and for comparison with the latter, the empirical relationship in Equation 3.1. The latter relationship was developed by Nes (1995) [54]. Here A and B are alloy-dependent constants, and Z is the Zener-Hollomon parameter, described in Equation 2.1. The range of parameters in Table 3.6 are values depending on the deformation temperature and through-thickness variations in the extruded profiles, where the surface regions experience a stronger deformation than the mid-section, and thus a higher driving force for recrystallisation. These parameters have been obtained by HyperExtrude and FEM simulations and subsequent use of the *ALFLOW* model for the extrusion process in D04 and B2. For the initial deformation temperature, strain rate and strain, the maximum value during the simulated extrusion process was chosen. The simulations were performed for different sections through the thickness of the profile. This is indicated in the first column in Table 3.6, where the number behind the simulated sample name is the distance (in μm) from the profile centre where the simulations were performed. This means that D04 - 300 would be representative for the centre region of the profile and D04 1350 for the sub-surface region.

$$\frac{1}{\delta} = \frac{RT}{A} \ln\left(\frac{Z\delta^2}{B}\right) \tag{3.1}$$

The *ALSOFT* simulations were performed with the same annealing temperatures as in the experiments and the annealing in *ALSOFT* is displayed in Table 3.9.

Table 3.9: Simulated annealing temperatures with *ALSOFT*

Simulated sample	Annealing temperature
D04 - 300	
D04 - 1200	T = 450°C
D04 - 1350	
D04 - 300	
D04 - 1200	T = 500°C
D04 - 1350	

When calculating the stored energy the contribution from cell-interior dislocation density can be ignored as it represents only a minor fraction of the total stored energy, thus mainly given by the sub-grain size.

The temperature dependence of these parameters can be displayed by a simple numerical example. In the paragraph below this has been done. These calculations have been performed using *ALSOFT* with the AA6060 input file loaded. Here T_{def}, $\dot{\varepsilon}$ and ε is respectively the temperature, strain rate and strain during deformation and these values are chosen from Table 3.6. From this, it is possible to calculate the Zener-Holloman parameter, Z, and sub-grain size, δ, by using respectively Equation 2.1 and Equation 3.1. The dislocation density is related to the sub-grain size by the relationship $\rho_i = \left(\frac{C_1}{\delta}\right)^2$, where C_1 is a constant. When loading the AA6060 input file into *ALSOFT*, C_1 = 2. In *ALSOFT*, Equation 3.1 is solved by iterating using Newtons method. When these variables are known it is possible to calculate the driving force for recrystallisation with Equation 2.4.

$T_{def} = 373°C$ 　　　　　　$T_{def} = 496°C$
$\dot{\varepsilon} = 104 s^{-1}$ 　　　　　　$\dot{\varepsilon} = 102 s^{-1}$
$\varepsilon = 3.94$ 　　　　　　$\varepsilon = 3.97$

$Z = 8.53 \cdot 10^{14} s^{-1}$ 　　　　$Z = 7.49 \cdot 10^{12} s^{-1}$
$\rho_i = 6.87 \cdot 10^{12} m^{-2}$ 　　$\rho_i = 3.33 \cdot 10^{12} m^{-2}$
$\delta = 0.8 \mu m$ 　　　　　　$\delta = 1.1 \mu m$

$P_D = 4.11 \cdot 10^5 Pa$ 　　　　$P_D = 2.84 \cdot 10^5 Pa$

From the calculations above the driving force for recrystallisation in the centre of D04 and B2 have been compared. From these calculations it is possible to see that this goes down more than 30% when extruding at higher temperatures. The dislocation density and initial sub-grain size when using Equation 3.1 are lower than the predictions with *ALFLOW*.

3.5.2   Recrystallisation Texture Model

The recrystallisation model was created by using Matlab with the addition of the free and open sourced MTEX toolbox added [46]. MTEX has a lot of built-in functions which was used to create a Matlab programme to predict the recrystallised texture from a deformed structure. The deformation structure was obtained by EBSD analysis of the deformed D04 and exported to a text file, which in turn can be loaded into the Matlab programme. This programme was used to plot the texture and run simulations. The texture calculations in MTEX used harmonic series expansion with $l_{max} = 22$, $\psi_0 = 5°$ and triclinic sample symmetry. When calculating ODF's using MTEX the user has to define the symmetry of the loaded data. When comparing with *RDB_texture* which was created for rolling, orthorhombic specimen symmetry was chosen and when looking at the extruded D04 sample, triclinic was chosen. With orthorhombic sample symmetry, the φ_1-range in the ODF plot is 0-90° and for triclinic it is 0-360°. The cube nucleation in the software comes from an external file loaded into the software. This could be the cube nucleation file used in *RDB_texture* for rolled components or an ODF containing the <100>-fibres from the deformation structure. These fibres can be extracted from EBSD-data by using MTEX or TSL OIM.

In the software the different weighting components in the nucleation function $f(g)^{nucl}$, Equation 2.18, has to be selected by the user. These were empirically found by looking at the difference between the experimentally found recrystallised ODF and simulated ODF, by using Equation 2.2 (GOF). A Matlab code was created to run through a number of different combinations of weighting factors and then comparing the simulated ODF with an experimentally recrystallised ODF. As the recrystallised reference, spontaneously recrystallised B2 and statically recrystallised D04 were used. The equations used in *AL-SOFT* was also used to find these weighting factors, Equation 2.6, 2.7 and 2.8. These weighting factors were found running *ALSOFT* simulations with the data from alloy AA6060, as described in Section 3.5.1.

To validate the Matlab implementation of *RDB_texture*, a data set provided by Kai Zhang of a rolled sample was used to compare the two models. A description of this data set can be found in Zhang et al. (2014) [55]. The alloy used was AA3103 sheets in cold rolled condition, then used *RDB_texture* and the Matlab implementation to generate a recrystallised texture. Harmonic series expansion with $l_{max} = 22$, $\psi_0 = 5°$ and orthorhombic sample symmetry was used when calculating the ODF's. There was no normalisation performed and the randomisation of the grain boundary nucleation was set to be 50%. The weighting factors used was the same as found to be the best fit in Engler (1997); $x_{Cube} = 0.3$, $x_{GB} = 0.5$ and $x_{PSN} = 0.2$. The ODF's of the different

nucleation mechanisms from both software will also be presented to be able to indicate from where differences may arise.

In Appendix C, the Matlab functions used to generate $f(g)_{GB}^{nucl}$, $f(g)_{PSN}^{nucl}$, $f(g)_{Cube}^{nucl}$, $f(g)^{Nucleation}$, $f(g)^{Growth}$ and $f(g)^{Simulated}$ have been attached.

4 Experimental Results

In the follow section will results from EBSD analysis of the different samples be presented. For all samples a grain map, pole figures, recrystallised area fraction and average grain diameter will be given. At the end of this section, all of the results will be summarised and compared. The samples analysed and being presented are listed in Table 4.1.

Table 4.1: The different samples analysed

Sample	Extrusion temperature	Ram speed [mm/s]	Comments
D04	300°C	4.5	As deformed
D04	300°C	4.5	Heat treated for 10s at 450°C
D04	300°C	4.5	Heat treated for 120s at 450°C
D04	300°C	4.5	Heat treated for 610s at 450°C
D04	300°C	4.5	Heat treated for 10s at 500°C
E6	400°C	4.5	Spontaneously recrystallised
B2	450°C	4.5	Spontaneously recrystallised
E24	550°C	4.5	Spontaneously recrystallised

4.1 Deformed D04 - Extruded at 300°C
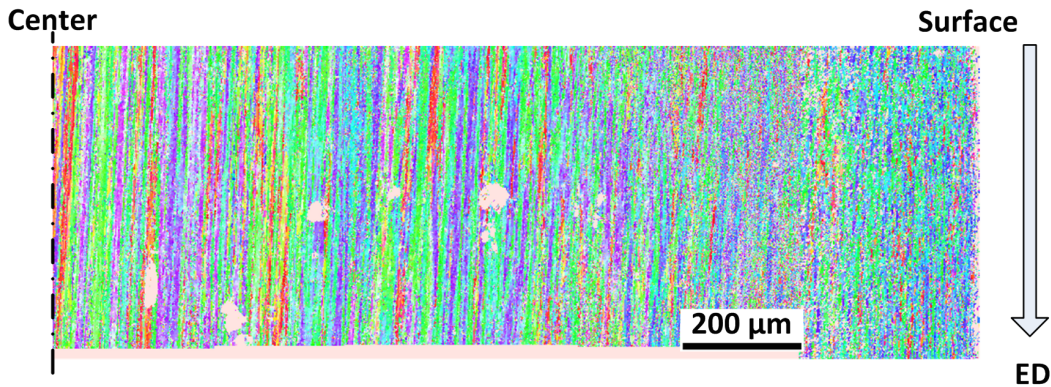
Figure 4.1: D04 deformed grain map, specimen surface to the right and centre to the left, 500 μm x 3 mm. Figure courtesy of Kai Zhang.

When the D04 was extruded at 300°C the sample did not recrystallise after extrusion and ended up with a fibrous microstructure as seen in Figure 4.1. From Figure 4.2 it is shown that the sample has a very strong <111> texture with some <100> texture present. The intensities are respectively 15.2 and

4.7. EBSD results of this deformed D04 sample were loaded into the recrystallisation software. From this data set, the growth and nucleation function in Equation 2.20, were created. The ODF of D04 can be seen in Figure 4.3, here it can be seen that the <100> cube fibre is present. There are also some strong fibres present and they have the strongest intensity.
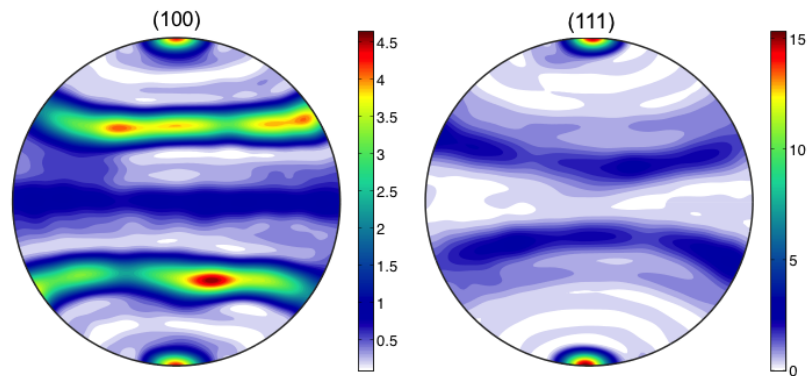
Figure 4.2: (100) and (111) pole figures of sample D04, deformed after extrusion.
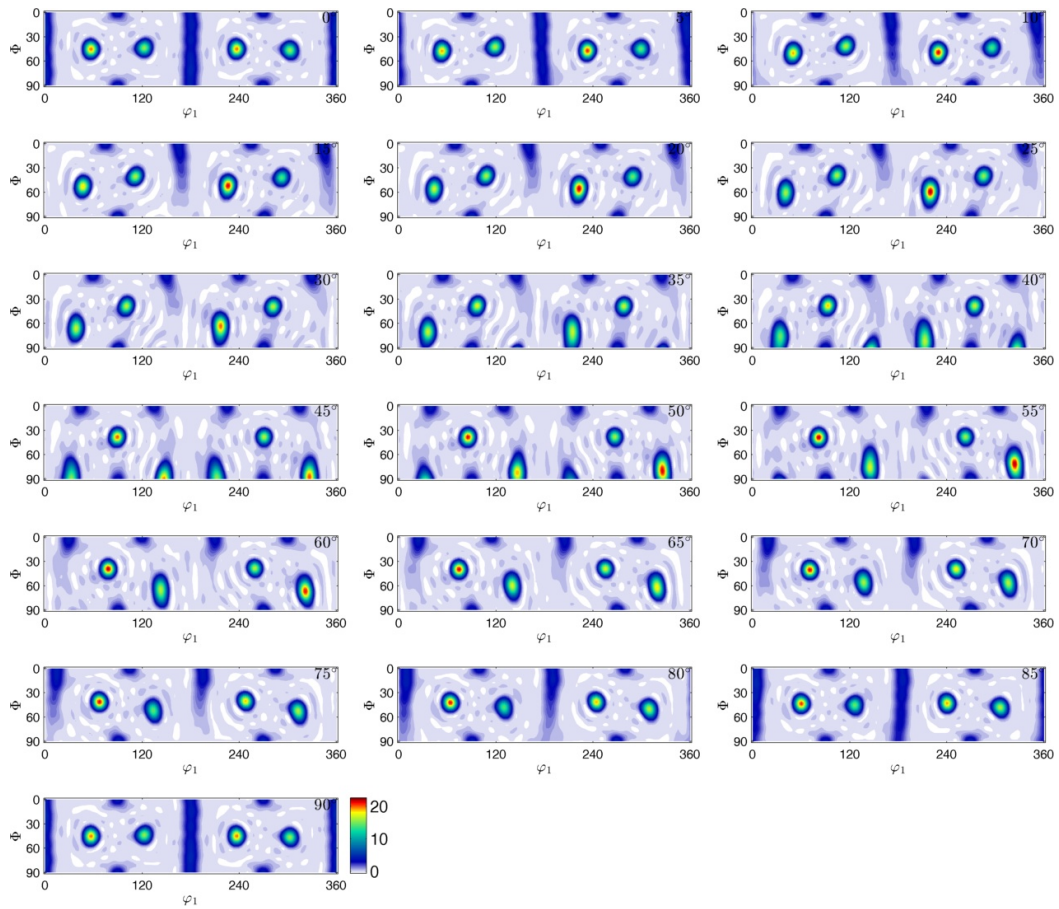
Figure 4.3: ODF of sample D04, deformed after extrusion.

4.2   Heat Treated D04

4.2.1   Heat Treated D04 - 10s at 450°C
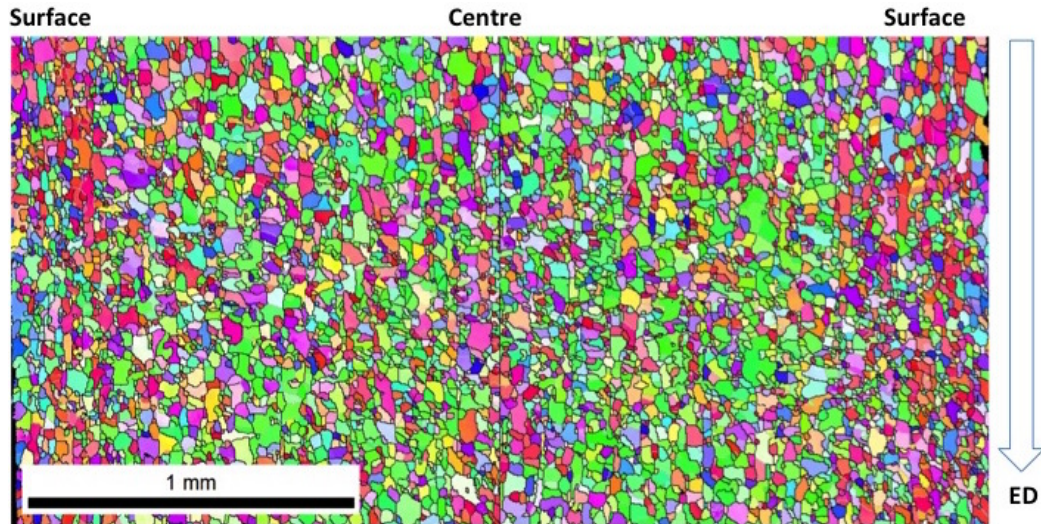
Figure 4.4: D04 10s at 450°C grain map. 1.5 mm x 3 mm, the surface is the left and right boundary in the grain map.

In figure 4.4 the microstructure of the sample after being heat treated for 10s at 450°C can be seen. The sample did not fully recrystallised, having a recrystallised area fraction of 86.9% and average grain diameter of 25.3 μm. There are smaller grains close to the surface and larger ones in the centre. The (100) and (111) pole figures of this sample is shown in Figure 4.5, from this the texture intensities can be seen. The <111> texture has a maximum intensity of 6 and the <100> texture has a maximum of 3.9.
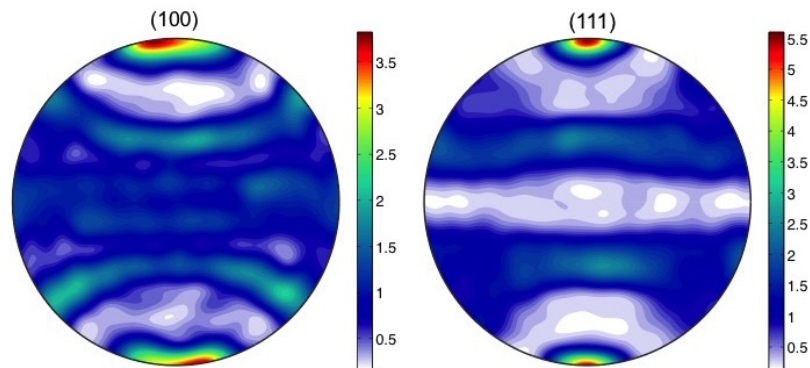
Figure 4.5: (100) and (111) pole figures of heat treated D04, 10s at 450°C.

4.2.2 Heat Treated D04 - 120s at 450°C

After being heat treated for 120s at 450°C the sample is very similar to the sample heat treated at 10s at 450°. The average grain diameter is 25.4 μm and the recrystallised area fraction is 87.8%. In Figure 4.7 the (100) and (111) pole figures can be seen, the maximum intensity of <111> texture is 6.7 and for <100> texture it is 3.9.
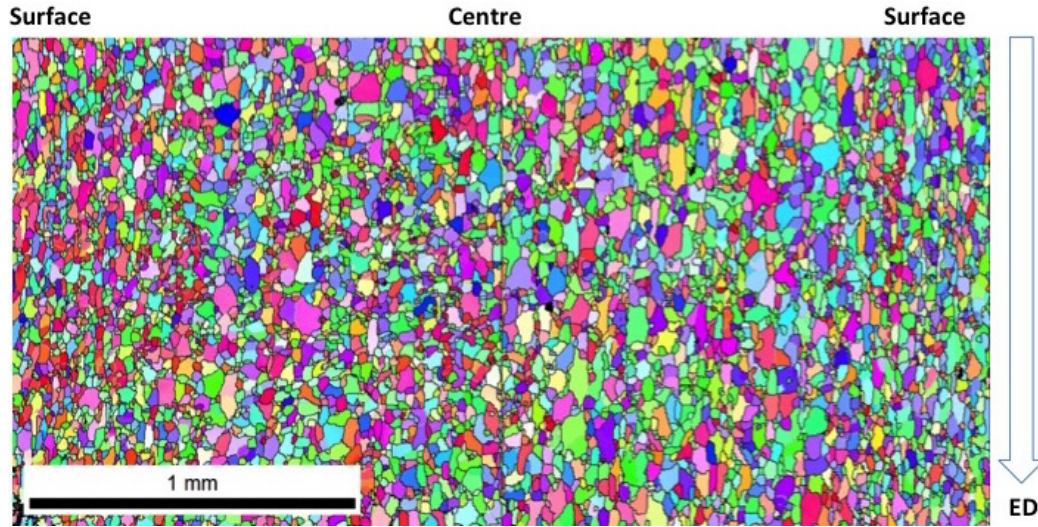
Figure 4.6: D04 120s at 450°C grain map. 1.5 mm x 3 mm, the surface is the left and right boundary in the grain map.
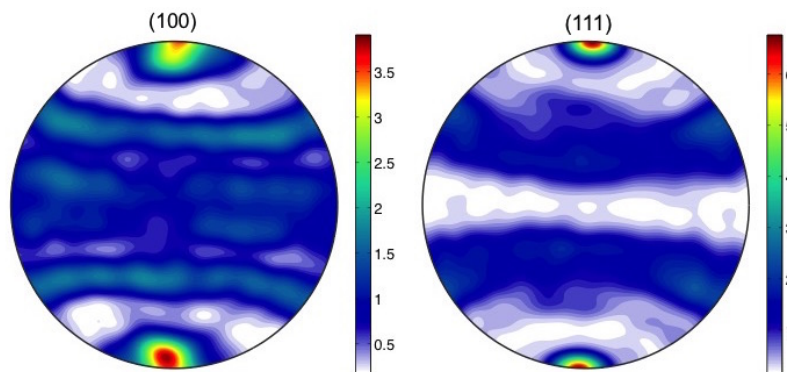
Figure 4.7: (100) and (111) pole figures of heat treated D04, 120s at 450°C.

4.2.3 Heat Treated D04 - 610s at 450°C

The sample held at 450°C for 610s more or less fully recrystallised, with a recrystallised area fraction of 89.5%. The sample has an average grain diameter of 29.3 μm. Looking at the grain map in Figure 4.8 some small grains close to the surface can be seen. Other than these the grain structure consists more or less of equiaxed grains. This heat treated recrystallised sample has a weak <100> texture with an intensity of 3.5 and a stronger <111> texture with an intensity of 7.2. The (100) and (111) pole figures can be seen in Figure 4.9.
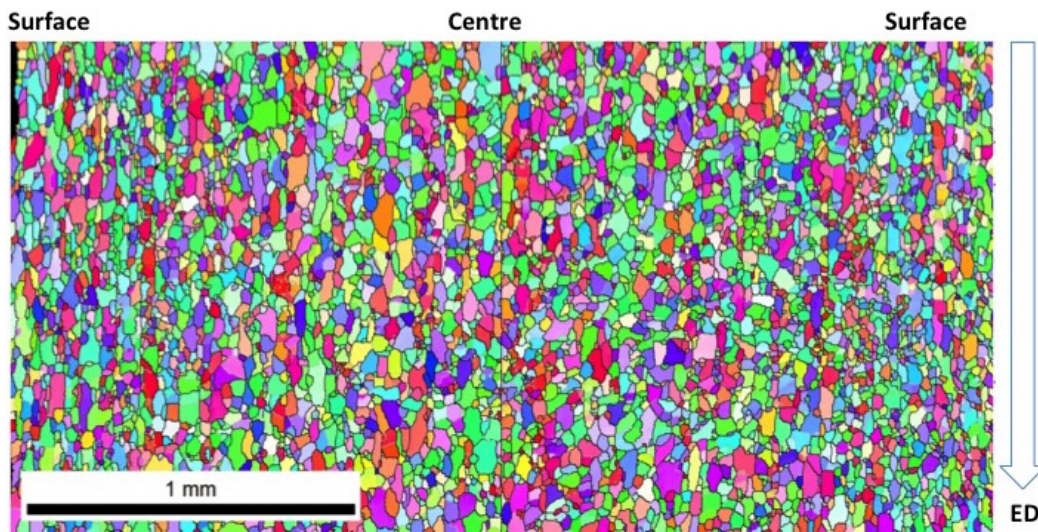
Figure 4.8: D04 610s at 450°C grain map. 1.5 mm x 3 mm, the surface is the left and right boundary in the grain map.
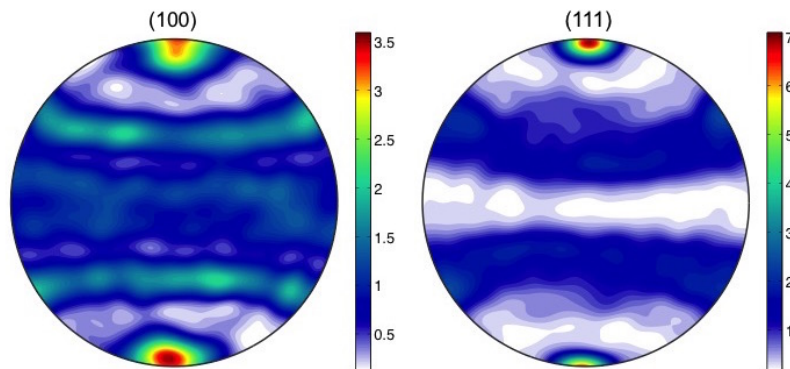
Figure 4.9: (100) and (111) pole figures of heat treated D04, 610s at 450°C.

4.2.4 Heat Treated D04 - 10s at 500°C

In Figure 4.10 the grain map for the sample heat treated at 500°C for 10s can be seen, from this map it is possible to see that the sample fully recrystallised. The sample has an average grain diameter of 29.3 μm with a recrystallised area fraction of 91.5%. This heat treated statically recrystallised sample has a weak <100> texture, with an intensity of 3.6 and a stronger <111> texture with an intensity of 7.2. This is shown in the (100) and (111) pole figures in Figure 4.11.
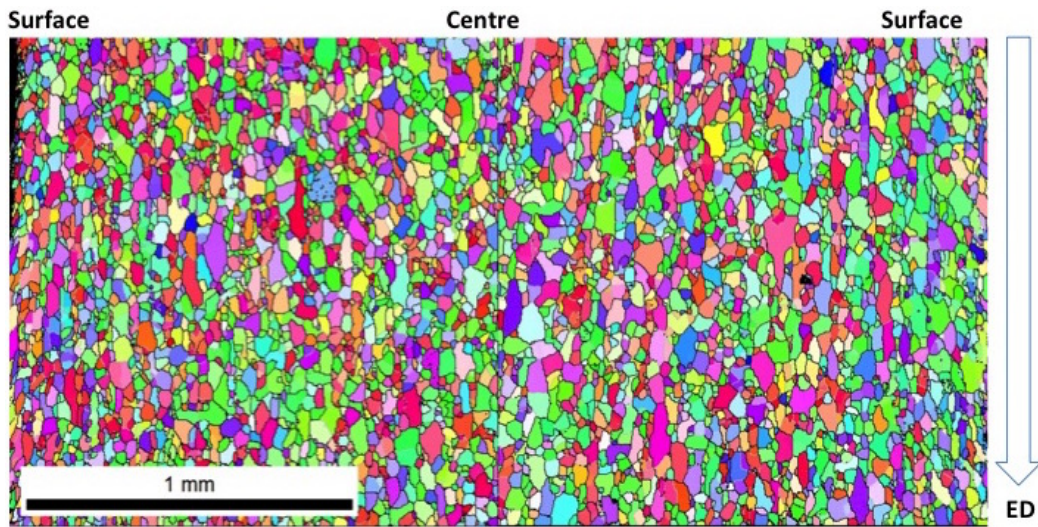
Figure 4.10: D04 10s 500°C grain map. 1.5 mm x 3 mm, the surface is the left and right boundary in the grain map.
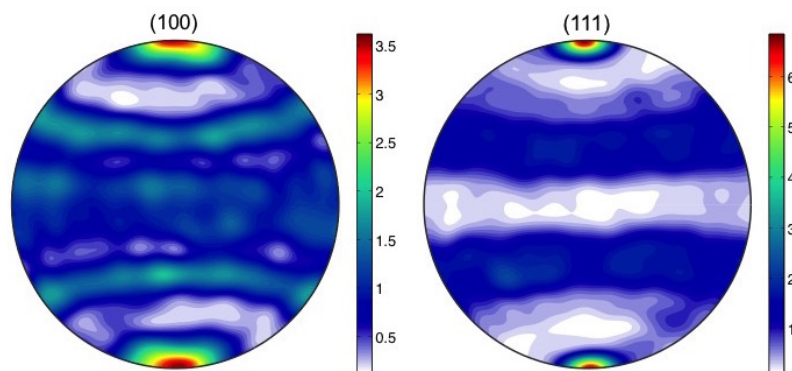
Figure 4.11: (100) and (111) pole figures of heat treated D04, 10s 500°C.

4.3 Spontaneously Recrystallised Extruded Samples

4.3.1 E6 - 400°C
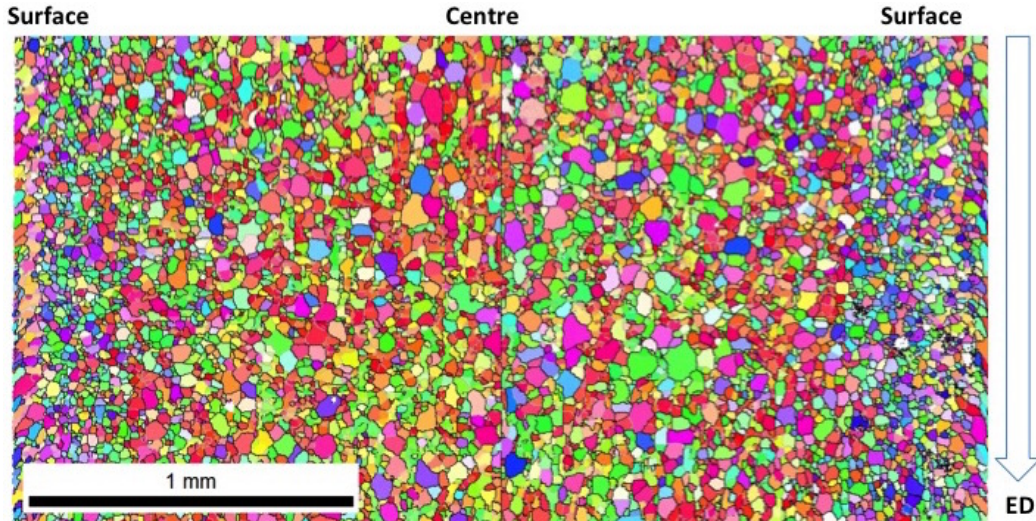
Figure 4.12: Grain map of sample E6, recrystallised after extrusion. 1.5 mm x 3 mm, the surface is the left and right boundary in the grain map.

E6 was extruded at 400°C and from Figure 4.12 it can be seen that the sample spontaneously recrystallised. The recrystallised area fraction is 90.4% and the sample have an average grain diameter of 24.1 μm. There are smaller grains at the surface, and larger ones in the centre. The texture can be seen in Figure 4.13, it has a maximum <100> intensity of 11.1 and <111> intensity of 3.5.
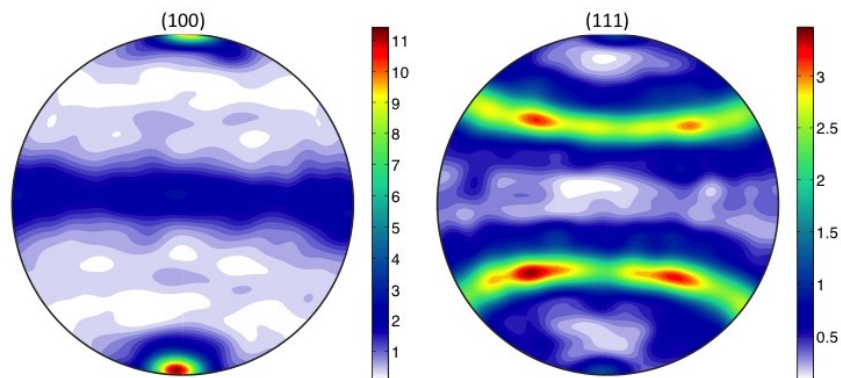
Figure 4.13: (100) and (111) pole figures of sample E6, recrystallised after extrusion.

4.3.2   B2 Tip - 450°C
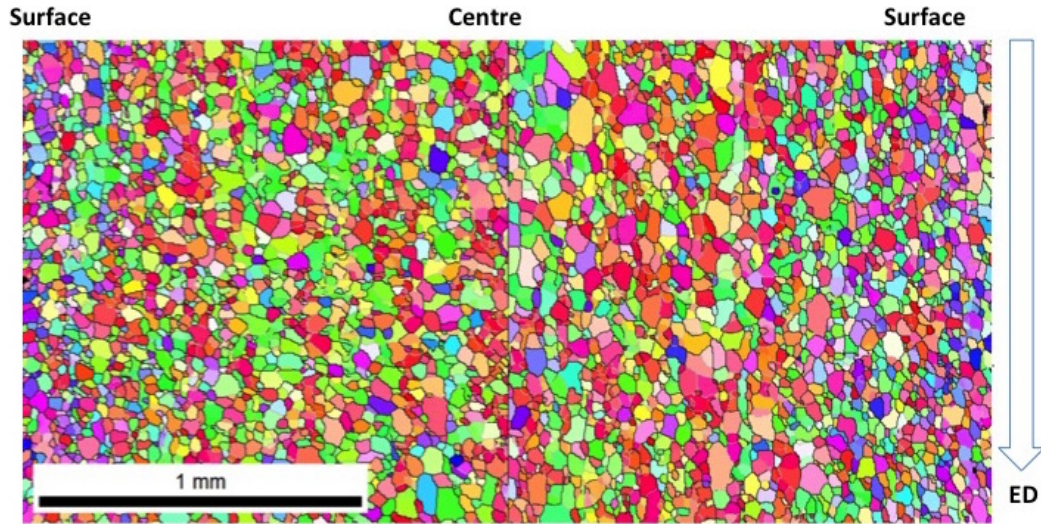
Figure 4.14: Grain map of sample B2 at the extrusion tip, recrystallised after extrusion. 1.5 mm x 3 mm, the surface is the left and right boundary in the grain map.

B2 was extruded at 450°C and spontaneously recrystallised during the process. The equiaxed recrystallised grain structure can be seen in Figure 4.14. B2 is the most recrystallised sample, 92% recrystallised area fraction, with the average grain diameter 29.9 μm. The texture of B2 is relatively weak, but the has some <100> texture as seen in Figure 4.15. Maximum intensity of <100> texture is 7.7.
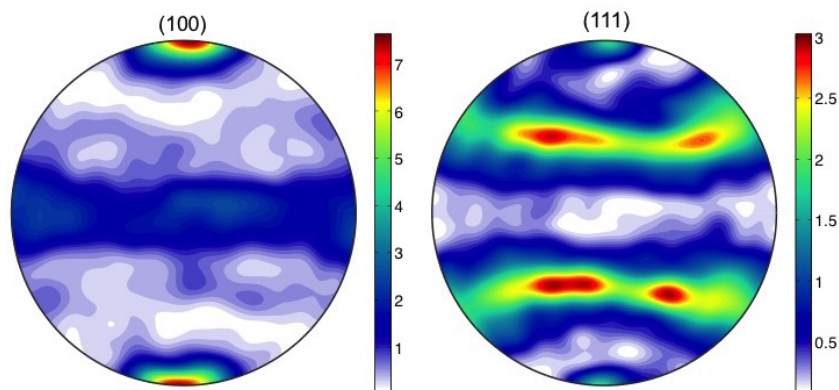
Figure 4.15: (100) and (111) pole figures of sample B2 (tip), recrystallised after extrusion.

4.3.3   B2 Die - 450°C
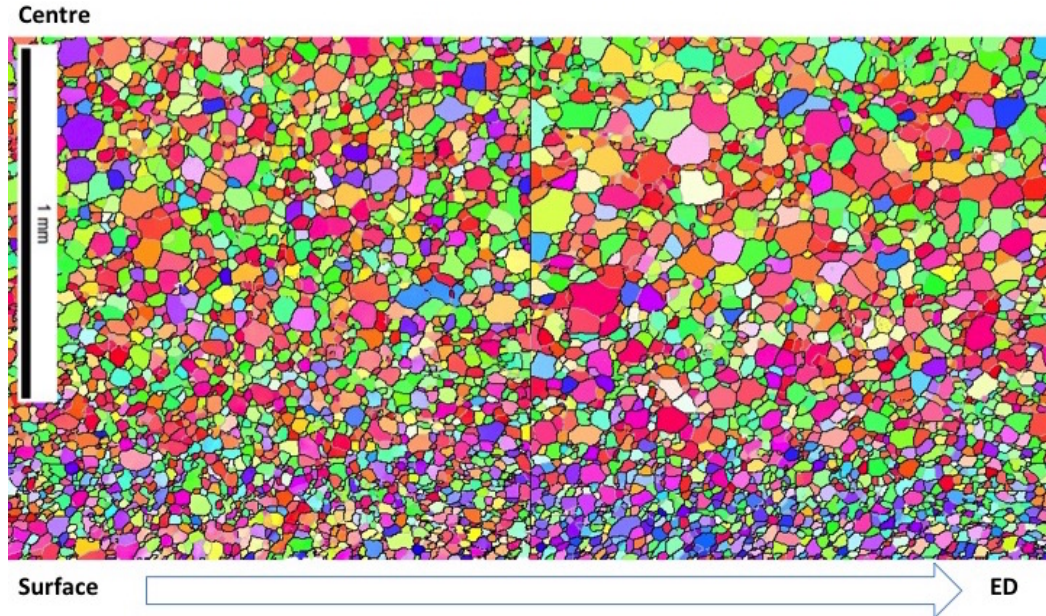
Figure 4.16: Grain map of sample B2 at the extrusion die, recrystallised after extrusion, 1.5 mm x 3 mm, sample centre at the top and sample surface at the bottom.

A section of B2 was analysed both close to the die and close to the tip of the extruded string. This to see if there were any difference in grain structure along the length of the extruded profile. The grain map of the B2 sample taken close to the die can be seen in Figure 4.16. When comparing Figure 4.16 and 4.14 it does not look like there is any difference between the two grain structures. B2 (die) has an average grain diameter of 29.2 μm and recrystallised area fraction of 91.5% whilst for B2 (tip) it is respectively 29.9 μm and 92%. The texture intensities are also similar. As for B2 (tip), B2 (die) has a stronger <100> texture and a weak <111> texture. This can be seen in Figure 4.17. For B2 (tip) the maximum intensity of <100> is 7.7, whilst for B2 (die) it is 8.7.
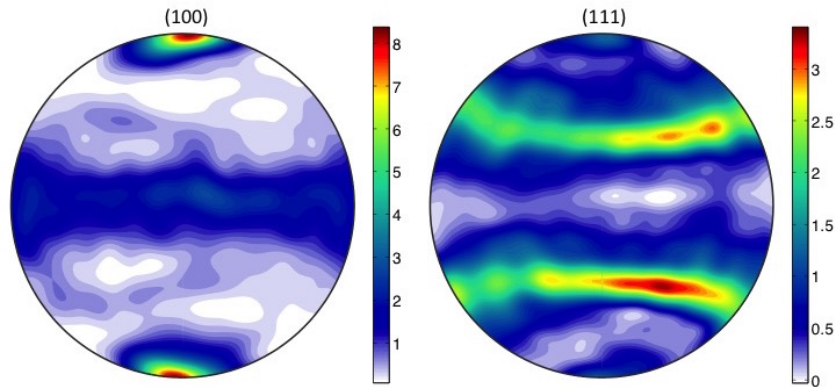
Figure 4.17: (100) and (111) pole figures of sample B2 (die), recrystallised after extrusion.

4.3.4 E24 - 550°C
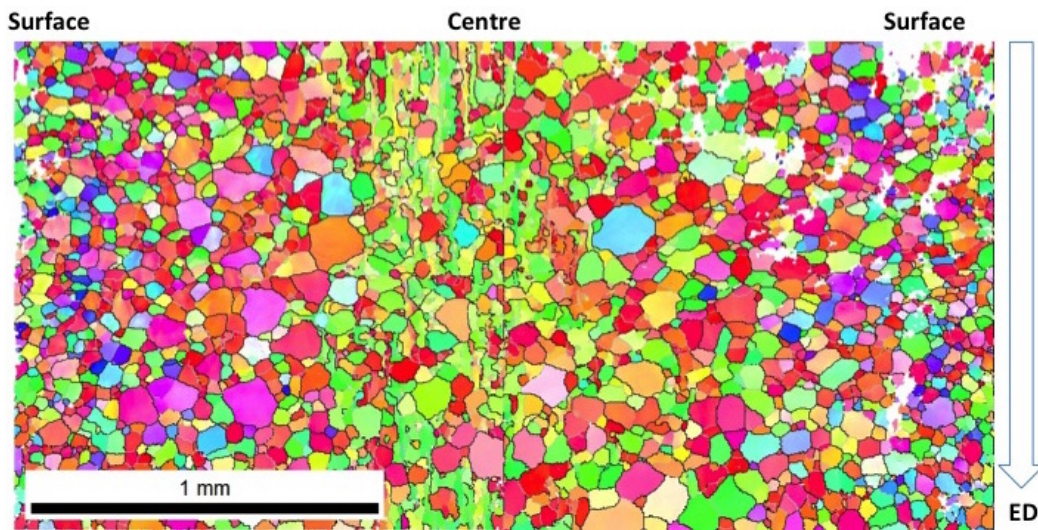
Figure 4.18: Grain map of sample E24, recrystallised after extrusion. 1.5 mm x 3 mm, the surface is the left and right boundary in the grain map.

This sample was extruded at 550°C and have a large average grain diameter of 34.9 μm. The texture is shown in Figure 4.19 and consists of a strong <100> cube texture, with the maximum intensity of 17.2. <111> texture is less present, with the maximum intensity of 4.2. In the centre of Figure 4.18, there is a region where the grain structure does not consist of equiaxed grains. The total recrystallised area in this sample is 76.9%, the lowest value of all samples, in spite of being the sample extruded at the highest temperature.

This is probably due to the fact that this sample is taken ∼2 mm from the die and, therefore, did not recrystallise as fast as the area closer to the surface.
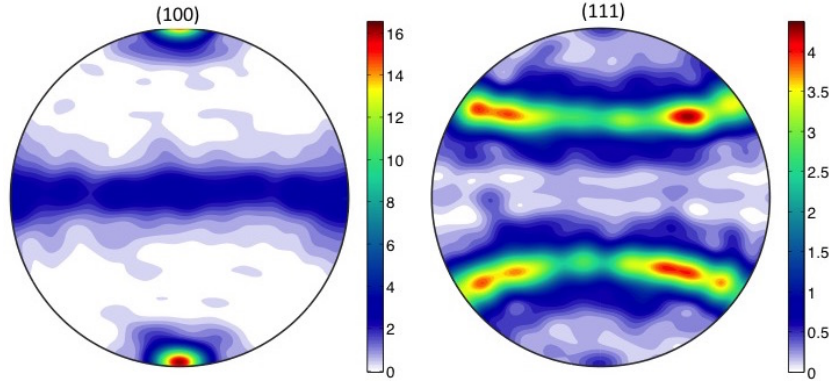
Figure 4.19: (100) and (111) pole figures of sample E24, recrystallised after extrusion.

4.4 Summary of Experimental Results

In Table 4.2, 4.3 and Figure 4.20 and 4.21 the experimental results have been summarised. The texture intensity values are based on pole figures and ODF's attached in Appendix D.

Table 4.2: Summary of experimental results

Sample	Max <100> intensity	Max <111> intensity	Max ODF intensity	Recrystallised Area Fraction	Average Grain Diameter μm
E6	11.1	3.5	12.6	90.4%	24.1
B2 - tip	7.7	3	9.6	92%	29.9
B2 - die	8.7	3.4	10.3	91.5%	29.2
E24	16.5	4.2	20.4	76.9%	34.9
Deformed D04	4.7	15.2	24.7	-	-
Heat treated D04 10s 450°C	3.9	6	8.8	86.9%	25.3
Heat treated D04 120s 450°C	3.9	6.7	8	87.8%	25.4
Heat treated D04 610s 450°C	3.5	7.2	9.4	89.5%	27.5
Heat treated D04 10s 500°C	3.6	7.2	7.1	91.5%	29.3

The experimentally found textures have also been compared by using Goodness of Fit (Equation 2.2) to compare the ODF's. In Table 4.3 the returned values are listed. A lower GOF value indicates a similar texture. The spontaneously recrystallised samples have the lowest values when being compared

to each other. The agreement between two statically recrystallised samples is also quite good, but not as good as between two spontaneously recrystallised samples. When comparing a statically and spontaneously recrystallised sample the agreement is still not too bad and a similar texture is indicated.

Table 4.3: ODF comparison between experimentally found textures

ODF's compared	GOF value
D04 heat treated for 610s at 450°C vs B2	0.7
D04 heat treated for 10s at 500°C vs B2	0.6
D04 heat treated for 610s at 450°C vs D04 heat treated for 10s at 500°C	0.4
E24 vs B2	0.3
E6 vs D04 heat treated for 10s at 500°C	0.6
E6 vs B2	0.2
E6 vs E24	0.3

In Figure 4.20 and 4.21 the texture intensities of respectively the spontaneously and statically recrystallised samples. From this, it is possible to see that the spontaneously recrystallised samples, in general, have a stronger <100> texture and weaker <111> texture. For statically recrystallised samples, it is the opposite. When looking at the bars it can be seen that the ratio between the strongest and weakest texture is larger for spontaneously recrystallised samples.
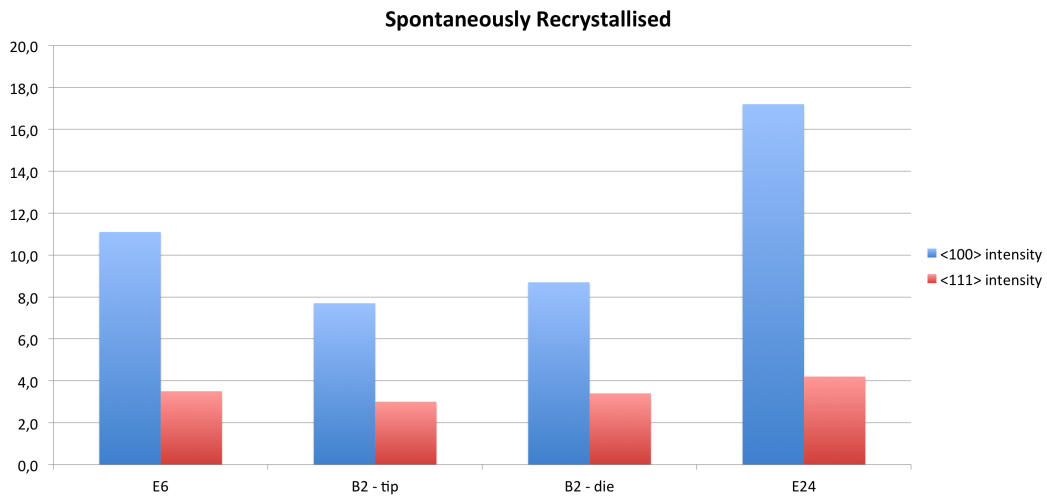
Figure 4.20: Texture summary of spontaneously recrystallised samples.
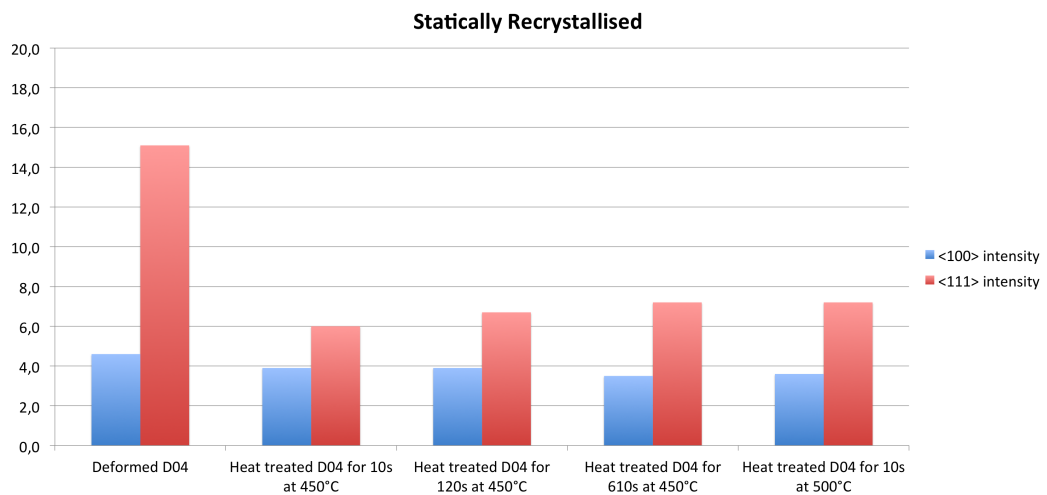
Figure 4.21: Texture summary of heat treated samples.

5   Modelling Results

The simulated recrystallisation textures and grain structure will be presented in this section. Simulations have been performed with the Matlab implementation of *RDB_texture*. Firstly this implementation will be compared with *RDB_texture* in an effort to validate the software developed in Matlab. Then some simulations have been performed with different input values into the model and compared the simulated texture with experimentally found textures. Simulated textures with different weighting factors (i.e. the relative contribution of different nucleation mechanism) as input, were compared with experimentally found recrystallisation texture. A set of weighting factors giving the best fit with experimental data will be presented. The grain structure simulations have been performed with *ALSOFT*. Here graphs on how recrystallised fraction and grain size evolves with time for different heat treatment temperatures and initial sub-grain sizes (i.e. stored energy) have been generated.

5.1   Validation of Matlab Implemented Texture Recrystallisation Model

The recrystallisation model for modelling recrystallisation textures is a Matlab implementation of *RDB_texture* described in Engler (1997 & 1999) [41, 42]. In Figure 5.1 the overall concepts in the model are presented. A set of functions is generated from a loaded deformation texture (in terms of a set of Euler angles). The orientation spectrum of cube nucleation is loaded as an external file.

In the following section, a comparison between the models will be presented to look at the differences and similarities between the final recrystallised texture in the two softwares. The data set used to compare these was provided by Kai Zhang and a description of it can be found in Zhang et al. (2014) [55]. It contains texture data from an AA3103 sheet in cold rolled condition (AA3103H18). This data set is only used for comparing *RDB_texture* and the Matlab implementation. To compare the two models, the ODF of each step in both are printed out. From this, it is possible to see from where any possible differences in the final recrystallised texture may arise.
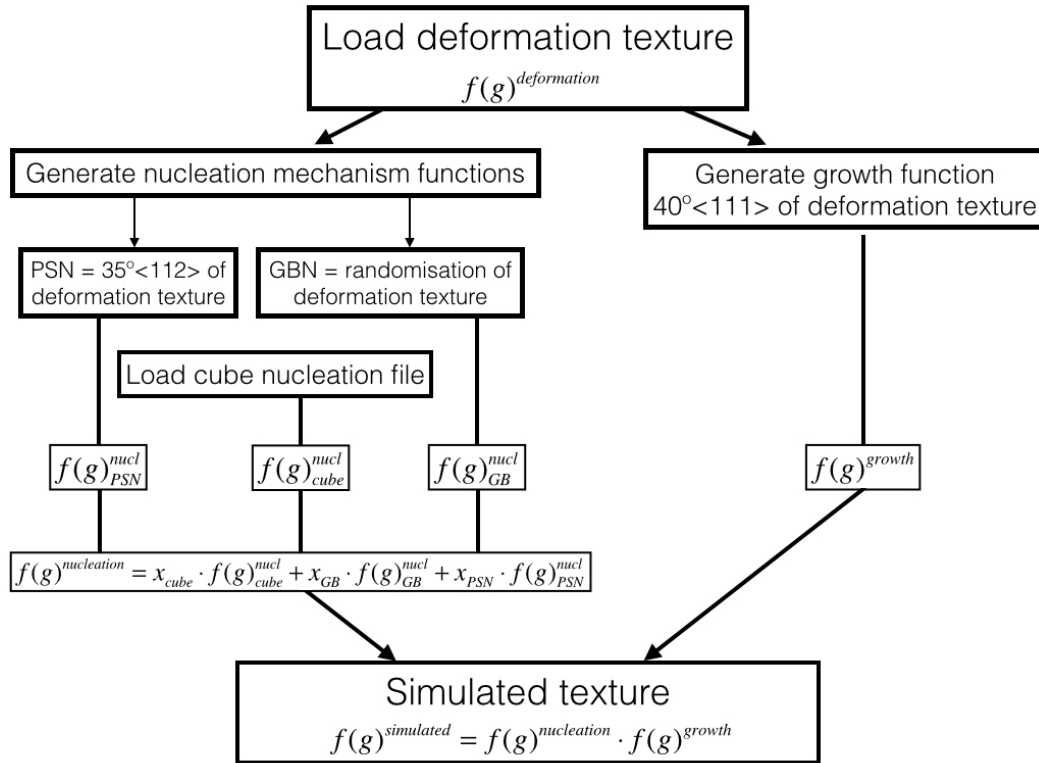
Figure 5.1: Flow chart showing the main concepts of the model and the different steps involved to calculate the recrystallisation texture from deformation texture.

Table 5.1 gives a summary of the maximum ODF values for the different steps in the two models. From this, it is possible to see that *RDB_texture* in all steps will give a higher maximum value. The difference is particularly large when coming to grain boundary nucleation texture. It is noted that the ODF from *RDB_texture* has a maximum intensity close to three times the intensity of the one in the Matlab implementation. The PSN texture is also twice the intensity, but this is also a weak texture component and a difference here will not affect the final recrystallised texture, unless x_{PSN} is large.

Table 5.1: Maximum intensity in ODF's of different functions in both models

ODF	Max ODF intensity Matlab implementation	Max ODF intensity *RDB_texture*
Deformation texture $f(g)^{deformation}$	9.1	10.1
Recrystallisation texture $f(g)^{simulated}$	26.8	32.6
Growth texture $f(g)^{growth}$	2.6	2.9
PSN $f(g)^{nucl}_{PSN}$	1.6	3.4
Grain boundary nucleation $f(g)^{nucl}_{GB}$	5.0	13.6
Cube nucleation $f(g)^{nucl}_{cube}$	44.2	47.8
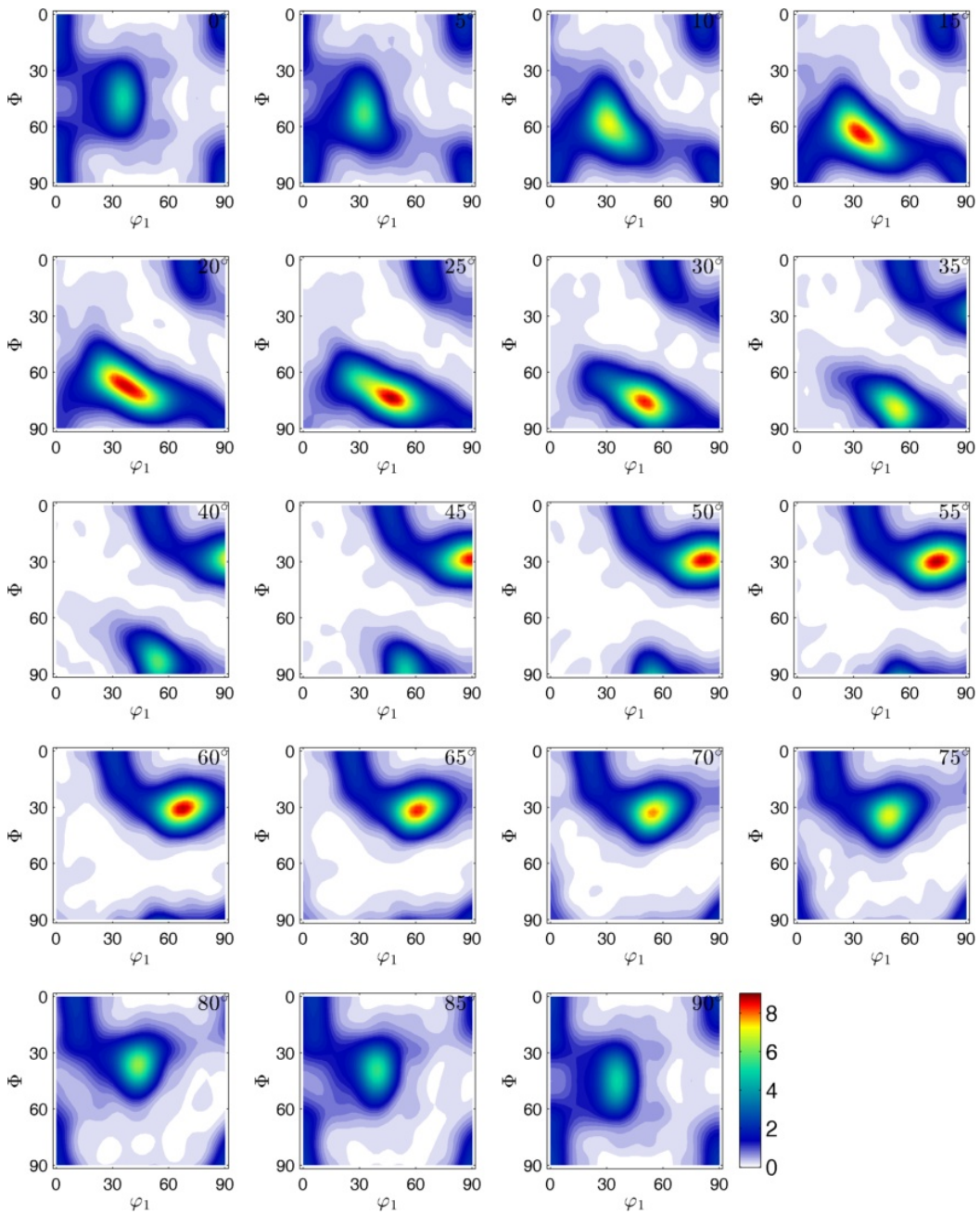
Figure 5.2: ODF of deformed rolled AA3103H18, plotted in Matlab.

An ODF plot of the deformation texture $(f(g)^{deformation})$ is seen in Figure 5.2 and 5.3, respectively plotted in Matlab and *RDB_texture*. These ODF's are plots of the deformed data set, with no alterations, it is therefore expected to be close to identical. When looking at Figure 5.2 and 5.3 it can be seen

that these are more or less the same, only a small difference in intensity. The maximum intensity in the Matlab plot is 9.1 whilst it is 10.1 from the plot in *RDB_texture*.
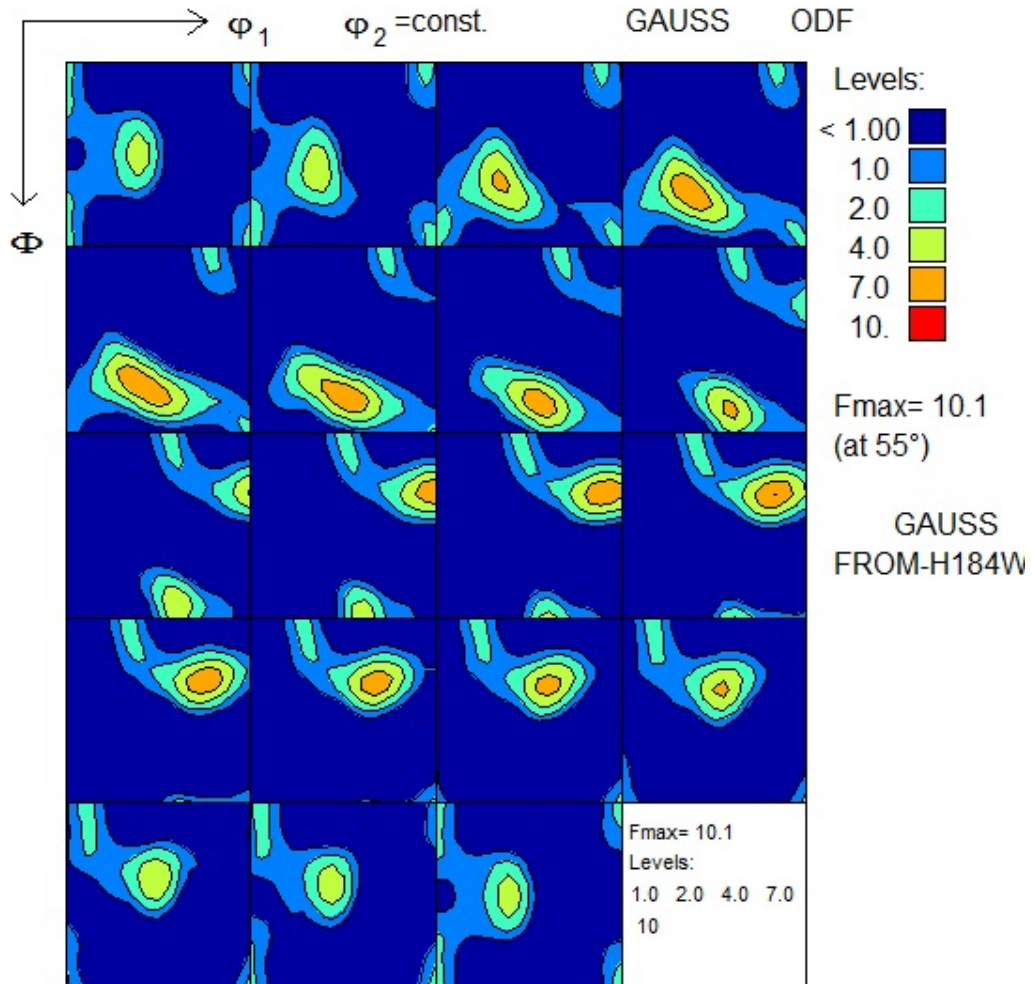
Figure 5.3: ODF of deformed rolled AA3103H18, plotted in *RDB_texture*.
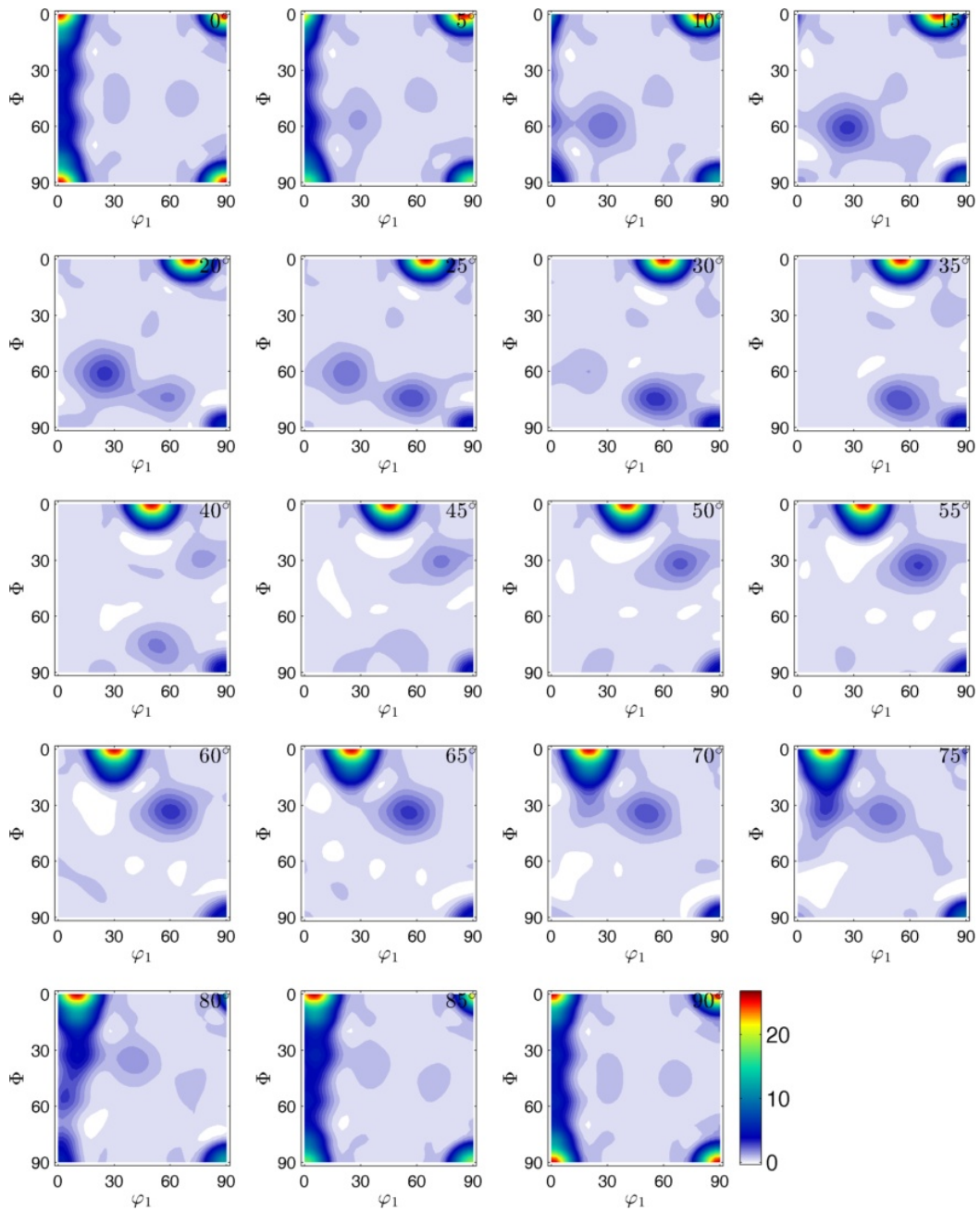
Figure 5.4: ODF of simulated recrystallised rolled AA3103H18, generated in Matlab.

In Figure 5.4 and 5.5 the predicted recrystallised texture $(f(g)^{simulated})$ can be seen. The recrystallised ODF from the Matlab software have a maximum intensity of 26.8, whilst *RDB_texture* have a maximum of 32.6. The two

ODF's were compared by using Equation 2.2 and the GOF value returned was 0.2, this indicates a very good fit between the two. When looking at the two ODF it is clear that all the same components are present in both. For instance, it is possible to trace a fibre which starts to emerge at the coordinates $\varphi_1 = 75°$, $\Phi = 30°$ and $\varphi_2 = 40°$ in both models. This gets stronger in intensity until $\varphi_2 = 65°$ and then fades away at $\varphi_2 = 80°$.
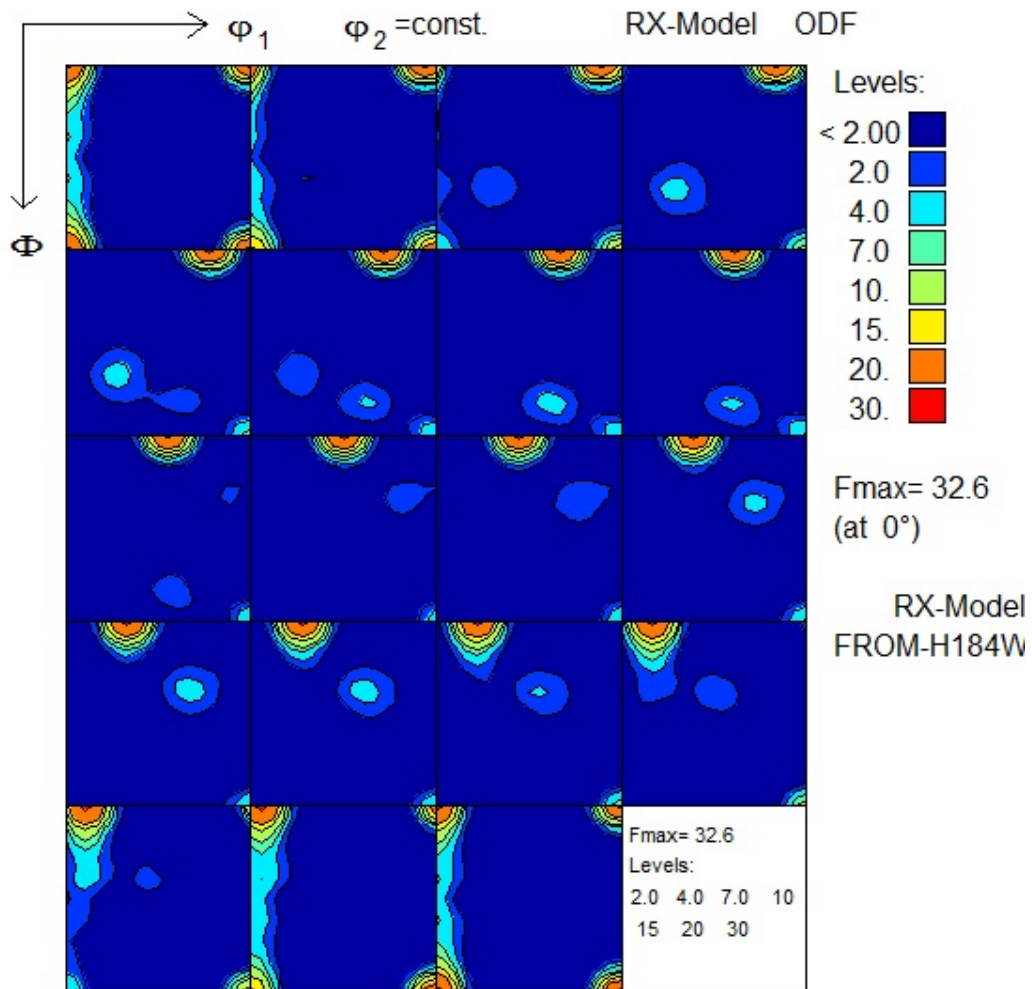
Figure 5.5: ODF of simulated recrystallised rolled AA3103H18, generated in *RDB_texture*.
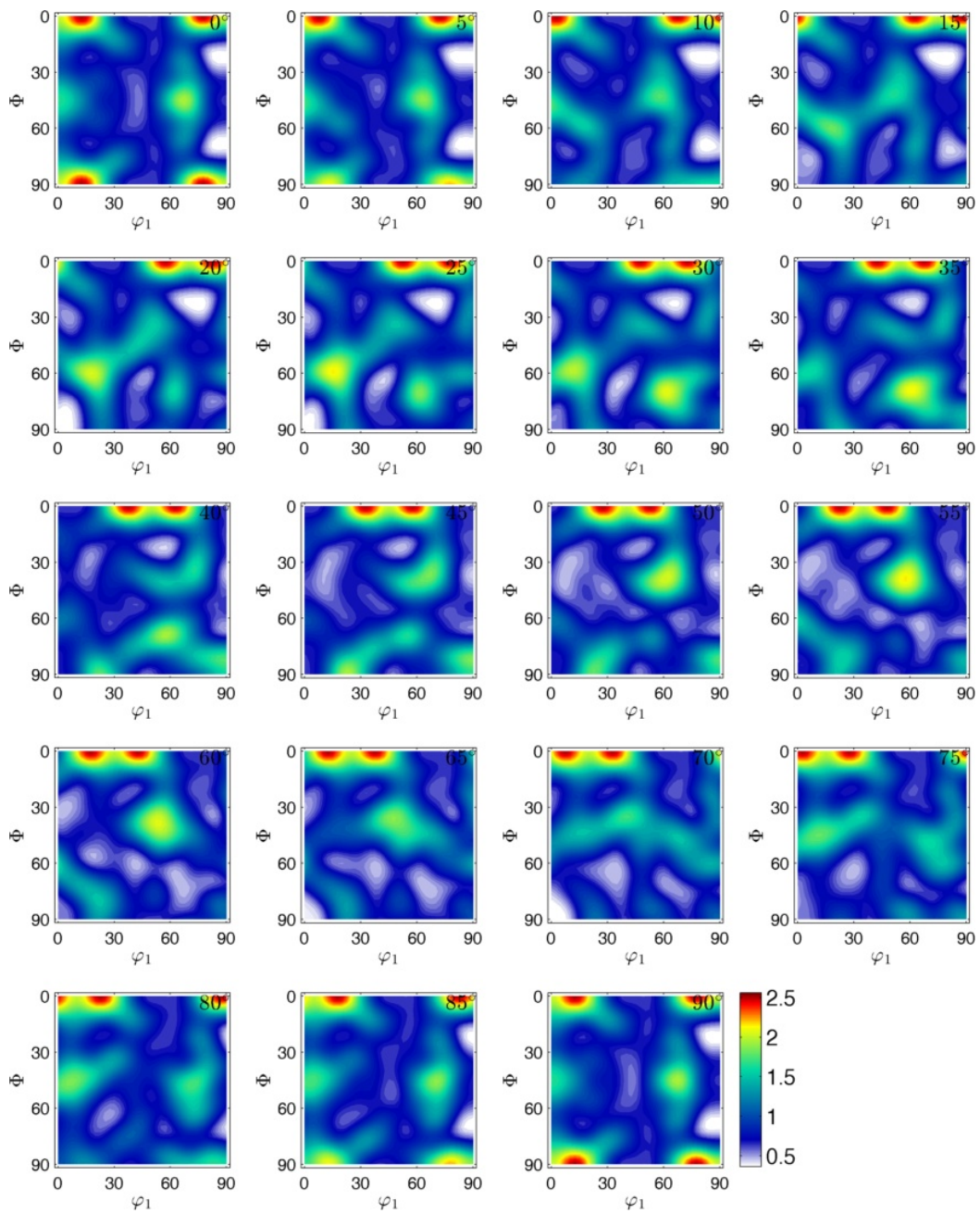
Figure 5.6: ODF of growth function in rolled AA3103H18, generated in Matlab.

The different steps of the two models have also been compared in Figure 5.6-5.13. Here it can be seen that most of them have very similar textures, but may vary in intensity. The growth texture $(f(g)^{growth})$ in Figure 5.6 and 5.7

have roughly the same intensities and also the texture seems to correspond well. Note the difference in colour bars of the two plots. In the Matlab plot yellow would indicate an intensity ~ 2, whilst in *RDB_texture* an intensity of 1 would give the same colour.
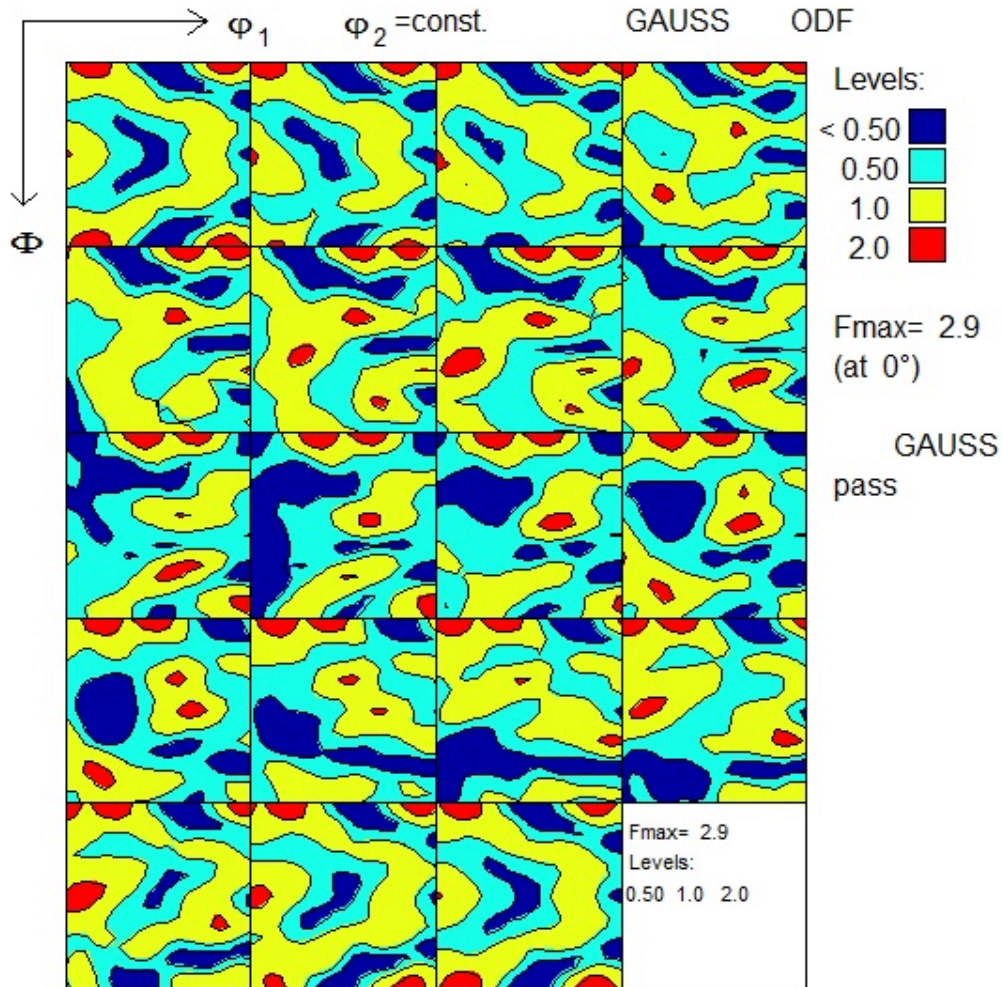
Figure 5.7: ODF of growth function in rolled AA3103H18, generated in *RDB_texture*.
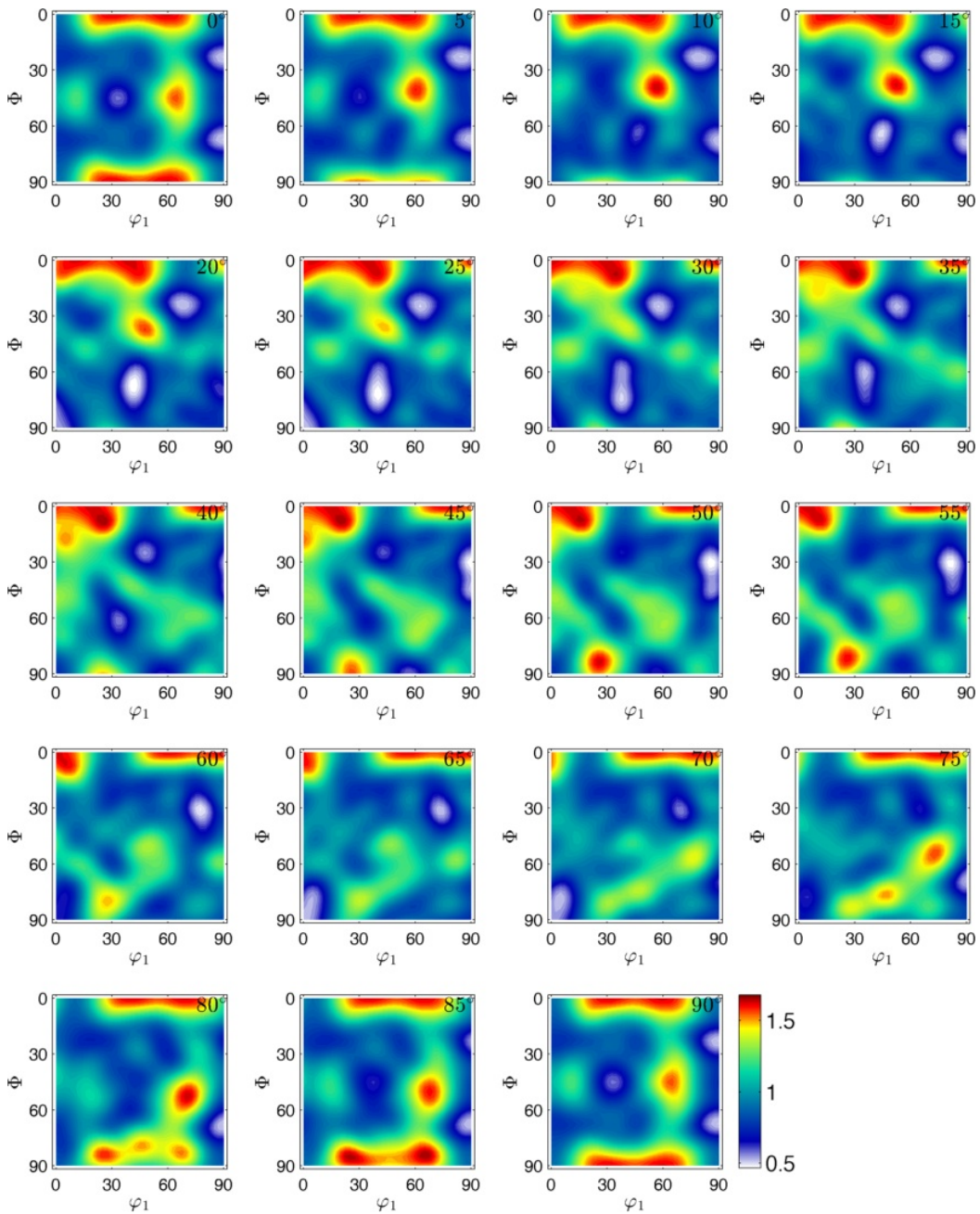
Figure 5.8: ODF of PSN in rolled AA3103H18, generated in Matlab.

The PSN texture $(f(g)_{PSN}^{nucl})$ in both models are displayed in Figure 5.8 and 5.9. When comparing them there are some differences. Looking at Φ = 80°, φ_1 = 25° and φ_2 = 45° -60° it is possible to see a fibre in the Matlab implementation which is only present in the *RDB_texture* generated PSN

56

texture at $\varphi_2 = 45°$. The maximum intensity in the two are low, but in *RDB_texture* it is more than twice the intensity of the Matlab implementation. It is respectively 3.4 and 1.6.
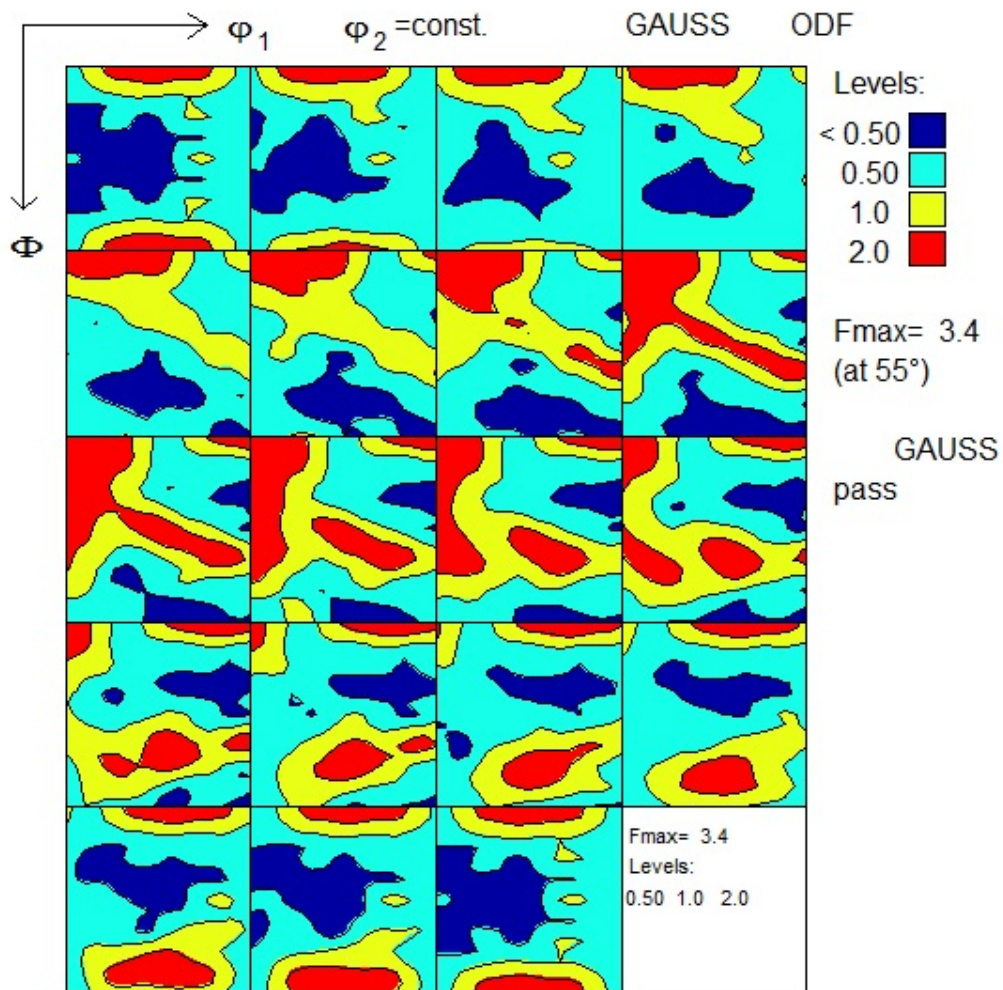
Figure 5.9: ODF of PSN in rolled AA3103H18, generated in *RDB_texture*.
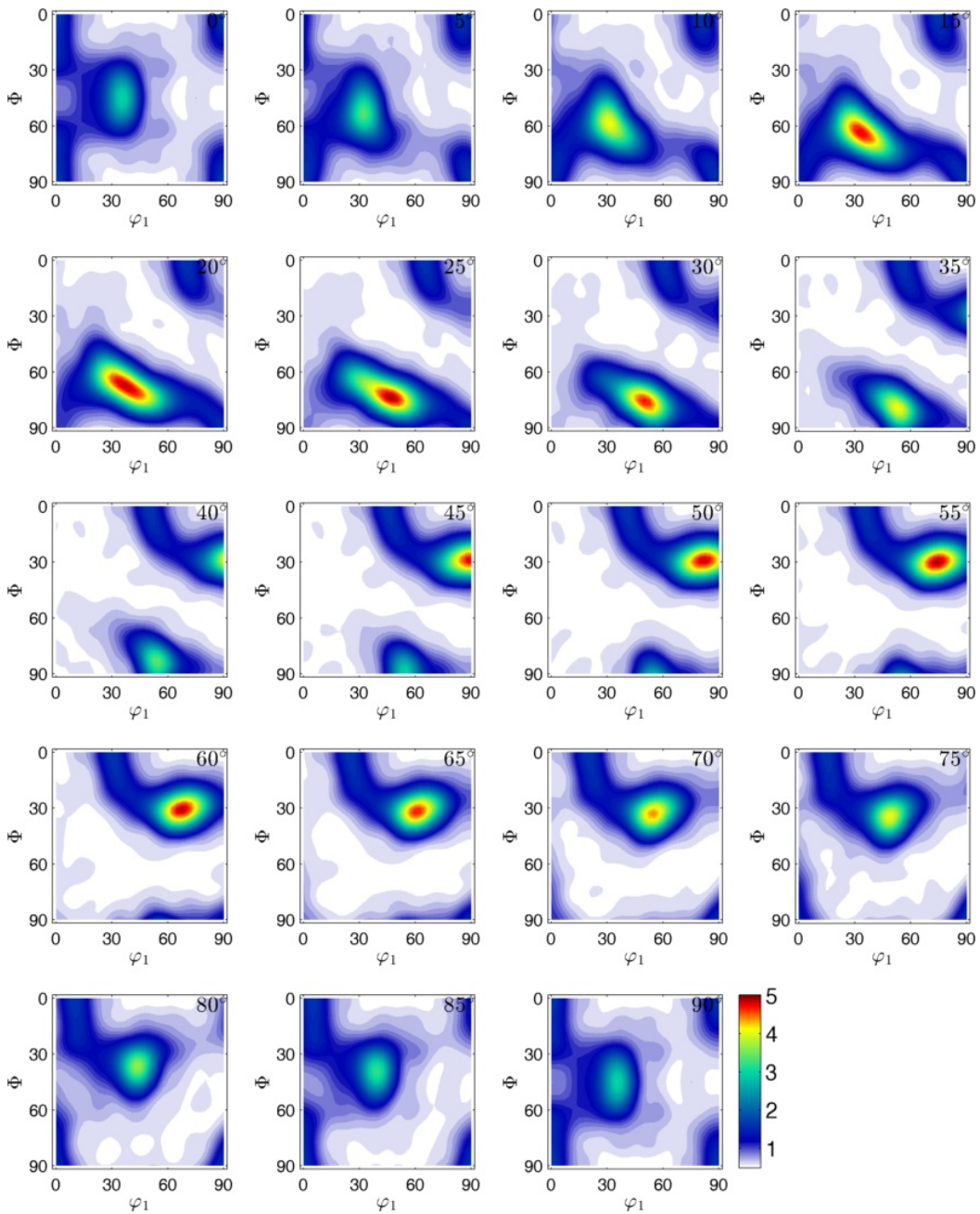
Figure 5.10: ODF of grain boundary nucleation in rolled AA3103H18, generated in Matlab.

In Figure 5.10 and 5.11 the grain boundary nucleation texture $(f(g)_{GB}^{nucl})$ of the two models can be seen. These ODF's seems to have identical texture plots, but in *RDB_texture* the maximum intensity is 13.6 whilst the Matlab

implementation has a maximum intensity of 5. Apart from the differences in intensity, the two ODF's have all the same texture components.
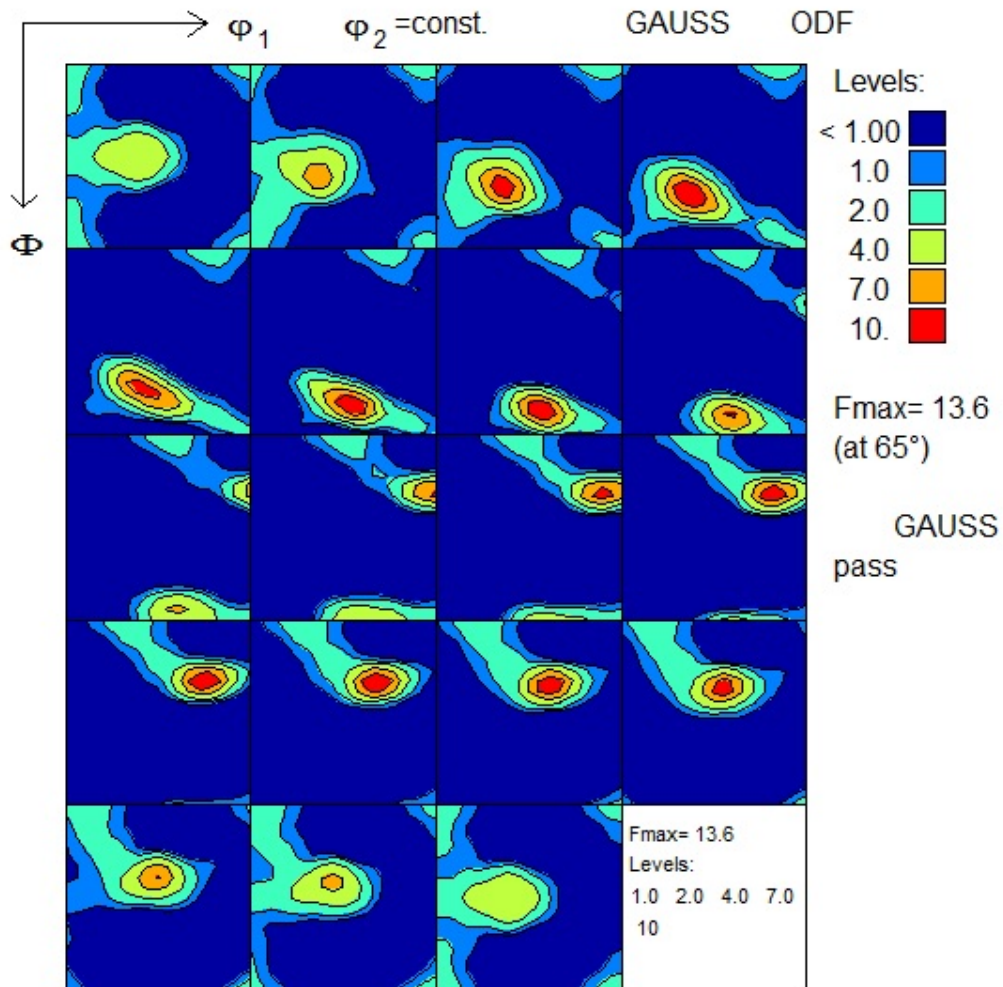
Figure 5.11: ODF of grain boundary nucleation in rolled AA3103H18, generated in *RDB_texture*.
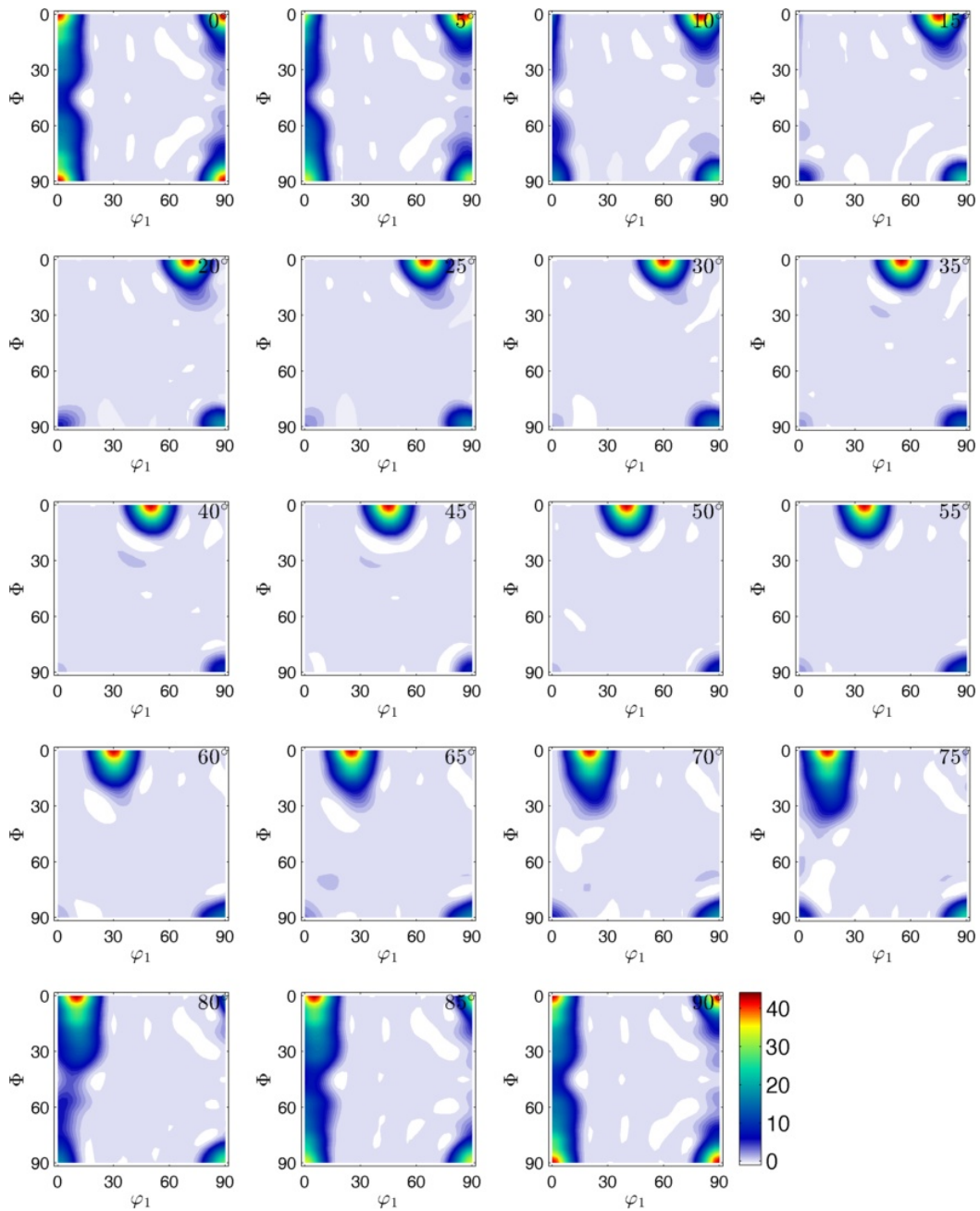
Figure 5.12: ODF of cube nucleation in rolled AA3103H18, plotted in Matlab.

In these models, the cube nucleation texture $(f(g)_{cube}^{nucl})$ is loaded into the software as an external file. The file loaded here is the same in both software. Figure 5.12 is the cube nucleation file plotted in Matlab and the plot in

RDB_texture can be seen in Figure 5.13. When comparing the two plots they are close to identical, as expected. The difference between the two is the intensity, *RDB_texture* has a maximum intensity of 47.8 whilst for the Matlab implementation it is 44.2.
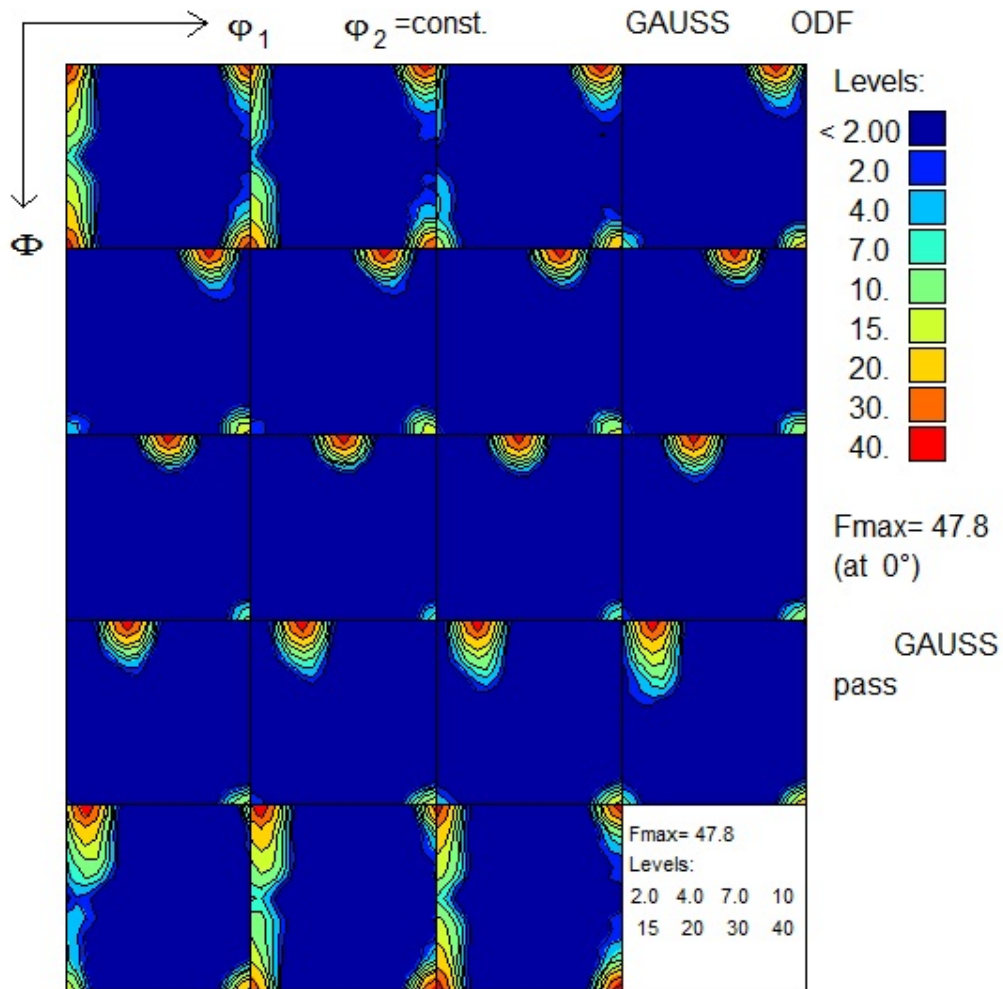
Figure 5.13: ODF of cube nucleation in rolled AA3103H18, plotted in *RDB_texture*.

5.2 Simulated Recrystallised Texture

In Table 5.2 a summary of texture simulations performed with the Matlab implementation of *RDB_texture* is presented. The simulations are mainly just a modelling exercise to see how some systematic variations in weighting factors influence the final recrystallisation texture. The simulated textures were still compared with spontaneously recrystallised B2 and statically recrystallised D04 by using GOF, Equation 2.2. This to see how well the simulated texture compared with experimentally found textures. The returned GOF values are listed in Table 5.2. A lower value indicates a better concordance between the two compared ODF's. These simulations are then used as basis to find the best fort weighting factors in the next section.

Table 5.2: Simulated recrystallisation textures with different weighting factors compared with statically and spontaneously recrystallised samples using GOF

Weighting factors			Maximum ODF	GOF value when compared with	
Cube	GB	PSN	intensity	B2	D04 10s 500°C
1	0	0	42.3	0.5	0.8
0	1	0	30.3	5.2	4.9
0	0	1	7.4	1.4	1.3
0.33	0.33	0.34	15.7	1.2	0.6
0.5	0.5	0	25.5	1.5	0.9
0.5	0	0.5	8	0.7	0.7
0	0.5	0.5	17.3	2.2	1.5

Table 5.3: Texture components present in simulated recrystallisation textures with different weighting factors

Weighting factors			Maximum	Maximum
Cube	GB	PSN	<100> intensity	<111> intensity
1	0	0	29.2	2
0	1	0	1	26.8
0	0	1	2.6	2
0.33	0.33	0.34	3	14.3
0.5	0.5	0	5.5	22.9
0.5	0	0.5	5.5	2.3
0	0.5	0.5	1	15.2

When looking at Table 5.2 and 5.3 it can be seen that cube nucleation gives rise to <100> texture and grain boundary nucleation to <111> texture.

PSN contributes little towards these components. In Figure 5.14, the (100) and (111) pole figures of a simulated texture with 100% PSN are shown. Here it looks like there is a fibre present in the pole figure which is neither <100> or a <111>. The pole figures of 100% cube and 100% grain boundary nucleation (Figure 5.15 and 5.16, respectivly) are typically pole figures of respectively <100> and <111> fibres. The maximum intensity of the two texture components (<100> and <111>) for the different simulations is listed in Table 5.3.
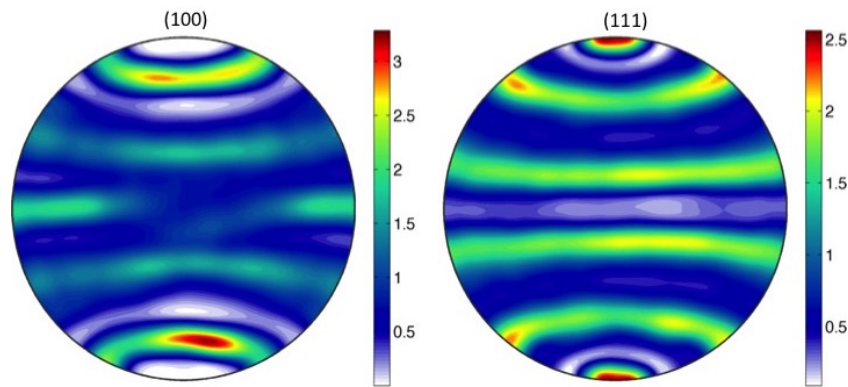
Figure 5.14: (100) and (111) pole figures of simulated recrystallisation texture with 100% PSN as input into the software.
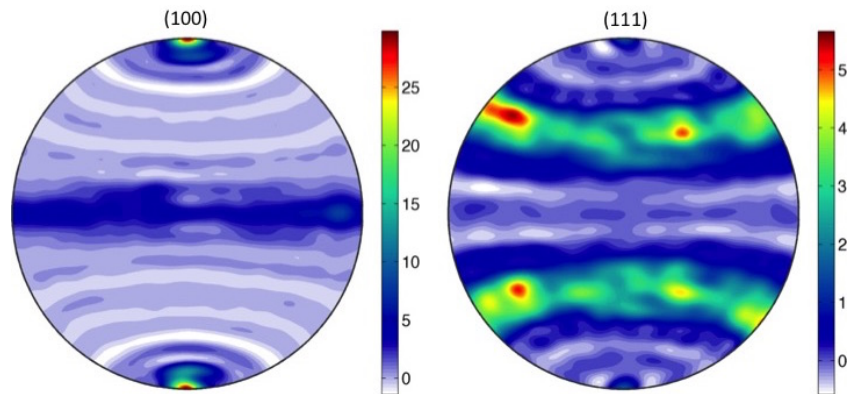
Figure 5.15: (100) and (111) pole figure of simulated recrystallisation texture with 100% cube nucleation as input into the software.
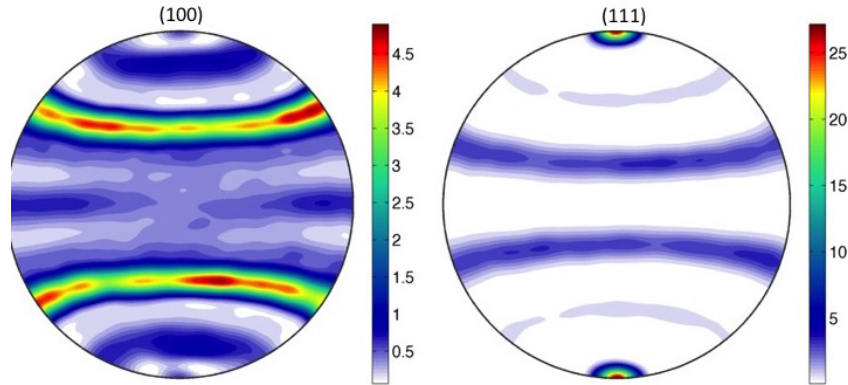
Figure 5.16: (100) and (111) pole figure of simulated recrystallisation texture with 100% grain boundary nucleation as input into the software.

5.2.1 Optimised Weighting Factors for Recrystallisation Texture Simulations

Based on the texture simulations in Section 5.2, the Matlab implementation of *RDB_texture* was run with a number of combinations of weighting factors as input values. Then as in the previous section the simulated texture (in term of its ODF) was compared with experimentally found texture using GOF, Equation 2.2. The result from these simulations can be seen in Table 5.4 and 5.5. Table 5.4 shows how the simulated textures compare with experimentally found textures, the GOF values are listed in the right column. The input weighting factors giving the best fit with the ODF used as reference to the comparison is shown in the columns to the left. In the centre column, the experimentally found texture used as reference is listed.

Table 5.4: ODF comparison for simulated textures.

Weighting factors			ODF's compared	GOF value
Cube	**GB**	**PSN**		
0.90	0.05	0.05	Simulated recrystallisation vs B2	0.5
1.00	0.00	0.00	Simulated recrystallisation vs E24	0.5
0.66	0.32	0.02	Simulated recrystallisation vs D04 heat treated for 610s at 450°C	0.3
0.65	0.21	0.14	Simulated recrystallisation vs D04 heat treated for 10s at 500°C	0.4
0.02	0.15	0.83	Simulated recrystallisation, values from *ALSOFT* vs D04 heat treated for 610s at 450°C	0.8

A lower ODF comparison value (GOF) indicates a better agreement between the compared ODF's. Except for the weighting factors found by using Equation 2.6, 2.7 and 2.8 in *ALSOFT*, PSN seems to be the nucleation mechanism contributing the least. The best agreement between simulated and experimentally found textures is when cube nucleation dominates. The maximum intensities of the two main components <100> and <111>, as well as the overall maximum ODF intensity of the simulated textures are listed in Table 5.5. All the texture plots are attached in Appendix D, but a selection will be presented here to be commentated and compared.

Table 5.5: Summary of simulation texture results

Experimentally found texture used as the comparison	Max <100> Intensity	Max <111> Intensity	Max ODF Intensity
Heat treated D04 610s 450°C	8.5	19.1	21.4
Heat treated D04 10s 500°C	8.8	14.5	15.4
Spontaneously Recrystallised B2	19.2	6.4	28.2
Spontaneously Recrystallised E24	31	2	42.3
Equation 2.6, 2.7 and 2.8 from *ALSOFT*	1.9	6.8	7

In Figure 5.17 and 5.18 the (100) and (111) pole figures of the experimentally found texture of the statically recrystallised D04 (heat treated for 10s at 500°C) and corresponding simulated recrystallisation textures are shown, respectively. The simulated texture was simulated with the nucleation mechanisms giving the best fit when comparing with the heat treated D04 at 500°for 10s. These have a GOF value of 0.4 and the maximum intensities of the ODF's are respectively 7.1 and 15 for the experimentally found and simulated texture. When looking at the weighting factors in Table 5.4 it can be seen that the nucleation mechanism dominating is the cube, but there is also some grain boundary nucleation and PSN present.
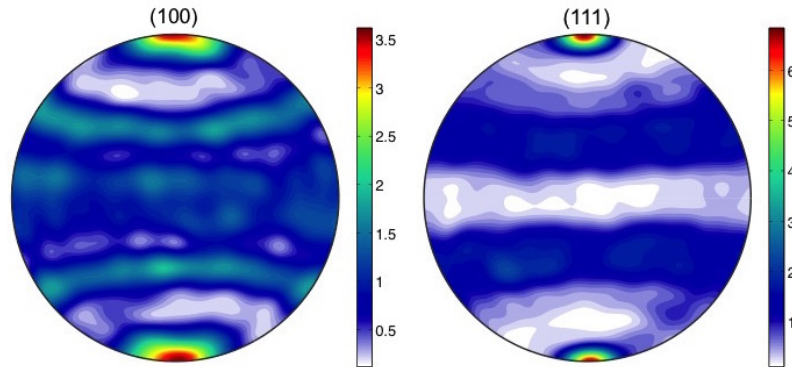
Figure 5.17: Experimental (100) and (111) pole figures of heat treated D04, 10s at 500°C.
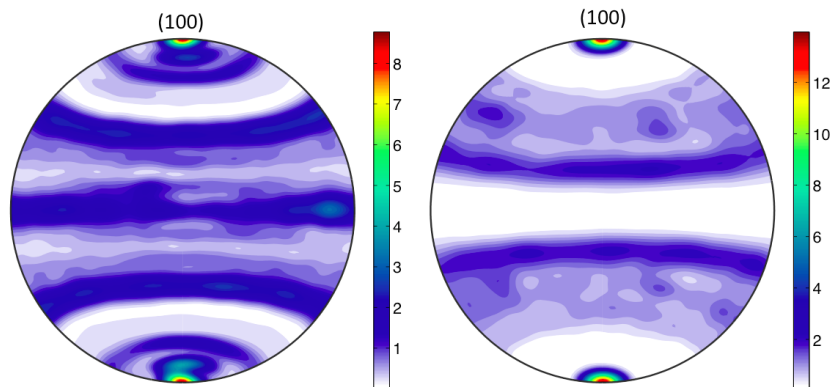
Figure 5.18: Simulated pole figures with D04 10s 500°C as the comparison.

In Figure 5.19 the (100) and (111) pole figures of simulated texture with weighting factors found by using Equation 2.6, 2.7 and 2.8 in *ALSOFT* are shown. The maximum intensities of <100> and <111>-fibres are respectively 1.9 and 6.8 and maximum ODF intensity is 7. This compares well with the texture results of the statically recrystallised samples. When visually comparing these pole figures (Figure 5.19) with the pole figures of the statically recrystallised D04 in Figure 5.17 it can be seen that there are some differences. There is a fibre present in the pole figures in Figure 5.19 which is not present in any experimentally found textures. This is the fibre at the top and bottom of these pole figures.
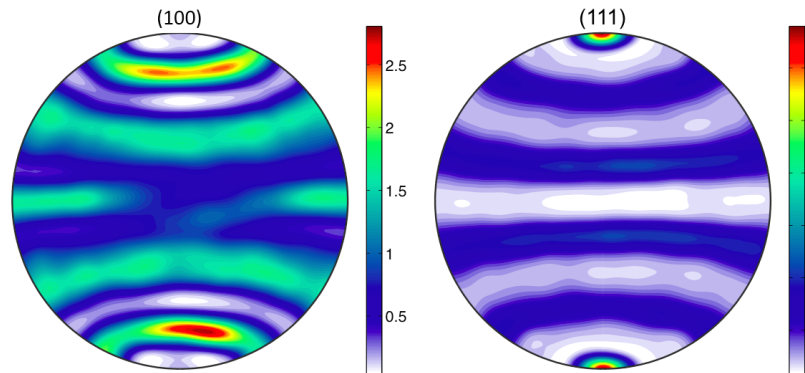
Figure 5.19: Simulated pole figure with weighting factors for nucleation mechanisms found using Equation 2.6, 2.7 and 2.8 with the AA6060 input file in *ALSOFT*.

5.3 *ALSOFT* - Simulated Recrystallised Grain Structure

Figure 5.20 to 5.25 gives the results from *ALSOFT*. These simulations predicts the recrystallisation kinetics and the evolution in recrystallised grain size for the spontaneously recrystallised B2 and statically recrystallised D04 annealed at 450°C and 500°C, respectively. In Figure 5.20, 5.21 and 5.22 the kinetic results can be observed. Here it can be seen that the static recrystallisation at 450°C predicts a fully recrystallised structure after 11s and at 500°C after 2s. This complies reasonably well with experimental results. After 10s at 450°C the structure had an 86.9% recrystallised area fraction and after 10s at 500°C the structure had a 91.5% recrystallised area fraction. The *ALSOFT* simulations for B2 predicted a fully recrystallised structure after 8s. From experimental data it can be seen that this sample recrystallised spontaneously during extrusion.

These graphs also display how the kinetics and grain size vary through the thickness of the profile. The number next to the legend in the graph represent the distance (in μm) from the profile centre being simulated. This means that B2 - 300 will be a simulation of the centre region and B2 - 1350 would represent the sub-surface region. From this, it is possible to see that the model predicts faster recrystallisation close to the surface and this area having a smaller grain size, compared to the centre.

The predicted recrystallised grain size at different section through the thickness of the profile can be seen in Figure 5.23, 5.24 for D04, at the two different temperatures and for B2 in Figure 5.25. It is noted that the annealing tem-
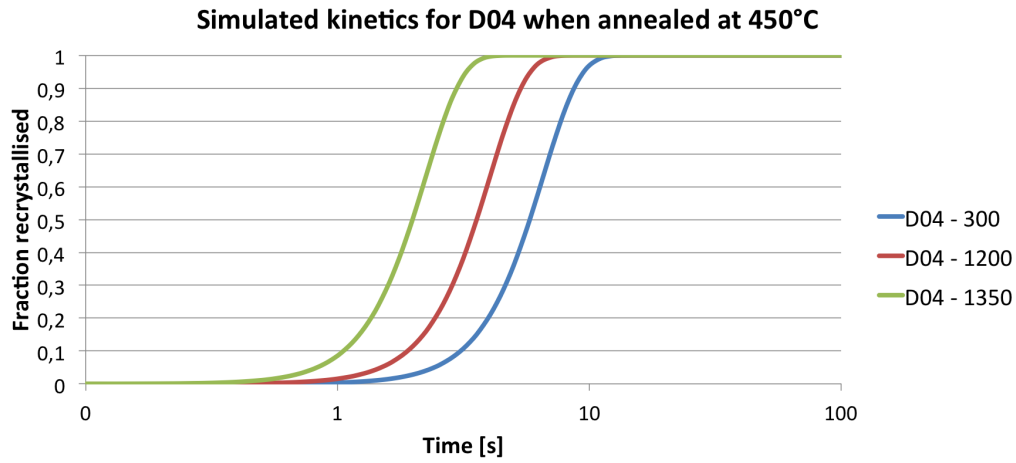
Figure 5.20: Fraction recrystallised from *ALSOFT* simulations with experimental and simulation data obtained for deformed D04 and then annealed at 450°C.
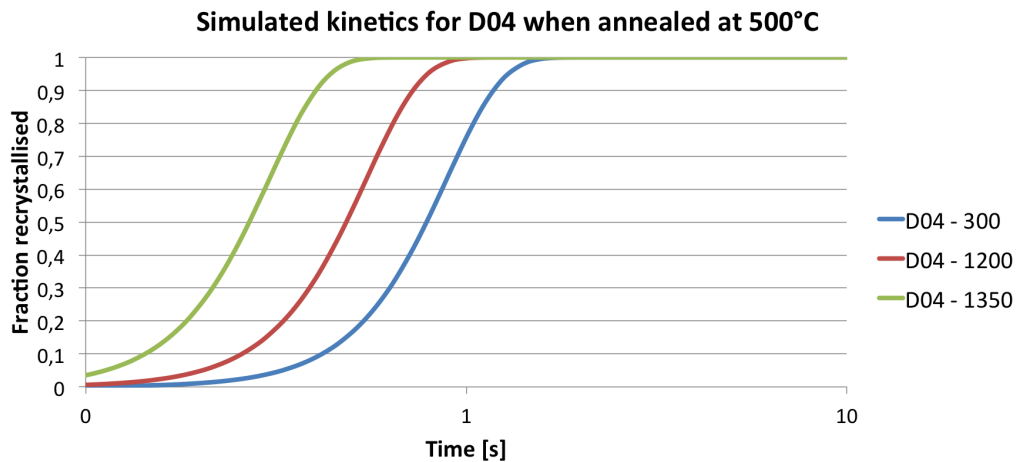
Figure 5.21: Fraction recrystallised from *ALSOFT* simulations with experimental and simulation data obtained for deformed D04 and then annealed at 500°C

perature does not affect the final grain size in *ALSOFT*, only the kinetics. The predicted grain sizes are in the range of 10 μm-38 μm. The experimentally found grain sizes, for spontaneously recrystallised B2 it was 29.5 μm and for statically recrystallised D04 the grain sizes were found to be 27.5 μm and 29.3 μm after annealing at respectively 450°C and 500°C. When annealing at 450°C the reaction finishes in less than 10s, and it takes less than 1s to

fully recrystallise when annealing at 500°C. The predictions for B2 indicates a reaction time between 1s and 8s. This complies well with experimental data.

Simulated kinetics for B2
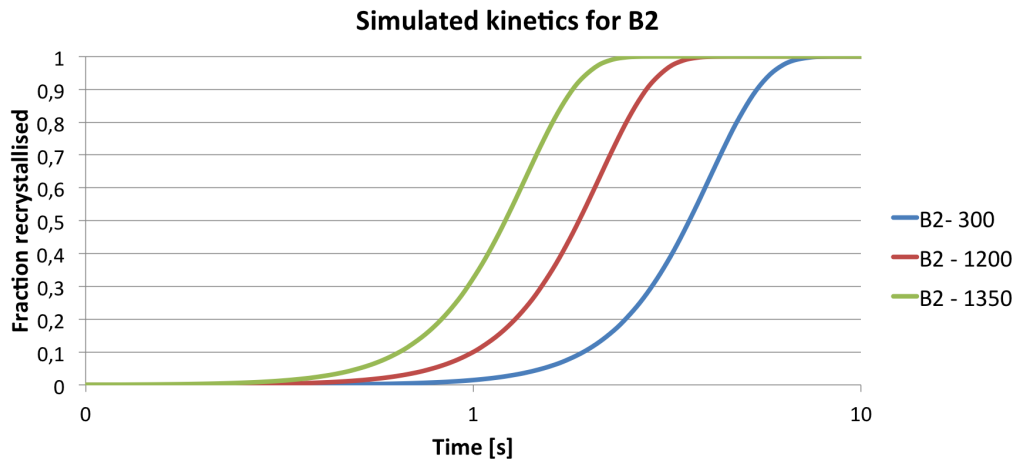
Figure 5.22: Fraction recrystallised from *ALSOFT* simulations with experimental and simulation data obtained for B2.

Simulated grain size for D04 when annealed at 450°C
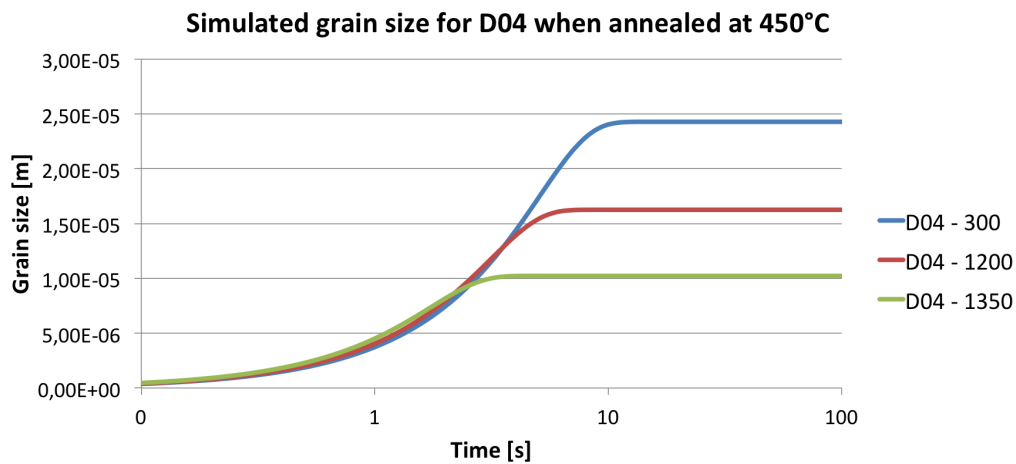
Figure 5.23: Recrystallised grain size simulations from *ALSOFT* with experimental and simulation data obtained for deformed D04 and then annealed at 450°C.
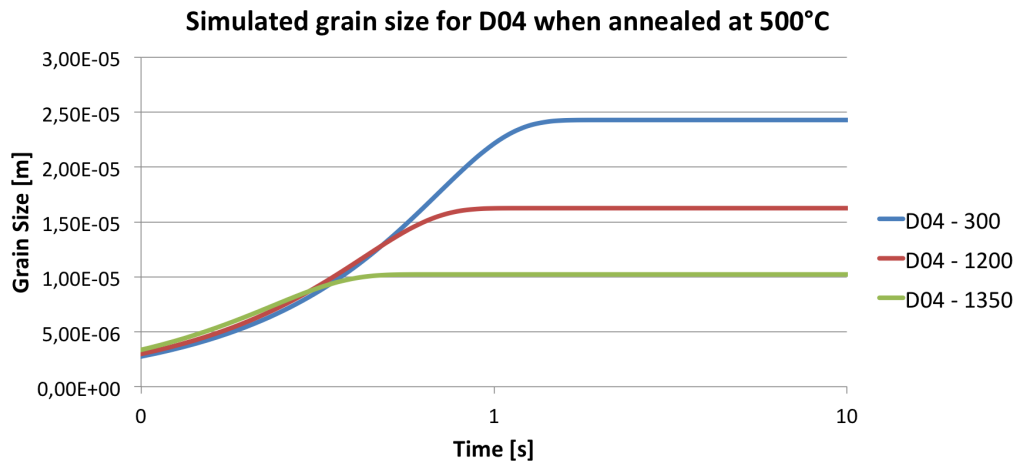
Figure 5.24: Recrystallised grain size simulations from *ALSOFT* with experimental and simulation data obtained for deformed D04 and then annealed at 500°C.
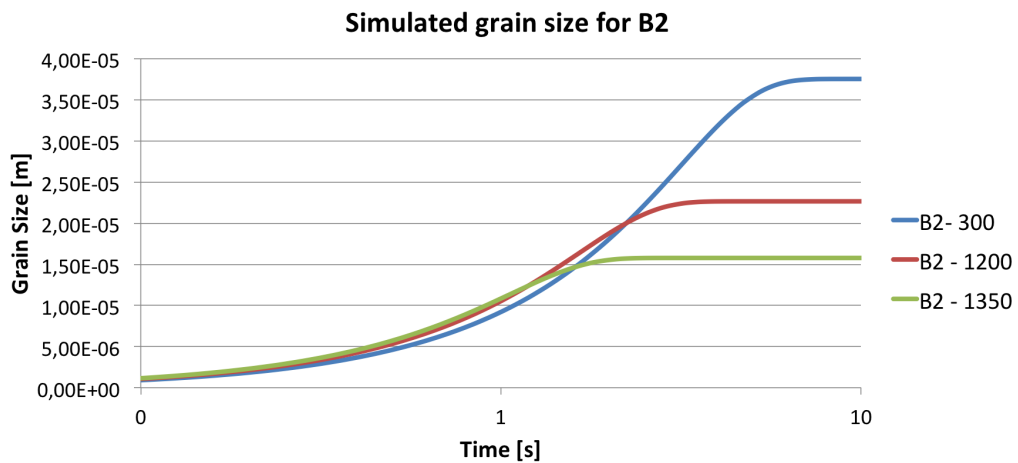
Figure 5.25: Recrystallised grain size simulations from *ALSOFT* with experimental and simulation data obtained for B2.

6 Discussion

In the following section, the result presented previously will be discussed. The experimental results will be compared to each other and with the simulation results. A difference in texture between the spontaneously and statically recrystallised samples were observed. *RDB_texture* was successfully implemented into Matlab and a set of optimised weighting factors for the nucleation mechanisms for this model was found. Finally, the validity of these results will be discussed. The experimental work was performed by using EBSD and settings and user inputs will influence the results obtained. In the model are the fundamental concepts mostly based on empirical relationships found for plain strain conditions (rolling). In this project, these are used for extruded axisymmetric profiles, with little tuning.

6.1 Experimental Results

The experimental results have been summarised in Table 6.1. Here it can be seen that spontaneously recrystallised samples have a strong <100> texture and a weaker <111> texture. The statically recrystallised samples experience the opposite. They have a strong <111> texture and a weaker <100> texture. However, when looking at the grain size and fraction recrystallised of the statically and spontaneously recrystallised samples, it can be seen that they are quite similar. The ODF's of the different recrystallised samples have been compared in Table 6.2 using Goodness of Fit (Equation 2.2). A lower GOF value indicates a similar texture.

Table 6.1: Summary of experimental results

Sample	Max <100> intensity	Max <111> intensity	Max ODF intensity	Recrystallised Area Fraction	Average Grain Diameter μm
E6	11.1	3.5	12.6	90.6%	24.1
B2 - tip	7.7	3	9.6	92%	29.9
B2 - die	8.7	3.4	10.3	91.5	29.2
E24	16.5	4.2	20.4	76.9%	34.9
Deformed D04	4.7	15.2	24.7	-	-
Heat treated D04 10s 450°C	3.9	6	8.8	86.9%	25.3
Heat treated D04 120s 450°C	3.9	6.7	8	87.8%	25.4
Heat treated D04 610s 450°C	3.5	7.2	9.4	89.5%	27.5
Heat treated D04 10s 500°C	3.6	7.2	7.1	91.5%	29.3

Table 6.2: ODF comparison between experimentally found textures

ODF's compared	GOF value
D04 heat treated for 610s at 450°C vs B2	0.7
D04 heat treated for 10s at 500°C vs B2	0.6
D04 heat treated for 610s at 450°C vs D04 heat treated for 10s at 500°C	0.4
E24 vs B2	0.3
E6 vs D04 heat treated for 10s at 500°C	0.6
E6 vs B2	0.2
E6 vs E24	0.3

In Table 6.2, the ODF's of the experimentally found textures are pairwise compared. When the spontaneously recrystallised samples were compared using GOF (Equation 2.2), all of them returned a value in the region of 0.2-0.3. This indicates a good fit and all the samples having similar textures. When looking at the pole figures this was as expected. This since all of the spontaneously recrystallised samples have a strong <100> texture and a weak <111> texture. The spontaneously recrystallised samples were also compared with samples which were recrystallised statically after extrusion. Here the comparison value of GOF were in the range of 0.6-0.7, which is still not to bad.

When comparing the heat treated sample at 500°C for 10s with the sample heat treated for 610s at 450°C, it can be seen that the area fraction recrystallised and grain size is a little larger. The texture of the two samples is very similar. By using GOF, the ODF's of the two samples were compared which returned the value of 0.4 indicating a similar texture of the two samples, as listed in Table 6.2.

In the spontaneously recrystallised sample E24, a region in the centre of the grain map was not recrystallised, seen in Figure 4.18. This area was only ∼2 mm from the die end of the profile and it seems that this fact affects the fraction recrystallised. For B2, which also spontaneously recrystallised during the extrusion a sample was also analysed close to the die, ∼15 mm. When this is compared to a sample from near the tip of the profile there is no clear difference between the two. Both of them have basically the same area fraction recrystallised, grain size and texture. It seems that only parts of the

profile very close to the die is affected, but further out from the die there are small variations across the length of the profile.

As observed, the samples which recrystallised spontaneously and the post-extrusion heat treated samples (static recrystallisation) ended up with different textures. This might indicate different recrystallisation mechanisms (i.e. that dynamic recrystallisation is the operation mechanism) in the spontaneously recrystallised samples. However, the results found in Figure 6.1 and 6.2 seems to refute this. These figures are all from the same region and are taken from the butt-end, just on the inside of the die during the extrusion. In Figure 6.1 a grey scale grain map can be seen with a set of different misorientation boundaries added. The range for each coloured boundary (in terms of misorientation) is described in the legend. In this image, it is possible to see new recrystallised grains and a deformed structure. Two recrystallised grains (i.e. surrounded by high angle grain boundaries) have been circled and as seen, these does not contain any deformed structure. There are only minor misorientations present within the grains, between $0.5°$ and $1°$ at maximum, which can be considered as noise. This is also illustrated by Figure 6.2, from which displays the misorientation across one of the two circled grains in Figure 6.1. This graph it is clear there are very small misorientations within this recrystallised grain, and it seems to be mostly noise. If DRX were to be present it would be expected that the newly recrystallised grains would be in the process of being deformed again, which should show up as significant misorientations in already recrystallised grains.

Another observation which also weigh against DRX is that the recrystallised grains are spatially distributed (have nucleated at different locations in the material) and have grown independently to fairly large size, which more resembles classical static recrystallisation than DRX. This means that the recrystallised grains in Figure 6.1 (from the butt-end) and in spontaneously recrystallised extruded profiles in general are a result of very fast recrystallisation during cooling of the extruded profiles. This is also consistent with the predicted very fast recrystallisation kinetics by *ALSOFT* for B2 in Section 5.3, just seconds, which allows the profiles to be recrystallised as it typically takes a few seconds before the profiles are quenched after exiting the die after extrusion.
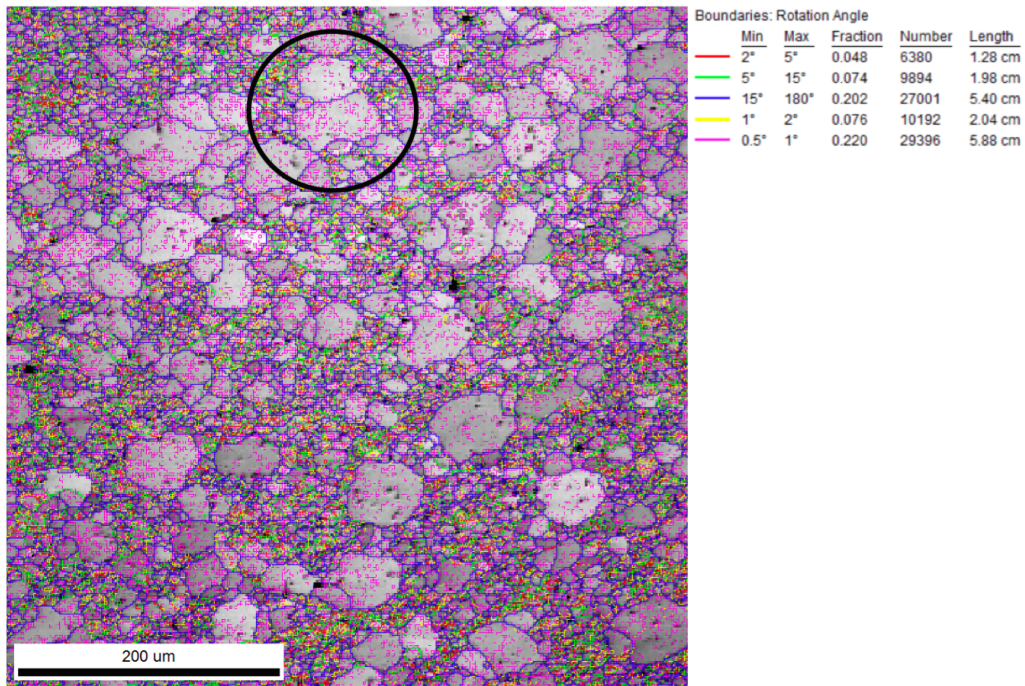
Figure 6.1: Grey scale image of the butt-end of B2, obtained by EBSD with boundaries with different rotation angles added. Figure courtesy of SINTEF, with Tanja Pettersen.
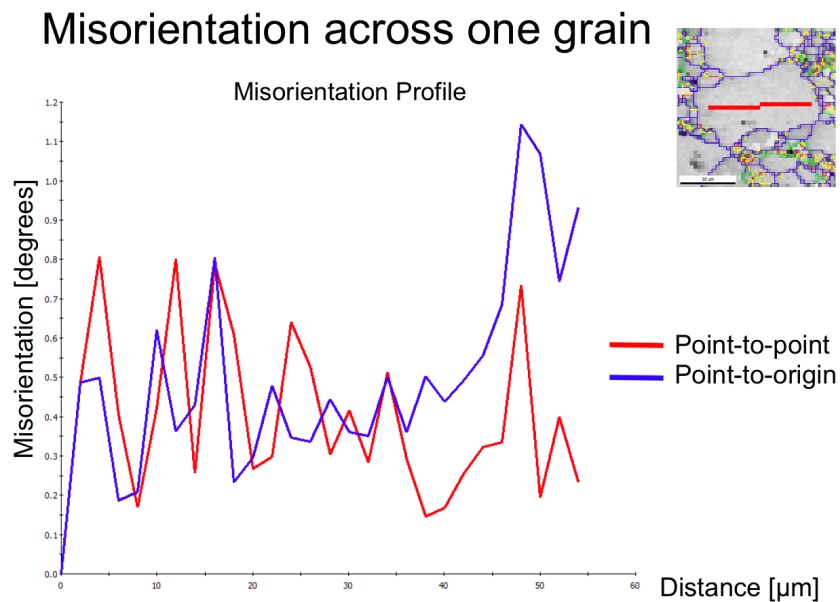
Figure 6.2: Misorientation across one grain, the grain is circled in Figure 6.1. Figure courtesy of SINTEF, with Tanja Pettersen.

6.2   Simulation Results

The simulations have been performed with a Matlab implementation of *RDB_texture*. This implementation seems to give the same recrystallisation texture as the original software. The software has been running with a number of different combinations of all weighting factors and the simulated recrystallised textures were compared with different experimentally found recrystallisation textures, in terms of ODF's using the GOF. These results are listed in Table 6.3. The first columns are with the optimised weighting factors, the middle is the recrystallised texture used as a reference and the last is the GOF value returned by Equation 2.2. In Table 6.4 the maximum intensity of the two main texture components, <100> and <111>-fibres, of the simulations with optimised weighting factors are listed.

Table 6.3: ODF comparison for simulated textures.

Weighting factors			ODF's compared	GOF value
Cube	**GB**	**PSN**		
0.90	0.05	0.05	Simulated recrystallisation vs B2	0.5
1.00	0.00	0.00	Simulated recrystallisation vs E24	0.5
0.66	0.32	0.02	Simulated recrystallisation vs D04 heat treated for 610s at 450°C	0.3
0.65	0.21	0.14	Simulated recrystallisation vs D04 heat treated for 10s at 500°C	0.4
0.02	0.15	0.83	Simulated recrystallisation, values from *ALSOFT* vs D04 heat treated for 610s at 450°C	0.8

Table 6.4: Summary of simulation results

Simulation Reference	Max <100> Intensity	Max <111> Intensity	Max ODF Intensity
Heat treated D04 610s 450°C	8.5	19.1	21.4
Heat treated D04 10s 500°C	8.8	14.5	15
Spontaneously Recrystallised B2	19.2	6.4	28.2
Spontaneously Recrystallised E24	31	2	42.3
Equation 2.6, 2.7 and 2.8 from *ALSOFT*	1.9	6.8	7

Looking at the difference between the experimentally found textures and the simulated texture some differences can be found. The greatest difference is

in the intensities. In general the intensities are larger for simulated textures. Comparing the values in Table 6.1 and Table 6.4, it is easy to see that the intensities are much higher for the simulated textures. In texture simulations, this is a known issue and a general problem when simulating recrystallisation textures. The exception in the present work is for the simulations with the weighting mechanism predicted by *ALSOFT*. In the pole figures in Figure 5.19, there seems to be texture components which are not being present in the experimental results. It is also based on having mainly PSN as main nucleation mechanism in an alloy containing little primary particles.

The optimised weighting factors found by comparing simulated with experimentally found recrystallisation textures can be seen in Table 6.3. From this, it is possible to see that spontaneously recrystallised samples had the best fit with the simulated texture with close to 100% of cube nucleation as input into the model. Statically (post-extrusion) recrystallised samples have a best fit with 65% cube nucleation and 30% grain boundary nucleation and a small portion of PSN.

The simulations by the Matlab implemented *RDB_texture* seems to correspond well with the results in *RDB_texture*. Both models seem to give the same texture for all the steps in the model as well as the final recrystallised texture. The only difference is in the intensities, the largest difference was for the grain boundary nucleation texture. Here the maximum intensity was more than two times the size in *RDB_texture*. The source for this might be due to the way the two software perform their operations. There might be some unidentified normalisation during the ODF calculations by *RDB_texture*, which is not included when using Matlab and MTEX to do the calculations.

ALSOFT simulations predicted smaller grain size and faster recrystallisation in the region of the profile close to the surface and larger grains and slower recrystallisation in the centre. This complies well with experimental data. For B2 *ALSOFT* predicts a grain size in the range of 16 μm-38 μm and the experimentally found average grain diameter was found to be 29.9 μm. The predicted recrystallised grain size for statically recrystallised D04 was from 10 μm-24 μm, whilst is was experimentally found to be 27.5 μm and 29.3 μm. The reaction time for B2 was predicted to be between 1s and 8s, experimental results ended up with a fully recrystallised structure during the extrusion process. For D04, the predicted reaction time was 3s to 10s and less than 2s for annealing respectively at 450°C and 500°C. The experimental results showed that annealing for 10s at 450°C gave 86.9% recrystallised area fraction and when looking at its grain map (Figure 4.4) it is possible to see that the structure is close to fully recrystallised. When annealing at 500°C for 10s the sample was fully recrystallised with a recrystallised area fraction

of 91.5%. In general the *ALSOFT* predictions were quite accurate. This is gratifying, but also somewhat surprising given that limited re-tuning of the model has been done for the particular alloy and processing condition used in this work.

6.3 Validity of Results

All experimental data from the samples in this project have been obtained by using EBSD. As described in Section 2.5 it is important to do all the analysis with the same settings on the SEM and in the EBSD software. In this project, all settings for the analysis have been the same and all the values in Table 6.1 would be comparable to each other. However, the exact numbers in this table might not be comparable to numbers obtained in another project.

All of the fundamental concepts in *RDB_texture* and consequently in the Matlab implementation are based on empirically found relationships. In the model, a data set containing texture data from a deformed sample is loaded and manipulated into several orientation distribution functions. These functions are then added and multiplied to get the simulated texture. The concepts were, in addition, developed for rolling (plain strain deformation conditions) and not extrusion. As been shown in this report, there seems to be indications of some different nucleation mechanisms present during recrystallisation in extruded profiles.

The predicted recrystallisation texture is in general quite good, but the texture intensities are twice the intensity of the experimental data. When looking at the weighting factors found it can be seen that the best ODF comparison value is found with a large fraction of cube nucleation. For comparison with spontaneously samples (B2 and E24), the best fit is found with only cube nucleation. In the statically recrystallised samples, $\sim$30% of the nucleation seem to be due to grain boundary nucleation and 65% due to cube nucleation. These results seem reasonable and the texture compares well with the experimentally found textures (Table 6.3).

The *ALSOFT* results gave a recrystallised grain size in the range of 10 μm-38 μm, depending on the stored energy. This seems to correspond quite well with the experimental results. They have an overall average grain diameter of $\sim$29 μm. When looking at the kinetic results from the simulations, they predict a fully recrystallised structure after 10s when heat treating at 450°C. D04 was heat treated at this temperature for 120s and did not achieve a fully, but close to a recrystallised structure. The experimental results in this report compare qualitatively well with the simulated results from *ALSOFT*, although, as already mentioned above, no proper tuning has been made for

the particular alloy and processing conditions used here. It should also be re-emphasised here, the *ALSOFT* model is developed for rolling, where the nucleation and growth mechanisms may be different from what is during axisymmetric extrusion.

7 Conclusion

This thesis has combined experimental and modelling work in order to try and get a better understanding of recrystallisation mechanisms in extruded axisymmetric aluminium profiles. The main conclusion from this project will be presented in the following section.

7.1 Conclusions Based on Experimental Results

For the experimental work, a set of spontaneously and statically recrystallised samples have been analysed by using EBSD. The texture, grain size and recrystallised area fraction of these samples have been compared in order to get an understanding about the recrystallisation mechanisms. The results from this investigation points in the direction of a difference in nucleation mechanisms of statically and spontaneously recrystallised samples, rather than dynamical recrystallisation taking place. The following are the main conclusion from the EBSD investigation:

- Statically recrystallised samples at different temperatures and times have a very similar texture, grain size and recrystallised area fraction.

- Grain size and recrystallised area fraction found in statically and spontaneously recrystallised samples are relatively similar.

- The texture of spontaneously recrystallised samples and statical recrystallised D04 are different.

    - Spontaneously recrystallised samples seems to have only cube band nucleation, whilst statically recrystallised samples also have some grain boundary nucleation in addition.
    - This might indicate different nucleation mechanisms.

- Newly recrystallised grains in the butt-end, just at the inside of the die, does not seem to be in the process of being re-deformed during the extrusion process.

    - This indicates that the recrystallisation process is static recrystallisation, and not dynamic recrystallisation.

- Except for the area closest to the die, there seem to be no variations across the profile length when it comes to grain structure and texture.

7.2 Conclusions Based on Modelling Results

A Matlab version of *RDB_texture* has been created for the modelling part of this thesis. This Matlab implementation have been used to simulated recrystallisation textures with different weighting factors for different nucleation mechanisms (from rolling) as input values. The simulated textures were compared with experimentally found textures. In general, the simulations showed a stronger texture than the experimentally found ones. However, this is also a known issue when simulating recrystallisation textures. The main conclusions for the texture modelling are the following:

- Successfully implemented *RDB_texture* in Matlab

- The optimised weighting factors found when comparing with statically recrystallised D04 at different temperatures were very similar. These were mainly cube nucleation ($\sim$65%), with some grain boundary nucleation ($\sim$30%) and little PSN.

- The optimised weighting factors found when comparing with spontaneously recrystallised B2 and E24 predicted only cube nucleation.

- The nucleation mechanisms in *ALSOFT* does not seem to be fully adequate for axisymmetric extruded profiles. Predicts a very large proportion of PSN, this is not likely due to few primary particles present in this alloy.

ALSOFT was used to simulated the recrystallised grain size and recrystallisation kinetics for D04 annealed at 450°C and 500°C and B2. The results from the model gave results resembling the experimentally found results. The predicted grain size and reaction time varied through the profile thickness, which also compared well with was found in the experiments.

7.3 Suggestions for Further Work

- Look further into static recrystallisation to identify nucleation mechanisms in extrusion.

  - This can be done by analysing the deformation structure even more closely to try to identify see from where the recrystallised nucleus form.

- Based on experimental findings, further develop and change the nucleation mechanisms in both *ALSOFT* and texture recrystallisation models accompanying.

References

[1] *aluMATTER applications,* `http://aluminium.matter.org.uk/content/html/eng/default.asp?catid=2&pageid=995466854`, Accessed: 2015-05-27.

[2] O. Reiso, "Extrusion of almgsi alloys," in *Materials Forum,* vol. 28, 2004, pp. 32–46.

[3] J. K. Solberg, "Teknologiske metaller og legeringer," *Institutt for materialteknologi, NTNU,*

[4] F. J. Humphreys and M. Hatherly, *Recrystallization and Related Annealing Phenomena.* 2002.

[5] R. Hu, T. Ogura, H. Tezuka, T. Sato, and Q. Liu, "Dispersoid formation and recrystallization behavior in an al-mg-si-mn alloy," *Journal of Materials Science & Technology,* vol. 26, no. 3, pp. 237–243, 2010.

[6] L. Lodgaard and N. Ryum, "Precipitation of dispersoids containing mn and/or cr in al–mg–si alloys," *Materials Science and Engineering: A,* vol. 283, no. 1, pp. 144–152, 2000.

[7] G. E. Dieter and D. Bacon, *Mechanical metallurgy.* 1986, vol. 3.

[8] G. Gottstein, "Physical foundations of materials science," 2004.

[9] B. Verlinden, J. Driver, I. Samajdar, and R. D. Doherty, *Thermomechanical processing of metallic materials.* Elsevier, 2007, vol. 11.

[10] P. K. Saha, *Aluminum extrusion technology.* Asm International, 2000.

[11] J. Hjelen, R. Ørsund, and E. Nes, "On the origin of recrystallization textures in aluminium," *Acta metallurgica et materialia,* vol. 39, no. 7, pp. 1377–1404, 1991.

[12] O. Engler, "Nucleation and growth during recrystallisation of aluminium alloys investigated by local texture analysis," *Materials science and technology,* vol. 12, no. 10, pp. 859–872, 1996.

[13] W. Leslie, J. Michalak, and F. Aul, "The annealing of cold-worked iron," *Iron and its Dilute Solid Solutions, Interscience Puhlishers, New York,* 1963.

[14] Y. Wu, H. Liao, J. Yang, and K. Zhou, "Effect of si content on dynamic recrystallization of al–si–mg alloys during hot extrusion," *Journal of Materials Science Technology,* vol. 30, no. 12, pp. 1271 –1277, 2014.

[15] H. McQueen, O. Knustad, N. Ryum, and J. Solberg, "Microstructural evolution in al deformed to strains of 60 at 400c," *Scripta Metallurgica,* vol. 19, no. 1, pp. 73 –78, 1985.

[16] M. E. Kassner, *Fundamentals of creep in metals and alloys*. Elsevier, 2008.

[17] *aluMATTER forming*, `http://aluminium.matter.org.uk/content/html/eng/?catid=175&pageid=2144416783`, Accessed: 2015-05-27.

[18] B. Verlinden, J. Driver, I. Samajdar, and R. D. Doherty, *Thermomechanical processing of metallic materials*. Elsevier, 2007, vol. 11.

[19] H. J. Bunge, "Zur darstellung allgemeiner texturen," *Zeitschrift fur metallkunde*, vol. 56, no. 12, p. 872, 1965.

[20] H. J. Bunge and P. R. Morris, "Texture analysis in materials science: Mathematical methods," 1982.

[21] O. Engler and V. Randle, *Introduction to texture analysis: Macrotexture, microtexture, and orientation mapping*. CRC press, 2009.

[22] V. Randle and O. Engler, *Introduction to texture analysis: Macrotexture, microtexture and orientation mapping*. CRC Press, 2000.

[23] J. Hjelen, "Scanning elektron-mikroskopi," 1989.

[24] N. Gao, S. C. Wang, H. S. Ubhi, and M. J. Starink, "A comparison of grain size determination by light microscopy and ebsd analysis," *Journal of materials science*, vol. 40, no. 18, pp. 4971–4974, 2005.

[25] G. Vander Voort and H. James, "Asm handbook, vol. 9," *Metallography and Microstructures, ASM International, OH*, 2004.

[26] F. Reidenbach, "Finishing methods, asm handbook, vol. 05," *Surface Engineering, ASM International,*, 1994.

[27] H. E. Vatne, T. Furu, R. Ørsund, and E. Nes, "Modelling recrystallization after hot deformation of aluminium," *Acta materialia*, vol. 44, no. 11, pp. 4463–4473, 1996.

[28] H. E. Vatne, R. Ørsund, K. Marthinsen, and E. Nes, "Modeling recrystallization kinetics, grain sizes, and textures during multipass hot rolling," *Metallurgical and Materials Transactions A*, vol. 27, no. 12, pp. 4133–4144, 1996.

[29] J. Saeter, B. Forbord, H. E. Vatne, and E. Nes, "Modelling recovery and recrystallization, applied to back-annealing of aluminium sheet alloys," in *ICAA-6: 6 th International Conference on Aluminium Alloys, Toyohashi, Japan, 5-10 Japan 1998*, 1998, pp. 113–126.

[30] N. Wang, K. Huang, and K. Marthinsen, "Modelling recovery and recrystallization behavior of cold-rolled al-mn-fe-si-alloys with different micro-chemistries," in *To be submitted*, 2014.

[31] K. Marthinsen, S. Abtahi, K. Sjolstad, and E. Nes, "Modeling the micro-structural evolution during hot rolling and subsequent cold rolling and annealing of an aa 3103 alloy," in *Materials Forum*, vol. 28, 2004, pp. 933–938.

[32] O. Engler, L. Löchte, and J. Hirsch, "Through-process simulation of texture and properties during the thermomechanical processing of aluminium sheets," *Acta Materialia*, vol. 55, no. 16, pp. 5449–5463, 2007.

[33] O. Daaland and E. Nes, "Recrystallization texture development in commercial almnmg alloys," *Acta Materialia*, vol. 44, no. 4, pp. 1413 –1435, 1996.

[34] *aluMATTER pinning of grain boundaries and zener drag*, `http://aluminium.matter.org.uk/content/html/ENG/default.asp?catid=68&pageid=1042033829`, Accessed: 2015-05-27.

[35] E. Nes, "Modelling of work hardening and stress saturation in fcc metals," *Progress in Materials Science*, vol. 41, no. 3, pp. 129–193, 1997.

[36] K. Marthinsen and E. Nes, "Modelling strain hardening and steady state deformation of al–mg alloys," *Materials science and technology*, vol. 17, no. 4, pp. 376–388, 2001.

[37] E. Nes and K. Marthinsen, "Modeling the evolution in microstructure and properties during plastic deformation of fcc-metals and alloys–an approach towards a unified model," *Materials Science and Engineering: A*, vol. 322, no. 1, pp. 176–193, 2002.

[38] E Nes, K Marthinsen, and B Holmedal, "The effect of boundary spacing on substructure strengthening," *Materials science and technology*, vol. 20, no. 11, pp. 1377–1382, 2004.

[39] A Seeger, "The mechanism of glide and work-hardening in face-centered cubic and hexagonal close-packed metal," *Dislocations and Mechanical Properties of Crystals. J. Wiley, New York*, 1957.

[40] J Friedel, "International series of monographs on solid state pysics, dislocations," 1964.

[41] O. Engler, "Simulation of the recrystallization textures of al-alloys on the basis of nucleation and growth probability of the various textures components," *Textures and microstructures*, vol. 28, no. 3, pp. 197–210, 1997.

[42] O. Engler, "A simulation of recrystallization textures of al-alloys with consideration of the probabilities of nucleation and growth," *Textures and microstructures*, vol. 32, no. 1-4, pp. 197–219, 1999.

[43] K. Lücke and O. Engler, "Effects of particles on development of microstructure and texture during rolling and recrystallisation in fcc alloys," *Materials Science and Technology*, vol. 6, no. 11, pp. 1113–1130, 1990.

[44] P. A. Beck, "Notes on the theory of annealing textures," *Acta Metallurgica*, vol. 1, no. 2, pp. 230 –234, 1953.

[45] K. T. Kashyap and R. George, "Mechanism of cube grain nucleation during recrystallization of deformed commercial purity aluminium," *Bulletin of Materials Science*, vol. 29, no. 2, pp. 197–200, 2006.

[46] *MTEX mtex toolbox home page*, `http://mtex-toolbox.github.io`, Accessed: 2015-05-27.

[47] D. Mainprice, R. Hielscher, and H. Schaeben, "Calculating anisotropic physical properties from texture data using the mtex open-source package," *Geological Society, London, Special Publications*, vol. 360, no. 1, pp. 175–192, 2011.

[48] L. S. Tóth and J. J. Jonas, "Modelling the texture changes produced by dynamic recrystallization," *Scripta metallurgica et materialia*, vol. 27, no. 3, pp. 359–363, 1992.

[49] J. J. Jonas and L. S. Toth, "Modelling oriented nucleation and selective growth during dynamic recrystallization," *Scripta metallurgica et materialia*, vol. 27, no. 11, pp. 1575–1580, 1992.

[50] *Struers Safety Data Sheet electrolyte a2*, `http://www.struers.com/ default.asp?top_id=3&main_id=199&doc_id=377&target=_self& admin_language=2`, Accessed: 2015-05-27.

[51] J. Friis and B. Holmedal, "Modelling of the microstructure evolution during and after extrusion using alflow and alsoft on particle paths from hyperxtrude," *Confidential*, 2008.

[52] *Private communication.*

[53] E. Nes, "Recovery revisited," *Acta metallurgica et materialia*, vol. 43, no. 6, pp. 2189–2207, 1995.

[54] E. Nes, "Constitutive laws for steady state deformation of metals, a microstructural model," *Scripta metallurgica et materialia*, vol. 33, no. 2, pp. 225–231, 1995.

[55] K. Zhang, B. Holmedal, O. S. Hopperstad, and S. Dumoulin, "Modelling the plastic anisotropy of aluminum alloy 3103 sheets by polycrystal plasticity," *Modelling and Simulation in Materials Science and Engineering*, vol. 22, no. 7, pp. 75 015–75 034, 2014.

A *ALSOFT*

Alsoft equations - Site saturation version

NTNU, Trondheim 10.12.2014

Knut Marthinsen

1. Evolution equation

$$\frac{d\rho_i(t)}{dt} = -v_D b A_\rho B_\rho \rho_i(t)^{3/2} \exp\left(-\frac{U_a}{RT(t)}\right) 2\sinh\left(\frac{A_\rho Gb^4 \sqrt{\rho_i(t)}}{kT(t)}\right). \tag{1}$$

$$\frac{d\delta(t)}{dt} = v_D b A_\delta B_\delta \exp\left(-\frac{U_a}{RT(t)}\right) 2\sinh\left(\frac{A_\delta Gb^4}{kT(t)}\frac{1}{\delta(t)}\right). \tag{2}$$

$$\frac{dr(t)}{dt} = V(t) \tag{3}$$

Radial growth velocity of spheraical recrystallized grains:

$$V(t)) = M(t)\left[P_D(t) - P_Z(t)\right] \tag{4}$$

$$M(t) = \frac{M_0}{c_{ss}R(t)}\exp\left(-\frac{U_{RX}}{RT(t)}\right) \tag{5}$$

Driving pressure for recrystallization

$$P_D(t) = a\frac{g_{SB}}{d(t)} + \frac{1}{2}Gb^2 r_i(t) \tag{6}$$

$$\gamma_{SB} = \frac{Gb\theta}{4\pi(1-v)}\ln\left(e\frac{\theta_c}{\theta}\right) \tag{7}$$

Shear modulus:

$$G = G_0\exp(-G_1 T) \tag{8}$$

The quantites A_d and A_r in Eq. (1) and (2)

$$A_\delta = w_\delta \left(c_{ss}^{eff} \right)^{-e_\delta}$$

$$A_\rho = w_\rho \left(c_{ss}^{eff} \right)^{-e_\rho}$$

2. Quantities derived from the current state

$$X(t) = 1 - \exp(-X_{ext}(t))$$

$$X_{ext}(t) = \frac{4pr(t)^3}{3} N_{tot} \tag{13}$$

Mean size of recrystallized grains

$$D = \left(\frac{X}{N_{tot}} \right)^{1/3} \tag{14}$$

Total density of nucleationsites for recrystallization calculated at $t = 0$ ($T = T_{def}$)

$$N_{Tot} = N_C + N_{GB} + N_{PSN} \tag{10}$$

Density of nucleation sites for cube grains

$$N_{Cube} = \overline{\delta}_C A(\varepsilon) R_S (1 - R_C) S_C^*$$

$$A(e) = 2 \frac{R_c}{D_0} \left(\exp(e) + \exp(-e) + 1 \right)$$

$$R_c = R_c^0 R_{cA} (R_{cB} + R_{cC}\varepsilon)^{R_{cD}} \left(R_{cE} \ln(Z) + R_{cF} \right)^{R_{cG}}$$

$$R_s = \begin{cases} R_{sA} + R_{sB}\varepsilon, & \varepsilon < R_{sC} \\ R_{sA} + R_{sB}R_{sB}, & otherwise \end{cases}$$

$$S_c^* = \begin{cases} \dfrac{\exp(5\delta^*/\overline{\delta}_c)}{\delta^3}\displaystyle\sum_{n=0}^{4}(5\delta^*/\overline{\delta}_c)^n, & 0 \le \delta^*/\overline{\delta}_c \le 15 \\ 0, & otherwise \end{cases}$$

$$\overline{\delta}_c = f_c\delta(0)$$

$$\delta^* = \frac{4\gamma_{GB}}{P_D(0) - P_Z(0)}$$

Density of grain boundary nucleation sites

$$N_{GB} = 2\frac{C_{GB}\delta(0)(1-R_c)S_{GB}^*}{D_0}\left(\exp(\varepsilon) + \exp(-\varepsilon) + 1\right)$$

$$S_{GB}^* = S_c^*$$

Density of particle stimulated nucleation sites

$$N_{PSN} = C_{PSN}N_0\exp(C_{PE}L\eta^*)$$

$$\eta^* = \frac{4\gamma_{GB}}{P_D(0) - P_Z(0)}$$

Yield stress:

$$R_{p0.2}(t) = R_{FLP} + \left[\alpha_1 MGb\sqrt{\rho_i(t)} + \alpha_2 MGb\frac{1}{\delta(t)}\right]\left[1 - X(t)\right]$$

3. Other useful relations

Initial values for r_i and d as a function of $R_{p0.2}$

$$\rho_i = \left(f_\rho \frac{R_{p0.2} - R_{FLP}}{\alpha_1 MGb} \right)^2$$

$$\delta = \frac{1}{1 - f_\rho} \frac{\alpha_2 MGb}{R_{p0.2} - R_{FLP}}$$

Initial values for r_i and d as a function of the Zener Hollomon parameter Z. The following equation is solved itearively

$$\frac{1}{\delta} = \frac{RT_{def}}{A_s} \ln\left(\frac{Z\delta^2}{B_s} \right)$$

$$\rho_i = \left(\frac{C_1}{\delta} \right)^2$$

Zener drag as a function of particle volume fraction f_p and the mean particle radius r_p (where C_{PZ} is tuning constant close to unity)

$$P_Z(t) = C_{PZ} \frac{3}{2} \frac{f_p(t) g_{GB}}{r_p(t)}$$

Zener-Hollomon parameter:

$$Z = \dot{\varepsilon} \exp\left(\frac{U_{ZH}}{RT_{def}} \right)$$

Effective solid solution content (weigted with activation enegies for diffusion)

$$c_{ss}^i = \frac{w_{ss}^i / A_r^i}{\sum_j w_{ss}^j / A_r^j} = \frac{W_{ss}^i / A_r^i}{\sum_j W_{ss}^j / A_r^j} \qquad c_{ss} = c_{ss}^0 + \sum_i c_{ss}^i \exp\left(\frac{U_a}{U_i} \right)$$

Tables of symbols used in this report. The corresponding parameter names used in the input file *alsoft.inp* are also listed.

A.1 Physical constants

Symbol	Name	Value	Unit	Description
k	kB	$1.3806503 \cdot 10^{-23}$	J/K	Boltzmann's const.
NA	NA	$6.02214199 \cdot 10^{23}$	mol^{-1}	Avogadro's constant
R	Rgas =	kNA	J/(mol K)	Molar gas constant

A.2 State variables

Symbol	Name	Description
ρ_i	rho i	Interior dislocation density, m^{-2}
δ	delta	Mean subgrain size, m
r	r	Radius of recrystallised grains, m

A.3 External parameters (time dependent)

Symbol	Name	Description
t	time	Time, s
T	T	Temperature, K
css	Css	Effective solid solution content, at. fraction
PZ	PZ	Zener drag, Pa

Table 1 *ALSOFT* input parameters

Bitflag for mode selection, currently unused...	as_mode		0
Initial dislocation density (#/m^2)	rho_i		4.81E+11
Initial subgrain size (m)	delta		2.88E-06
Initial recrystallised grain size (m)	r		0
Friction stress (MPa)	R_FLP		5.30E+01
Constant in evolution eq. for dislocation density	B_rho		3.5E+06
Constant in evolution eq. for dislocation density	w_rho		0.5
Constant in evolution eq. for subgrain size	B_delta		0.275
Constant in evolution eq. for subgrain size	w_delta		5
Constant in expr. for density of particle stimulated	N0		3E+15
Constant in particle size distribution (1/m)	L		1.34E+06
Prefactor for mobility (m^4/s)	M0		0.5E+03
Initial (as-cast) grain size (m)	D0		1.00E-04
Constant in evolution eq. for subgrain size	e_delta		0.6667
Constant in evolution eq. for dislocation density	e_rho		0.6667
Constant in strength model	alpha1		0.22
Constant in strength model	alpha2		2.1
Taylor factor	Mtaylor		3
Burgers vector (m)	b		2.86E-10
Debye frequency (1/s)	nu_D		1.00E+13
Grain boundary energy (J/m^2)	gamma_GB		0.3
Constant in expr. for density of particle stimulated	CPE		1.2
Prefactor for density of particle stimulated nucleat	C_PSN		0.6
Constant in expr. for density of grain boundary nucl	C_GB		0.12
Geometric constant in driving pressure for recrystal	alpha		2.5
Missorientation (Deg.)	theta		4
Constant for missorientation (Deg.)	theta_c		15
Poisson number	nu		0.33
Initial volume fraction of cube grains	R_c0		0.1
Constant in expr. for density of cube nucleation sit	C_Cube		0.15
Scale factor for mean cube grain size	fCube		1.3
Constant in expr. for volume fraction cube grains	R_cA		1
Constant in expr. for volume fraction cube grains	R_cB		1
Constant in expr. for volume fraction cube grains	R_cC		0
Constant in expr. for volume fraction cube grains	R_cD		1
Constant in expr. for volume fraction cube grains	R_cE		0.06
Constant in expr. for volume fraction cube grains	R_cF		-0.15

Constant in expr. for volume fraction cube grains	R_cG		-1.8
Constant in expr. for fraction S deformation texture	R_sA		0.04
Constant in expr. for fraction S deformation texture	R_sB		0.173
Constant in expr. for fraction S deformation texture	R_sC		2
Eff. activation energy for solute diffusion (J/mol)	U_a		2.00E+05
Activation energy for recrystallisation (J/mol)	U_rex		1.6E+05
Prefactor in expr. for shear modulus (Pa) [2.99e10]	G0		2.65E+10
Exp. factor in expr. for shear modulus (K^-1) [5.4e-	G1		0
Temperature during initial deformation (C)	T_def		373
Zener drag during initial deformation (Pa)	PZ_def		0
True strain after initial deformation	strain_def		2
Zener-Holomon parameter (1/s)	Z		4E+10
Particle radius [m]	rp		1
Volume fraction particles	fr		0.001

B   *ALFLOW*

The work-hardening model, version warm

1. The system of equations.

1.1   *The representation of the microstructure*

A three–parameter approach is made:

ρ_i :   Average dislocation density in the interior of the subgrains

δ :   Average diameter of the subgrains

φ :   Average misorientation of the dislocations across the subgrain boundaries

The following variables may be derived, the second one is not directly applied:

$$\rho = \rho_i + \kappa_0 \varphi/(b\delta)$$
   :   Average density of dislocations stored in the material

$$f\rho_b = \begin{cases} fq_b^2\rho_i = f\rho_i + \kappa_0\varphi/(b\delta) & \text{in stage II} \\ \kappa_0\varphi/(b\delta) & \text{above stage II} \end{cases}$$
   :   The dislocation density within the subgrain boundaries

Below we will first express the critical shear stress as a autonomous function of the microstructure variables. Then we will supply the equations for the evolution of the microstructure in strain (or time).

1.2   *The effective solute core concentration,* c_{sc} *, (Dynamic Strain Ageing).*

$$c_{sc} = c_0 + c + (c_{ss} - c)f_s$$

$$c_{ss} = c \exp\left(\frac{\Delta U_{sc}}{kT}\right)$$

$$f_s = f_s\left(\frac{D_s}{vb}\right) = 1 - \exp\left(-\left(\frac{D_s}{vb}\right)^{n_{sc}}\right)$$

$$D_s = B_{sc}b^2\nu_D \exp\left(-\frac{U_{sd}}{kT}\right)$$

$$v = \frac{\dot{\gamma}}{b\rho_m} = \frac{\dot{\gamma}}{bm\rho}$$

1.3   *The critical shear stress as a function of the microstructure*

The resolved shear stress is divided into four contributions

$$\tau = \tau_t + \tau_p + \alpha_1 Gb\sqrt{\rho_i} + Gb\alpha_2\left(\frac{1}{\delta} + \frac{1}{D}\right)$$

D	:	Average grain diameter
τ_t	:	Thermal short-range interactions between mobile dislocations and stored ones
τ_p	:	Non-deformable particles

τ_t is obtained from the Orowan equation $\dot{\gamma} = \rho_m b\mathbf{v}$ with $\rho_m = m\rho$, and the velocity v given by (for pure metals (*pm*) and solid solution alloys (*s*), respectively).

$$\mathbf{v}^{(pm)} = l_{at}^{(pm)} B_t^{(pm)} v_D \exp\left(-U_t^{(pm)}/kT\right) 2\sinh\left(\frac{V_t^{(pm)}\tau_t^{(pm)}}{kT}\right)$$

$$\mathbf{v}^{(s)} = l_{at}^{(s)} B_t^{(s)} v_D \exp\left(-U_t^{(s)}/kT\right) 2\sinh\left(\frac{V_t^{(s)}\tau_t^{(s)}}{kT}\right)$$

And it follows that:

$$\tau_t^{(pm)} = \left(\frac{kT}{V_t^{(pm)}}\right)\text{arcsinh}\left[\frac{(\dot{\gamma}/v_D)\exp\left(U_t^{(pm)}/kT\right)}{2bl_{at}^{(pm)}\rho_m B_t^{(pm)}}\right]$$

$$\tau_t^{(s)} = \left(\frac{kT}{V_t^{(s)}}\right)\text{arcsinh}\left[\frac{(\dot{\gamma}/v_D)\exp\left(U_t^{(s)}/kT\right)}{2bl_{at}^{(s)}\rho_m B_t^{(s)}}\right]$$

Finally we choose the solution having the smallest frequency, i.e. the smallest velocity v.

$$\tau_t = \begin{cases} \tau_t^{(s)} & \text{if } solute \\ \tau_t^{(pm)} & \text{if pure metal} \end{cases}$$

The following expressions are needed:

$$l_{at}^{(pm)} = b, \qquad V_t^{(pm)} = \frac{\omega_\rho}{\sqrt{\rho}} b^2 \qquad \text{and } U_t^{(pm)} = U_{SD} \text{ (“Self diffusion”).}$$

$$l_{at}^{(s)} = \frac{b^2 c_{sc}}{l_s^t}^{-1} = \frac{b}{\omega_t c_{sc}^{1-e_t}}, \quad V_t^{(s)} = l_s^t b^2 = \omega_t c_{sc}^{-e_t} b^3 \quad \text{and } U_t^{(s)} = U_s + \Delta U_s \text{ (solute diffusion)}$$

Due to the uncertainties when calculating the thermal stress contribution and that this contribution is only a small fraction of the total stress, it is justified to put $e_t = 1$.

| T | : | Temperature in Kelvin |
| $\dot{\gamma}$ | : | Resolved strain rate |

The contribution due to non-deformable particles is:

$$\tau_p = \left(\frac{AGb}{1.24 \cdot 2\pi}\right)\frac{\ln(\lambda/b)}{\lambda}.$$

Here

$$\lambda = 0.8\left(\sqrt{\pi/f_r} - 2\right)r$$

r :   Average radius of particles (dispersoids)

f_r :   Volume fraction of particles (dispersois)

1.4   The evolution of the dislocation density in the interior of the cells.

$$\frac{d\rho_i}{d\gamma} = \frac{d\rho_i^+}{d\gamma} + \frac{d\rho_i^-}{d\gamma}$$

$$\frac{d\rho_i^+}{d\gamma} = \frac{1}{\left(1 + f(q_b^2 - 1)\right)} \frac{2}{bL_{eff}}$$

$$\frac{d\rho_i^-}{d\gamma} = -\rho_i v \frac{1}{\dot{\gamma}}$$

$$v = \begin{cases} v_g^{(s)} & \text{solute glide} \\ v_c^{(pm)} & \text{pure metal} \\ v_c^{(s)} & \text{solute climb} \end{cases}$$

Where the frequency-terms are defined as follows:

$$v_c^{(pm)} = \xi_\rho^{(pm)} \mathrm{v}_c^{(pm)} \sqrt{\rho_i} \, , \qquad v_g^{(s)} = \xi_\rho^{(sg)} \mathrm{v}_g^{(s)} \sqrt{\rho_i} \, , \quad v_c^{(s)} = \xi_\rho^{(sc)} \mathrm{v}_c^{(s)} \sqrt{\rho_i}$$

The velocity terms are given by:

$$\mathrm{v}_c^{(pm)} = \sqrt{\rho_i} b^2 B_\rho^{(pm)} v_D \exp\left(-\frac{U_{SD}}{kT}\right) 2\sinh\left(\frac{V_\rho^{(pm)} Gb\sqrt{\rho_i}}{kT}\right), \quad V_\rho^{(pm)} = 2\xi_\rho^{(pm)} b^3$$

$$\mathrm{v}_g^{(s)} = l_{a\rho}^{(sg)} B_\rho^{(sg)} v_D \exp\left(-\frac{U_s + \Delta U_s}{kT}\right) 2\sinh\left(\frac{V_\rho^{(sg)} Gb\sqrt{\rho_i}}{2\pi kT}\right),$$

$$l_{a\rho}^{(sg)} = \frac{b}{\omega_s c_{sc}^{1-e_\rho}}, \ V_\rho^{(sg)} = l_s b^2 = \xi_\rho^{(sg)} \omega_s b^3 c_{sc}^{-e_\rho}.$$

$$\mathrm{v}_c^{(s)} = \sqrt{\rho_i} b l_{a\rho}^{(sc)} B_\rho^{(sc)} v_D \exp\left(-\frac{U_s + \Delta U_s}{kT}\right) 2\sinh\left(\frac{V_\rho^{(sc)} Gb\sqrt{\rho_i}}{kT}\right),$$

$$l_{a\rho}^{(sc)} = bc_{sc}^{-1}, \ V_\rho^{(sc)} = 2\xi_\rho^{(sc)} b^3.$$

Here

$$\left(\frac{1}{L_{eff}}\right)^2 = \left(\frac{1}{L_\rho}\right)^2 + \left(\frac{1}{L_p}\right)^2 + \left(\frac{1}{L_D}\right)^2,$$

$$L_\rho = \frac{C}{\sqrt{\rho}}, \ L_p = \frac{r/2f_r}{\kappa_3}, \ L_D = \frac{D}{\kappa_2}.$$

1.5   The misorientation (fictive in stage II).

$$\frac{d\varphi}{d\gamma} = \left(f_{II} \frac{bK_{II}}{\varphi L_{eff}} + (1 - f_{II})0.02 \right) \left(1 - \left(\frac{\varphi}{\varphi_4} \right)^3 \right)$$

$$f_{II} = 1 - \min\left(1, \left(-2 \frac{d\rho^-}{d\rho^+} \right)^5 \right)$$

$$K_{II} = \frac{q_c^2 f^2 (q_b^2 - 1)^2}{(1 + f(q_b^2 - 1))\kappa_0^2}$$

$$\varphi_{II} = \frac{bq_c f(q_b^2 - 1)}{\kappa_0} \sqrt{\rho_i}$$

$$\varphi_4 = \varphi_{IV} - (\varphi_{IV} - \varphi_{II})\min\left(1, \left(\frac{d\delta^+}{d\delta^-} \right)^6 \right)$$

1.6   The evolution of the subgrain size.

$$\frac{d\delta}{d\gamma} = \frac{d\delta^-}{d\gamma} + \frac{d\delta^+}{d\gamma}$$

$$\frac{d\delta^-}{d\gamma} = -\frac{2\delta^2 \rho_i}{\kappa_0 \varphi} \frac{SL_\rho^2}{L_{eff}}$$

$$\frac{d\delta^+}{d\gamma} = \begin{cases} v\frac{1}{\dot{\&}} & \text{if } \delta < \delta_{IV} \\ \min\left(v\frac{1}{\dot{\&}}, -\left(\frac{\delta_{IV}}{\delta} \right)^{13} \frac{d\delta^-}{d\gamma} \right) & \text{if } \delta \geq \delta_{IV} \end{cases}$$

The storage parameter S changes during stage III. A linear scaling with the misorientation is assumed.

$$S = \begin{cases} S_{II} & \varphi \leq \varphi_{II} \\ S_{II} + \dfrac{(\varphi - \varphi_{II})(S_{IV} - S_{II})}{\varphi_{IV} - \varphi_{II}} & \varphi_{II} < \varphi < \varphi_{IV} \\ S_{IV} & \varphi \geq \varphi_{IV} \end{cases},$$

$$S_{II} = \frac{f(q_b^2 - 1)}{2C^2}, \quad S_{IV} = q_{IV} S_{SC}, \quad S_{SC} = \frac{fq_b^2}{2C^2(1 - f)}$$

Recovery at large temperature may not exceed a maximum strength limited by that the that a maximum subgrain size is reached that is given by a high temperature scaling relation:

$$\delta_{IV} = \frac{q_c^{IV}}{\sqrt{\rho_i}}$$

Dipole collapses are given by

$$v = \begin{cases} v_\delta^{(pm)} & \text{pure metal} \\ v_\delta^{(s)} & \text{solute} \end{cases}$$

The velocity terms are given by:

$$v_\delta^{(pm)} = 2B_\delta^{(pm)} b \, v_D \exp\left(-\frac{U_{SD}}{kT}\right) \sinh\left(\frac{pV_\delta^{(pm)}}{kT}\right), \qquad V_\delta^{(pm)} = \xi_\delta^{(pm)} b^3$$

$$v_\delta^{(s)} = 2B_\delta^{(s)} b \, v_D \exp\left(-\frac{U_s + \Delta U_s}{kT}\right) \sinh\left(\frac{pV_\delta^{(s)}}{kT}\right), \qquad V_\delta^{(s)} = \xi_\delta^{(s)} b^3 c_{sc}^{-e_\delta}$$

Here

$$p = 4\gamma_{sd} \Big/ \delta, \qquad \gamma_{sd} = \frac{Gb\varphi}{4\pi(1-\nu)} \ln\left(\frac{e\varphi_c}{\varphi}\right).$$

1.7 Parameters.

$B_\delta^{(pm)}, B_\delta^{(s)}$	:	Constants
$\xi_\delta^{(pm)}, \xi_\delta^{(s)}$	:	Constant
φ_c	:	Constant
ν	:	Poisson ratio
e_δ	:	Constant of order 0.5-1
$q_{IV} = S_{IV}/S_{SC}$	:	Constant of order 0.5-1*S_{SC}
q_c^{IV}	:	High temperature scaling parameter.
b	:	Length of Burgers vector
f	:	The volume fraction of cell walls stage II
q_b	:	Scaling parameter in stage 2
κ_0	:	Constant (area/surface of subgrains approximately equal to 3)
φ_{IV}	:	Saturation misorientation
C	:	Proportionality constant (slip length)
$\kappa_?$	:	Geometrical shape factor for the grains
κ_3	:	Geometrical shape factor for the particles
q_c	:	Scaling factor stage II
ω_s	:	Constant
$\xi_\rho^{(pm)}, \xi_\rho^{(sg)}, \xi_\rho^{(sc)}$	:	Constants
$B_\rho^{(pm)}, B_\rho^{(sg)}, B_\rho^{(sc)}$	:	Constants
A	:	Constant of order unity

k	:	Boltzmann's constant
v_D	:	The Debye frequency in s^{-1}
ω_ρ, ω_t	:	Constants of order unity (to be determined experimentally
$B_t^{(s)}, B_t^{(pm)}$	:	Constants, to be determined experimentally
B_{sc}, n	:	DSA constants
ΔU_{sd}		
c	:	Concentration. Alloy element in atom percent.
m	:	Mobile stored dislocation density scaling constant.
e_t	:	Constant put equal to 1
U_{SD}, U_s	:	Activation energy for self diffusion and diffusion of atoms in solution
ΔU_s	:	Binding energy between atoms and dislocations
α_1	:	Constant ≈ 0.3
α_2	:	Constant ≈ 2
G	:	Shear modulus

C Matlab Functions

C.1 Generating Growth Texture

```matlab
function odf_growth = GrowthTextureODF(ori_deformed_10000)

% Make the 40<111> rotation of the deformation grains
% ori_deformed_10000; - the input orientationlist containing the sampled
% deformation orientations
input_defori = ori_deformed_10000;
ss = ori_deformed_10000.SS;
cs = crystalSymmetry('432');

h = Miller(1,1,1,cs);

ori_rot = orientation('axis',symmetrise(h),'angle',40*degree, cs);

growth_ori = input_defori*ori_rot;

% Texture calculations
growth_ori.SS = ss;
odf_growth = calcODF(growth_ori, 'halfwidth', 5*degree, 'HarmonicDegree', 22,'fourier');
```

Figure C.1: Matlab function for generating growth texture

C.2 Generating PSN

```matlab
function odf_psn = CalPSNtexture(ori_deformed_10000)

% Generate PSN texture
% <112> axis
cs = crystalSymmetry('432');
h = Miller(1,1,2,cs);

% 35%rotation
ori_rot = orientation('axis',symmetrise(h),'angle',35*degree, cs);

% PSN orientations
ori_psn = ori_deformed_10000*ori_rot;

% Calculate the texture
odf_psn = calcODF(ori_psn, 'halfwidth', 5*degree, 'HarmonicDegree', 22,'fourier');
```

Figure C.2: Matlab function for generating PSN

C.3   Loading Cube Nucleation

```matlab
function odf_cube = CalCubetexture(ss)

% Read the ODF values from AUSWERT out, write into OIM compatable
path = '/Users/Christian/OneDrive/Dokumenter/Master - Spring 2015/Matlab/ReX/Data files/';

% *.OUT file name
file_out = [path uigetfile({'*.out;*.ang'},'Load cube texture file',path)];

res = 5*degree;
cs = crystalSymmetry('432');

if strcmp(file_out(end-3:end) ,'.out')
    % ODF data array and blocks
    ODF_DATA = zeros();
    ang_res = 5;
    TOTAL_ROWN = 0;

    % Read the *.out file
    [fid, message] = fopen(file_out,'r+');
    if fid<0
       disp(message);
    end
    % Read the top 4 rows for the head
    str = fgetl(fid);
    str = fgetl(fid);
    str = fgetl(fid);
    str = fgetl(fid);

    % Read the PHI2 section blocks, there should be 19 blocks
    for i_phi2_sec = 1:19
    %    first read the top 4 rows for header
    str = fgetl(fid);
    str = fgetl(fid);
    str = fgetl(fid);
    str = fgetl(fid);
    % read data
        for j_phi = 1: 19
            str = fgetl(fid);
            data_row = str2num(str);

            % read data for each Phi1
            for k_phi1 = 1:19
                TOTAL_ROWN = TOTAL_ROWN+1;
                ODF_DATA(TOTAL_ROWN,1) = (k_phi1-1)*ang_res;
                ODF_DATA(TOTAL_ROWN,2) = (j_phi-1)*ang_res;
                ODF_DATA(TOTAL_ROWN,3) = (i_phi2_sec-1)*ang_res;
                ODF_DATA(TOTAL_ROWN,4) = data_row(k_phi1+1);
                if ODF_DATA(TOTAL_ROWN,4)<0
                   ODF_DATA(TOTAL_ROWN,4) = 0.0001;
                end
            end
        end
    end
    fclose(fid);
```

```matlab
    % Write into temp file and read the ODF using MTEX functions
    file_tempodf = [path '/temp.odf'];
    fid = fopen(file_tempodf,'w');
    fprintf(fid,'%3.5f %3.5f %3.5f %3.5f\n',ODF_DATA');
    fclose(fid);

    odf_cube = loadODF(file_tempodf,cs,ss,'resolution',res,'Bunge',...
       'ColumnNames',{'Euler 1','Euler 2','Euler 3','weights'},...
       'Columns',[1,2,3,4]);

elseif strcmp(file_out(end-3:end) ,'.ang')

    cs = {'notIndexed',crystalSymmetry('432', [4.04 4.04 4.04], 'mineral', 'Aluminum', 'col
or', 'light blue')};
    cube_EBSD = loadEBSD(file_out,cs,'interface','ang',...
        'convertEuler2SpatialReferenceFrame');
    rot = rotation('Euler',-90*degree,0*degree,0*degree);
    cube_EBSD = rotate(cube_EBSD,rot);
    cube_EBSD = cube_EBSD('Al').orientations;
    cube_EBSD.SS = ss;
    odf_cube = calcODF(cube_EBSD, 'halfwidth', res, 'HarmonicDegree', 22,'fourier');

end
```

Figure C.3: Matlab function for loading cube nucleation file

C.4   Generating Grain Boundary Nucleation

```matlab
function odf_gb = CalGBtexture(myodf)

% generate random orientations
cs = crystalSymmetry('432');
ss = myodf.SS;
odf = uniformODF(cs,ss);
ori_rand_10k = calcOrientations(odf,10000);

rand_odf = calcODF(ori_rand_10k, 'halfwidth', 5*degree, 'HarmonicDegree', 22,'fourier');
def_odf = myodf;

odf_gb = 0.5*1 + 0.5*def_odf;
```

Figure C.4: Matlab function for generating grain boundary nucleation

C.5   Generating Simulated Texture

```matlab
function [rxodfsim, rxpfsim] = rx_run(ori_deformed_10000,cube,PSN,GB,odf_Cube,odf_PSN,odf_GB)
% Create the Growth texture ODF
odf_growth = GrowthTextureODF(ori_deformed_10000);

% Weight the different nucleation mechanisms
odf_nucl = cube*odf_Cube + PSN*odf_PSN + GB*odf_GB;

% Multiply nucleation odf and growth odf
%nucleation odf data
cs = odf_nucl.CS;
ss = odf_nucl.SS;
S3G = regularSO3Grid(cs,ss,'Bunge', 'MTEX');
v_n = eval(odf_nucl,S3G,'Bunge', 'MTEX');
d = Euler(S3G,'Bunge', 'MTEX');
d = mod(d,2*pi);
d = d./degree;

data_nucl = [d, v_n(:)].';

% data for growth odf data
cs = odf_growth.CS;
ss = odf_growth.SS;
S3G = regularSO3Grid(cs,ss,'Bunge', 'MTEX');
v_n = eval(odf_growth,S3G,'Bunge', 'MTEX');
d = Euler(S3G,'Bunge', 'MTEX');
d = mod(d,2*pi);
d = d./degree;
data_growth = [d, v_n(:)].';

data_rx = data_growth;

data_rx(4,:) = data_nucl(4,:).*data_growth(4,:);

%Save rx data in temporary file to be read as ODF
filename = '/Users/Christian/OneDrive/Dokumenter/Master - Spring 2015/Matlab/ReX/Data files/temp.odf';
fid = fopen(filename,'w');
fprintf(fid,'%3.5f %3.5f %3.5f %3.5f\n',data_rx);
fclose(fid);

pname = '/Users/Christian/OneDrive/Dokumenter/Master - Spring 2015/Matlab/ReX/Data files/';
fname = [pname '/temp.odf'];

%ODF
rxodfsim = loadODF(fname,cs,ss,'resolution',5*degree,'Bunge',...
  'ColumnNames',{'Euler 1','Euler 2','Euler 3','weights'},...
   'Columns',[1,2,3,4]);

%Pole figure
ss = 'triclinic';
rxpfsim = loadODF(fname,cs,ss,'resolution',5*degree,'Bunge',...
  'ColumnNames',{'Euler 1','Euler 2','Euler 3','weights'},...
   'Columns',[1,2,3,4]);
```

Figure C.5: Matlab function for generating the simulated texture

C4

D   Texture Plots

D.1   ODF Plots

D.1.1   Deformed After Extrusion
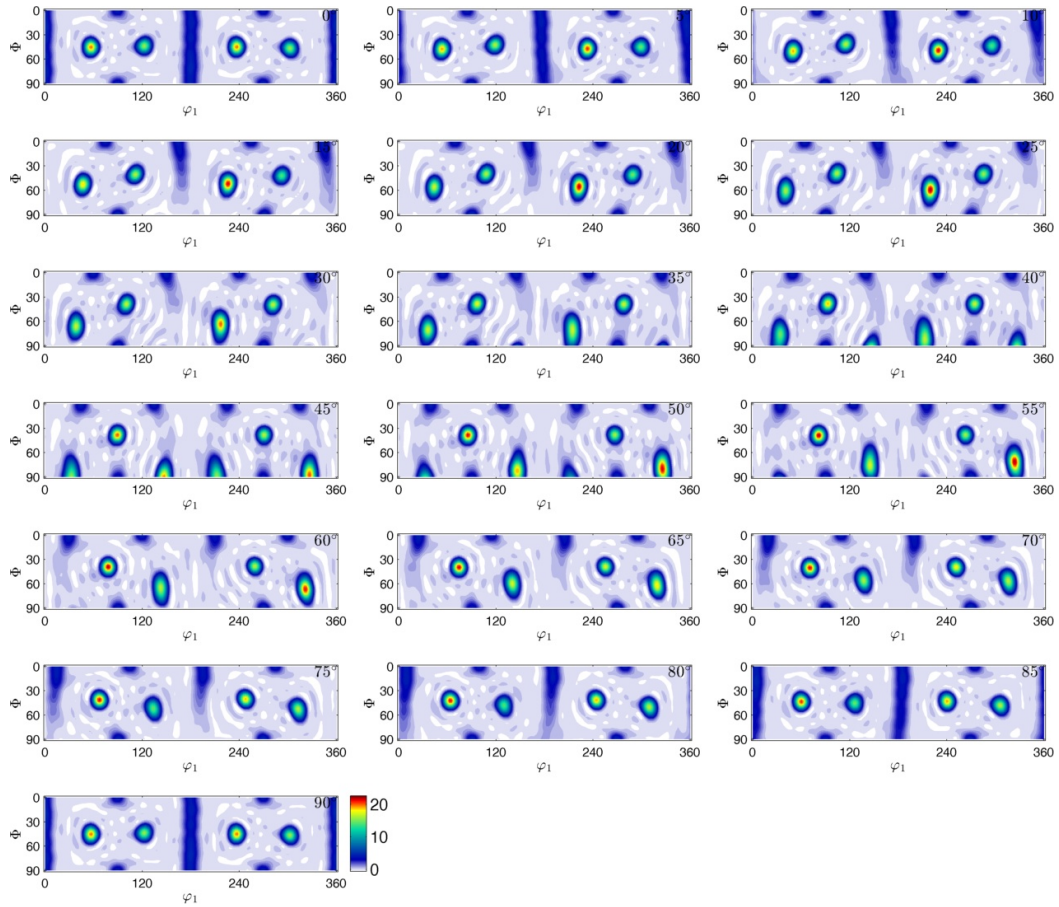
Figure D.1: ODF of deformed D04

D.1.2   Heat Treated Samples
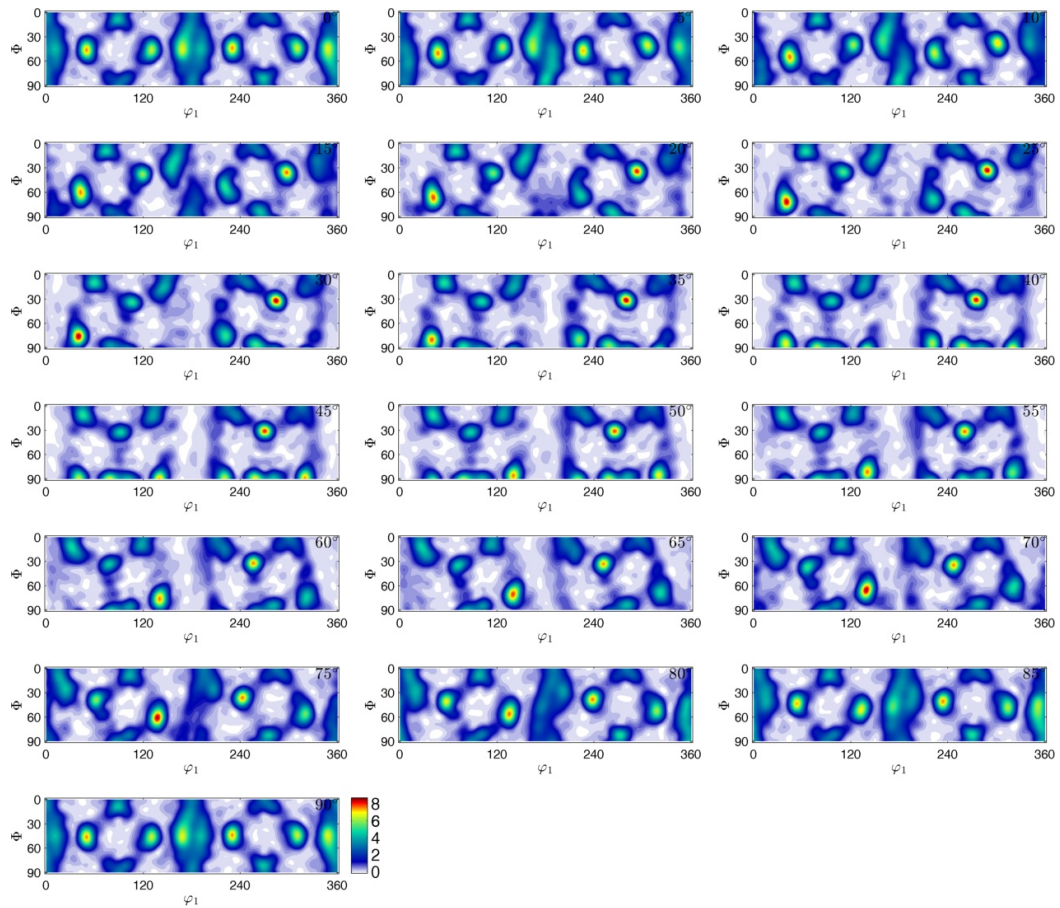
Figure D.2: ODF of heat treated D04 for 10s at 450°C
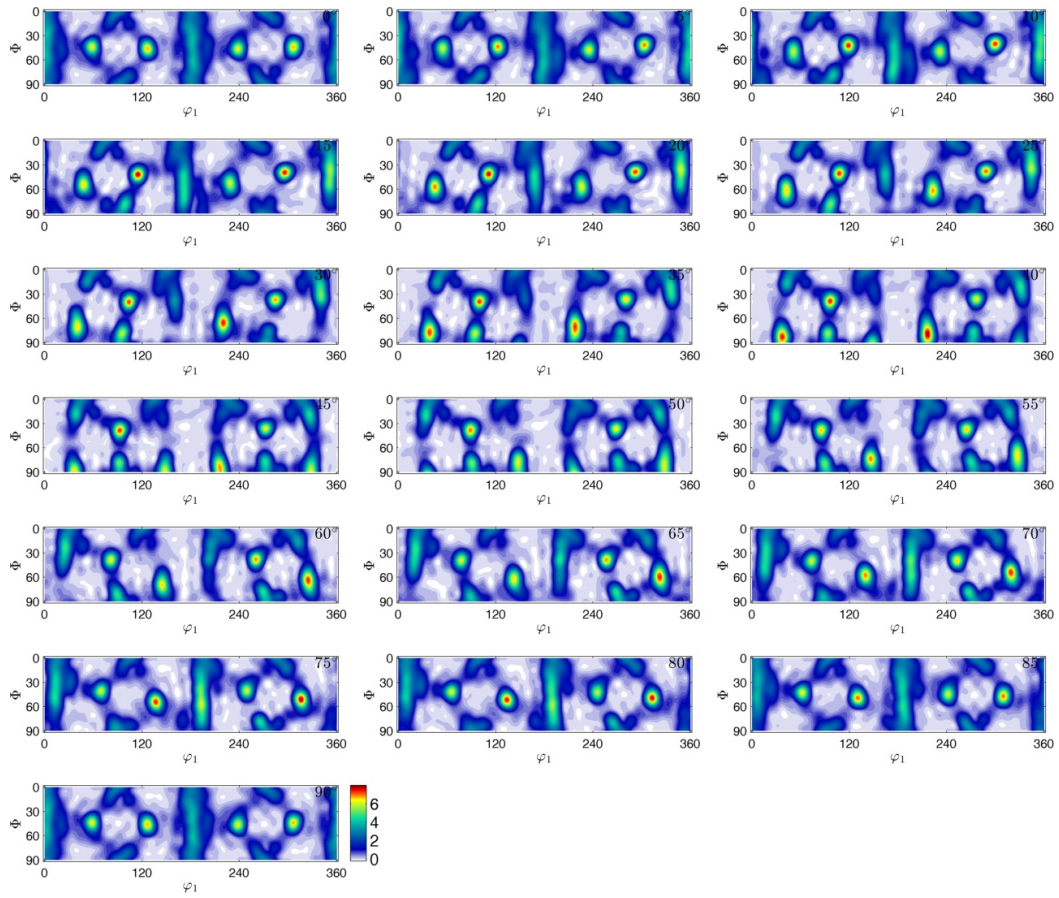
Figure D.3: ODF of heat treated D04 for 120s at 450°C

Figure D.4: ODF of heat treated D04 for 610s at 450°C
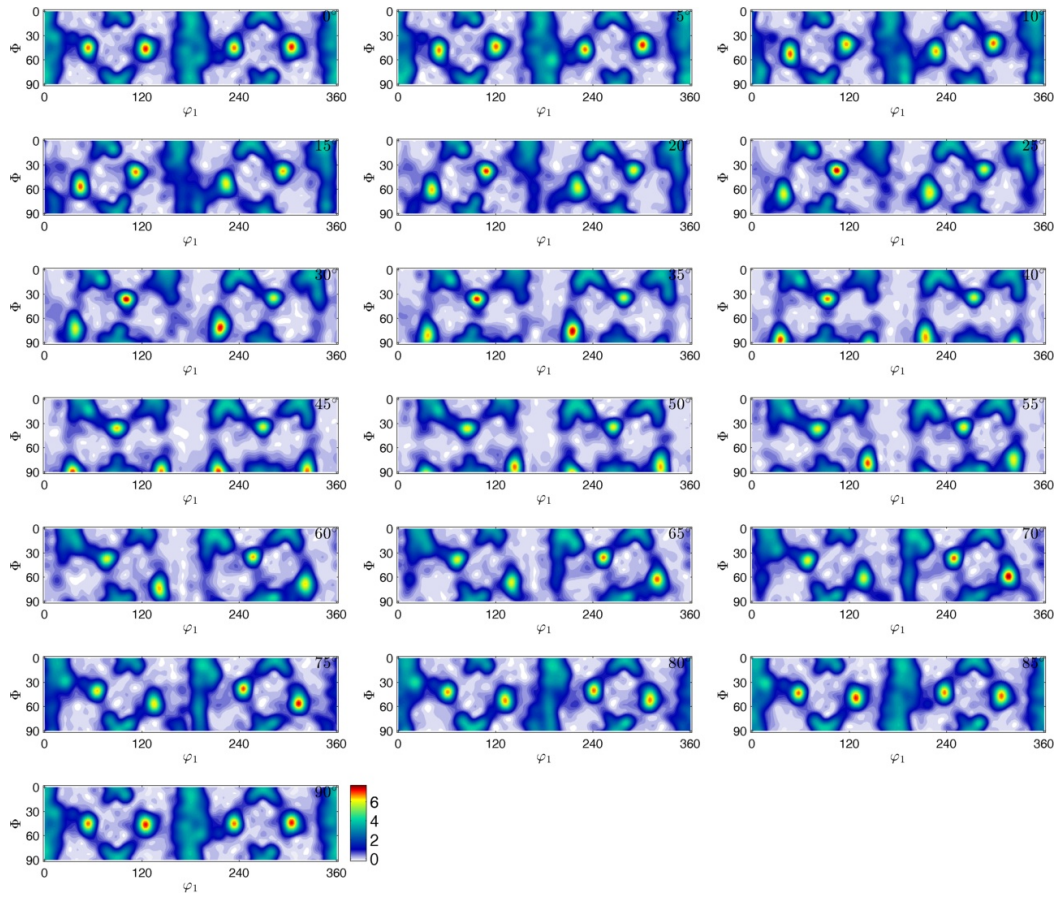
Figure D.5: ODF of heat treated D04 for 10s at 500°C

D.1.3   Spontaneously Recrystallised During Extrusion
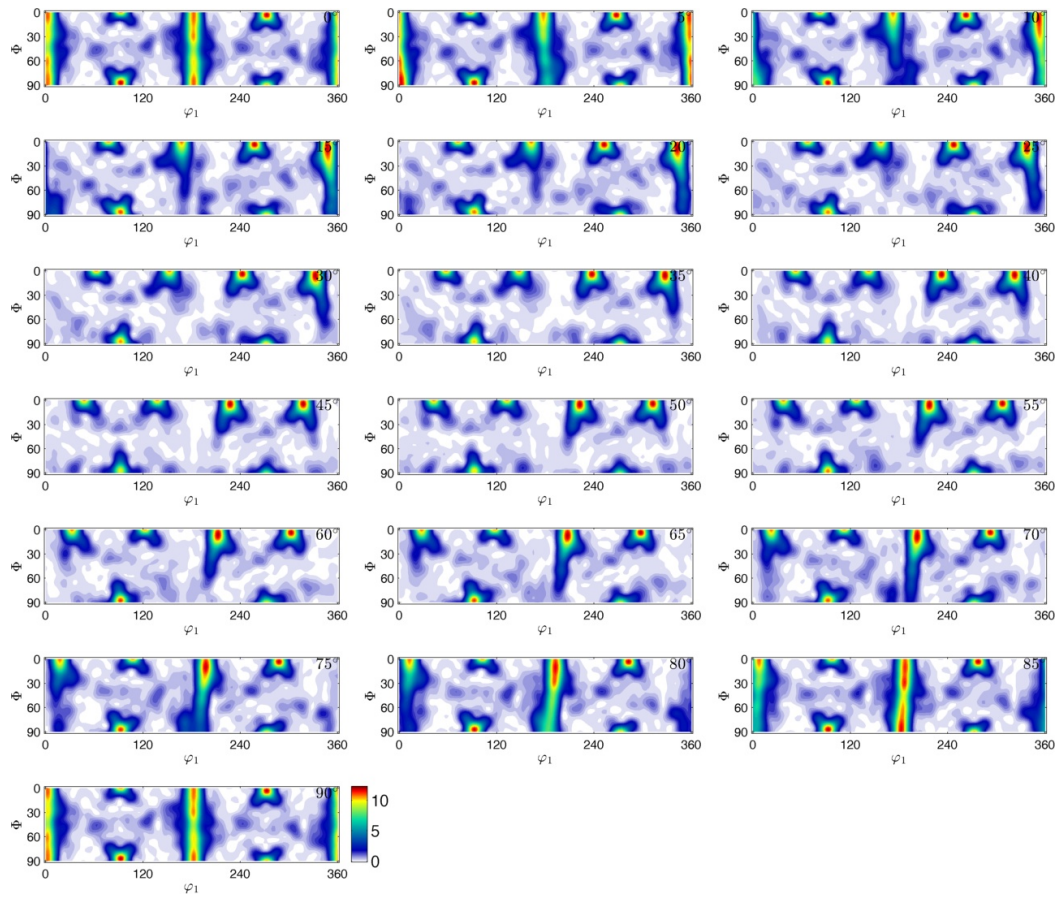
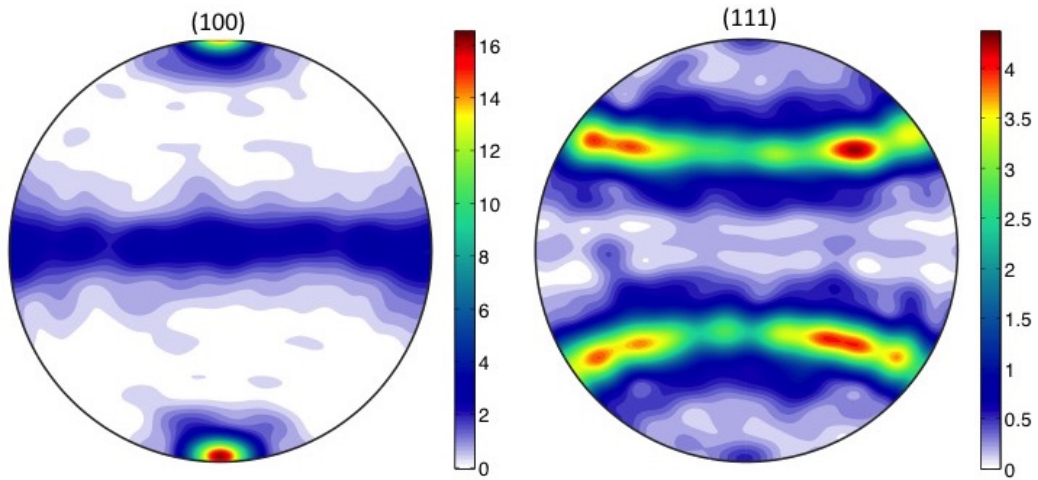**Figure D.6:** ODF of spontaneously recrystallised E6
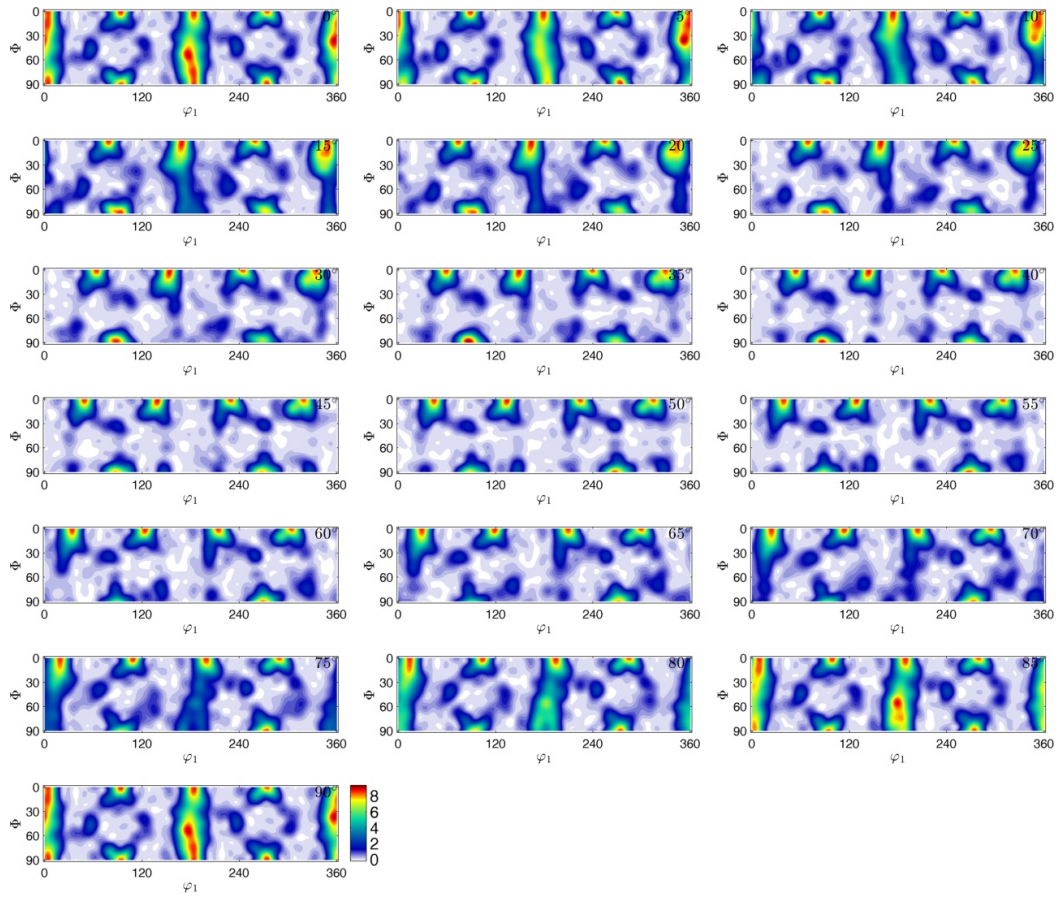
Figure D.7: ODF of spontaneously recrystallised B2, analysed near the tip
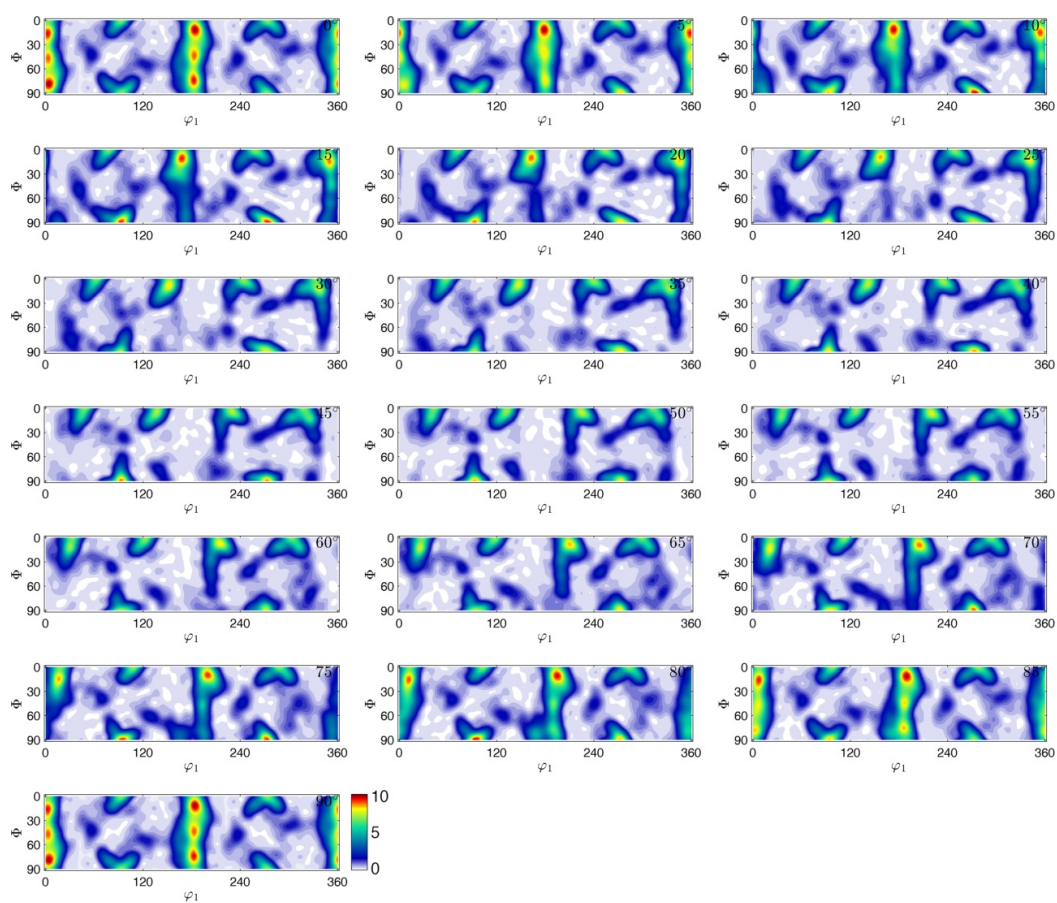
Figure D.8: ODF of spontaneously recrystallised B2, analysed near the die
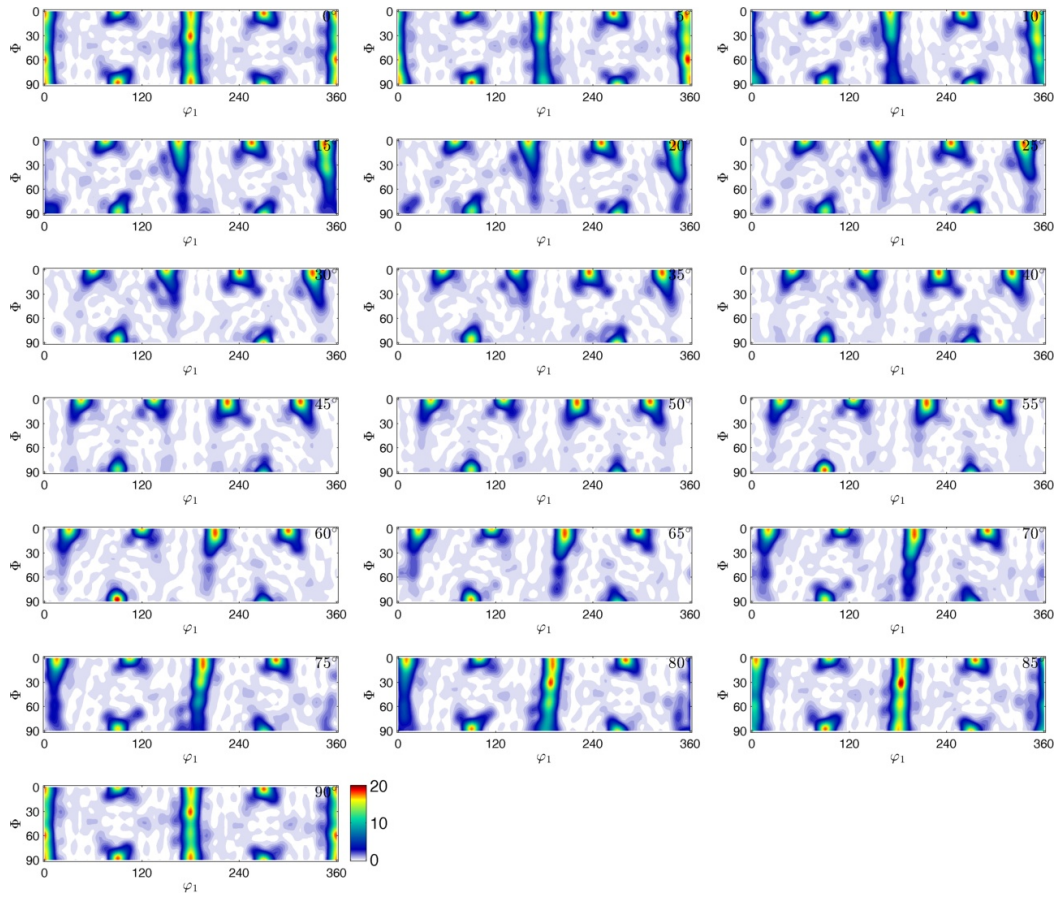
Figure D.9: ODF of spontaneously recrystallised E24

D.1.4   Simulated Recrystallised Texture
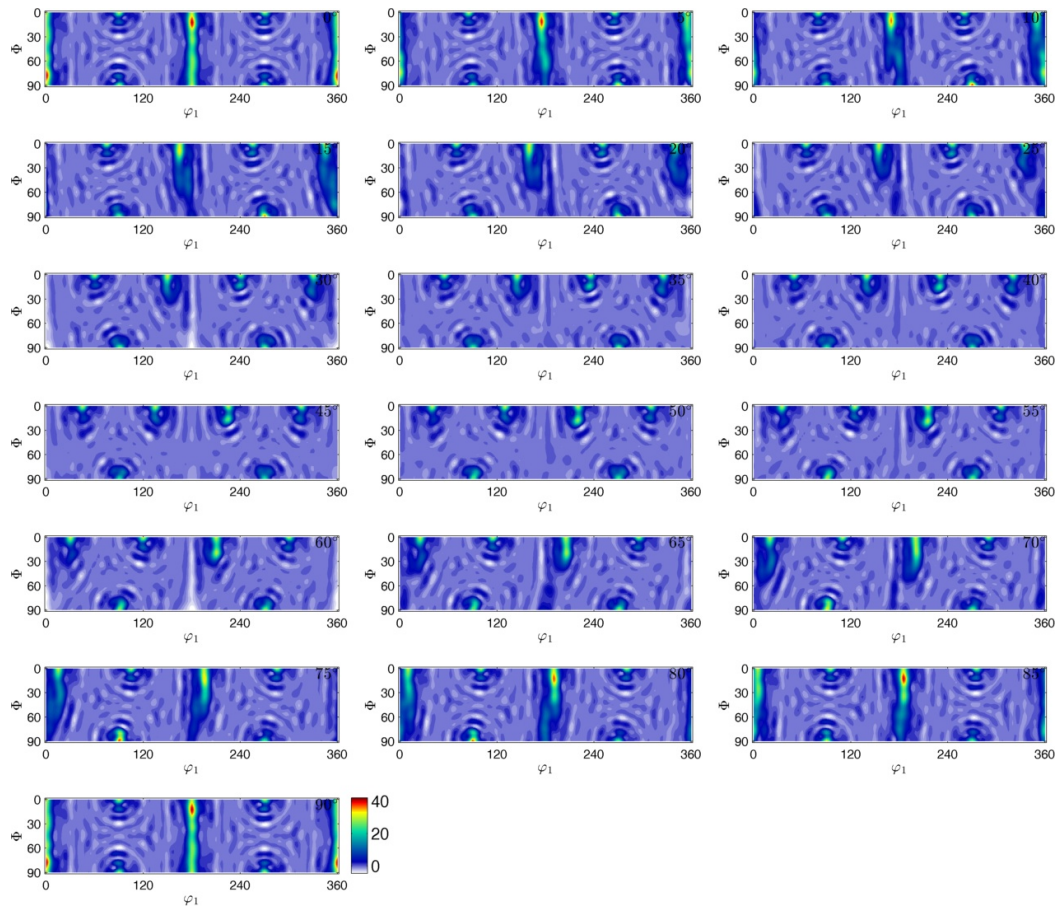
Figure D.10: Simulated ODF with 100% cube nucleation

Figure D.11: Simulated ODF with 100% grain boundary nucleation
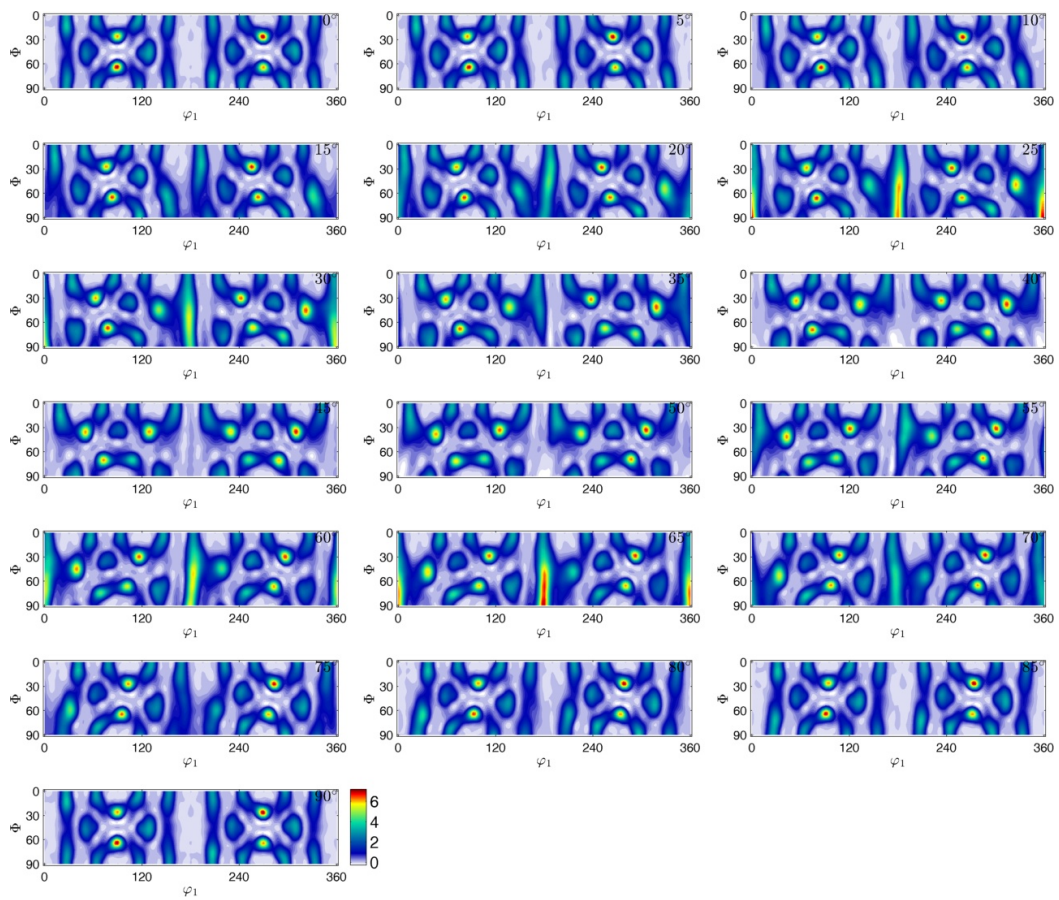
Figure D.12: Simulated ODF with 100% PSN
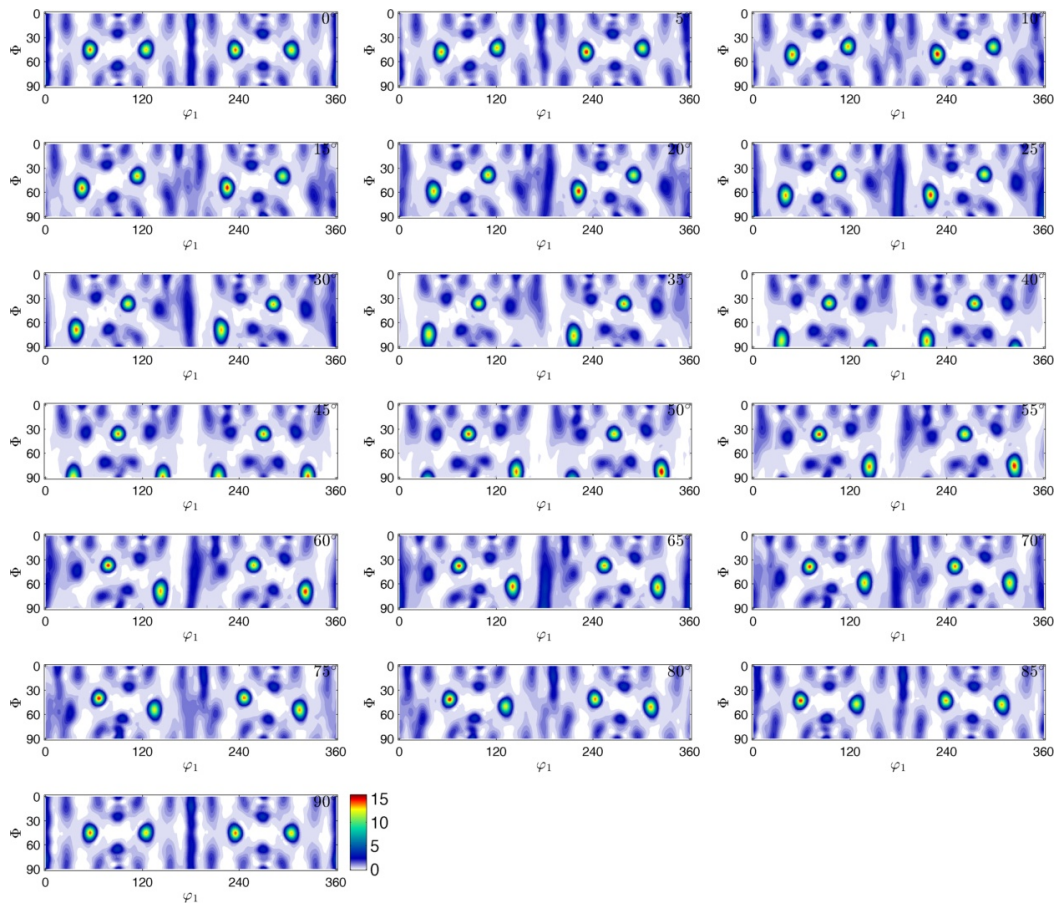
Figure D.13: Simulated ODF with 33% cube, 33% GB and 34% PSN
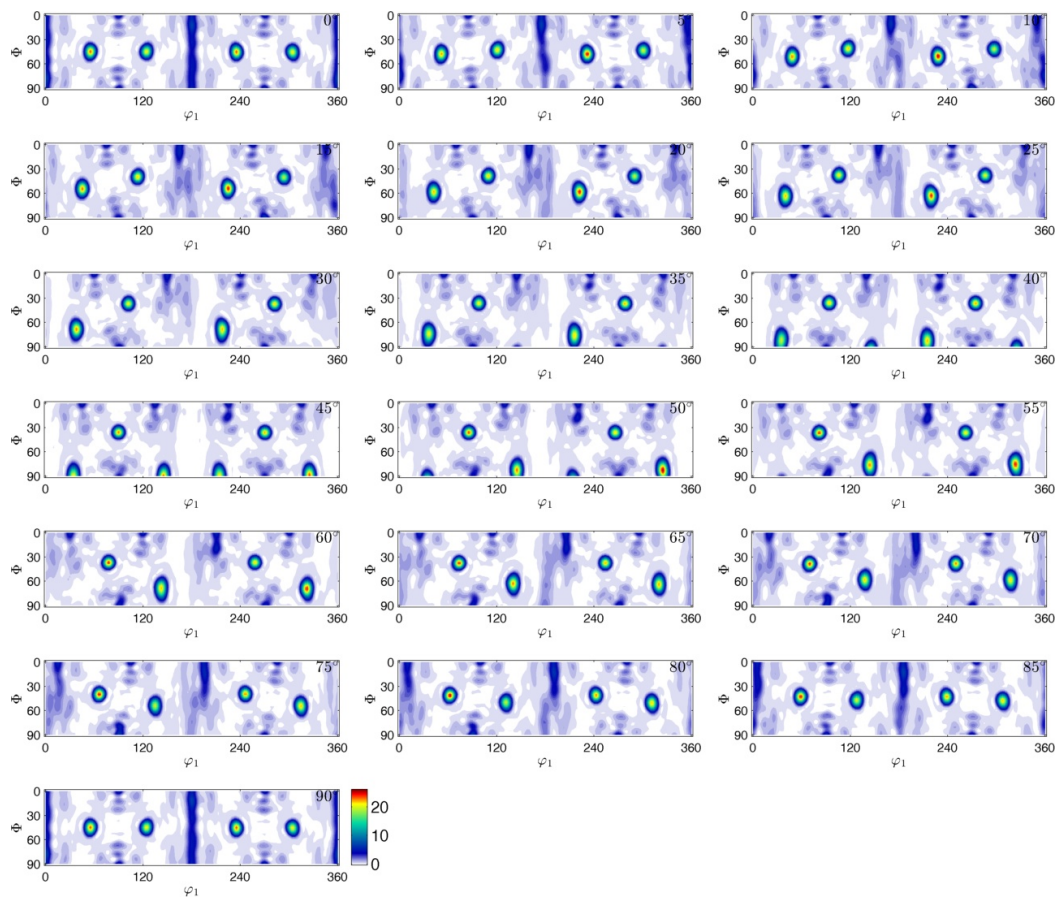
Figure D.14: Simulated ODF with 50% cube and 50% GB nucleation
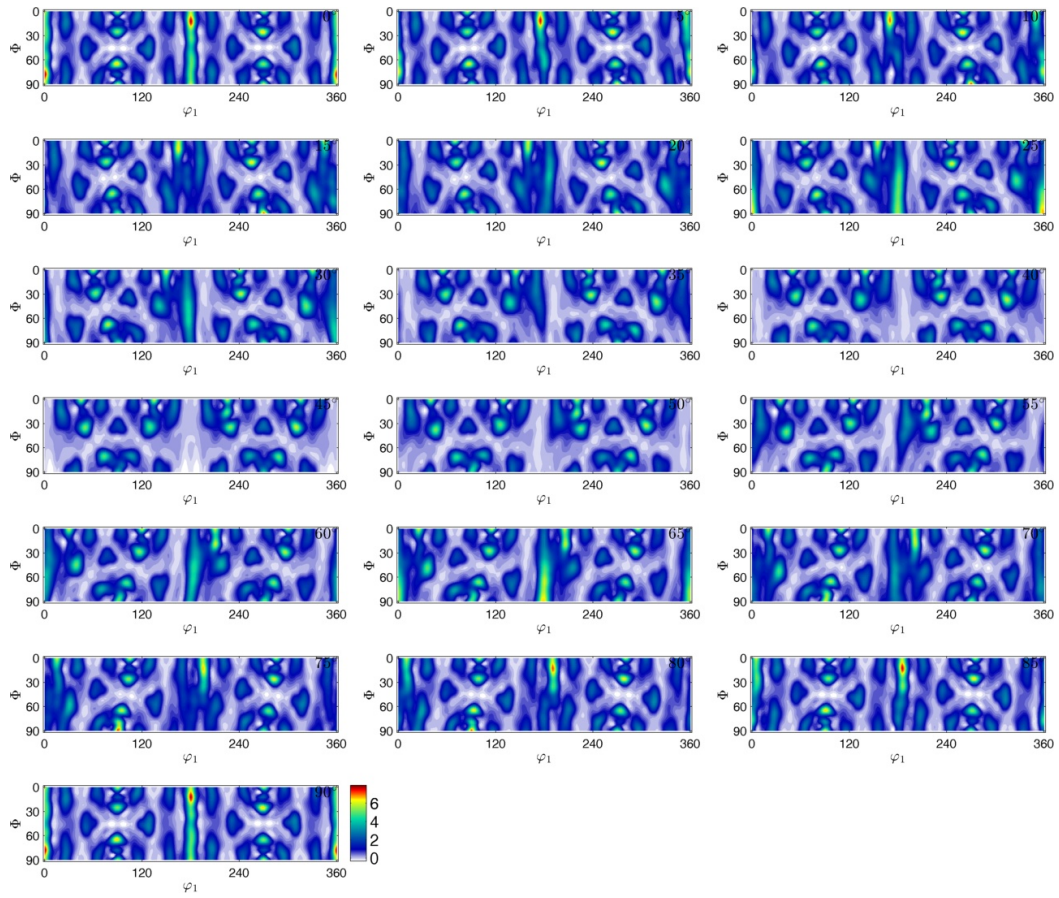
Figure D.15: Simulated ODF with 50% cube and 50% PSN
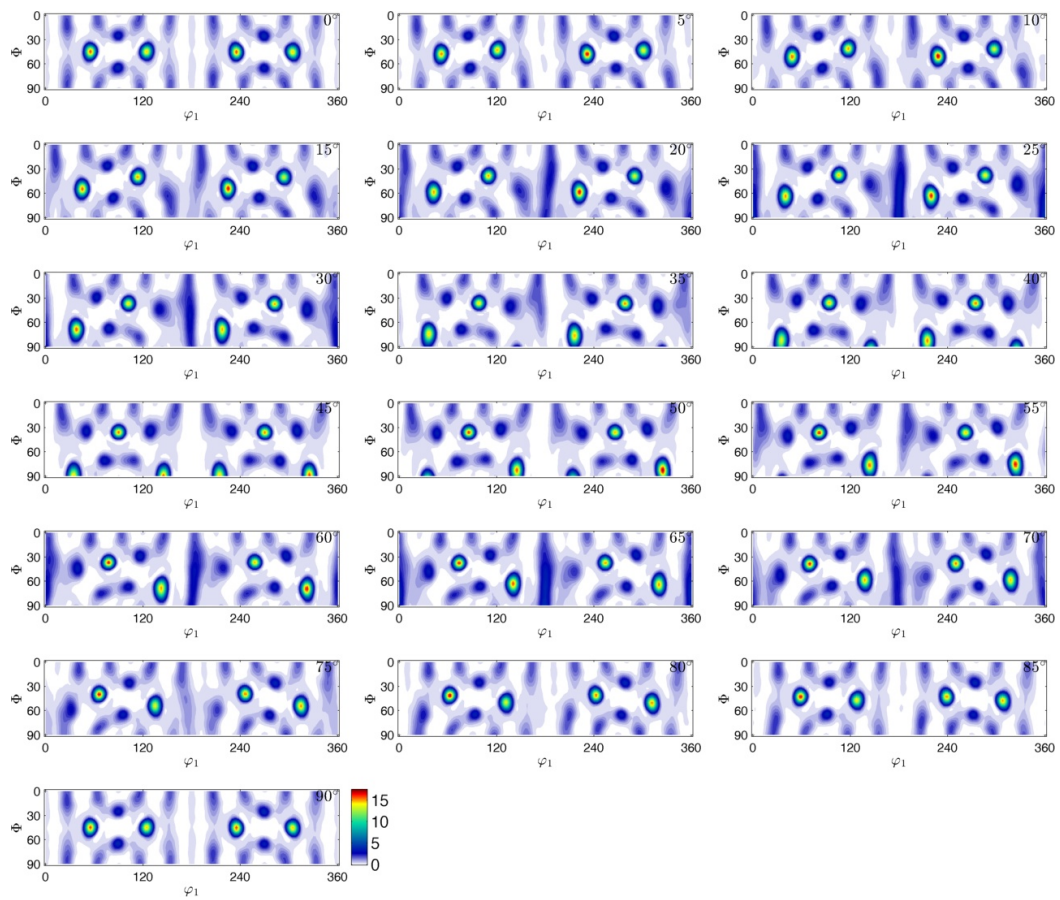
Figure D.16: Simulated ODF with 50% GB and 50% PSN
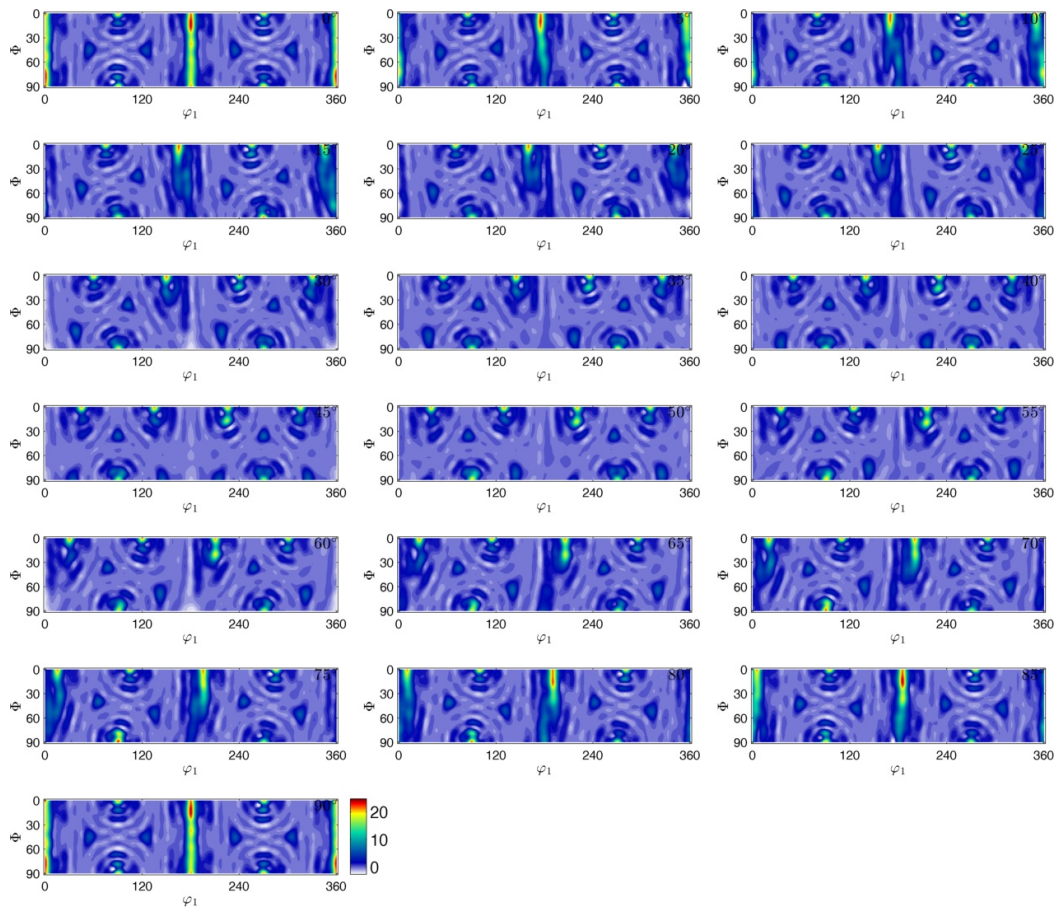
Figure D.17: Simulated ODF with weighting factors giving best fit when comparing with B2 (tip)
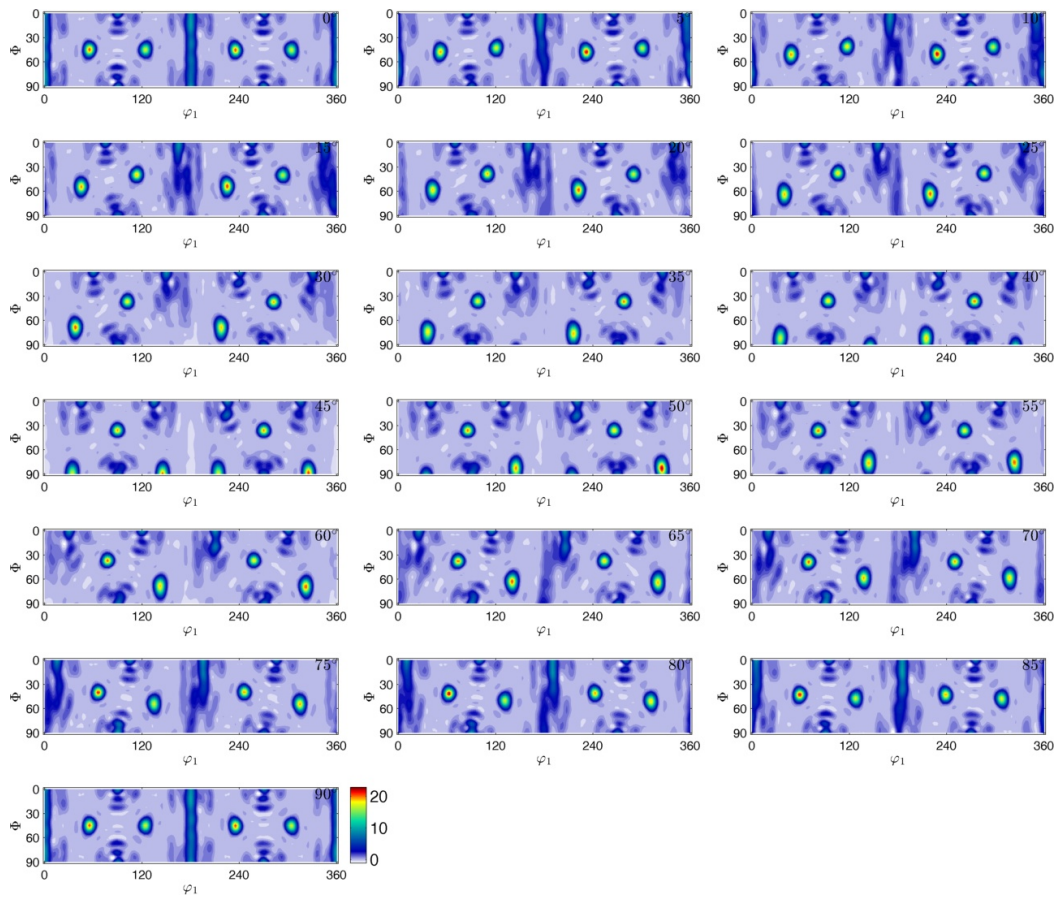
Figure D.18: Simulated ODF with weighting factors giving best fit when comparing with heat treated D04 for 610s at 450°C
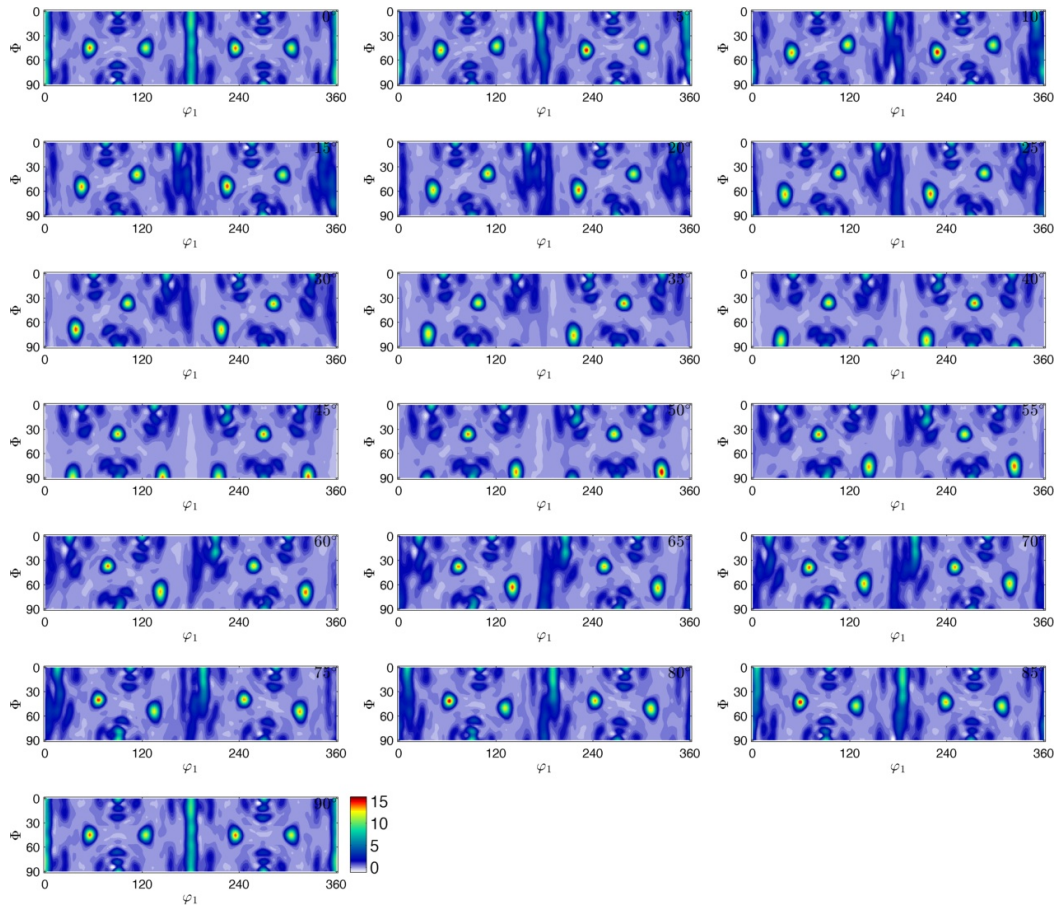
Figure D.19: Simulated ODF with weighting factors giving best fit when comparing with heat treated D04 for 10s at 500°C
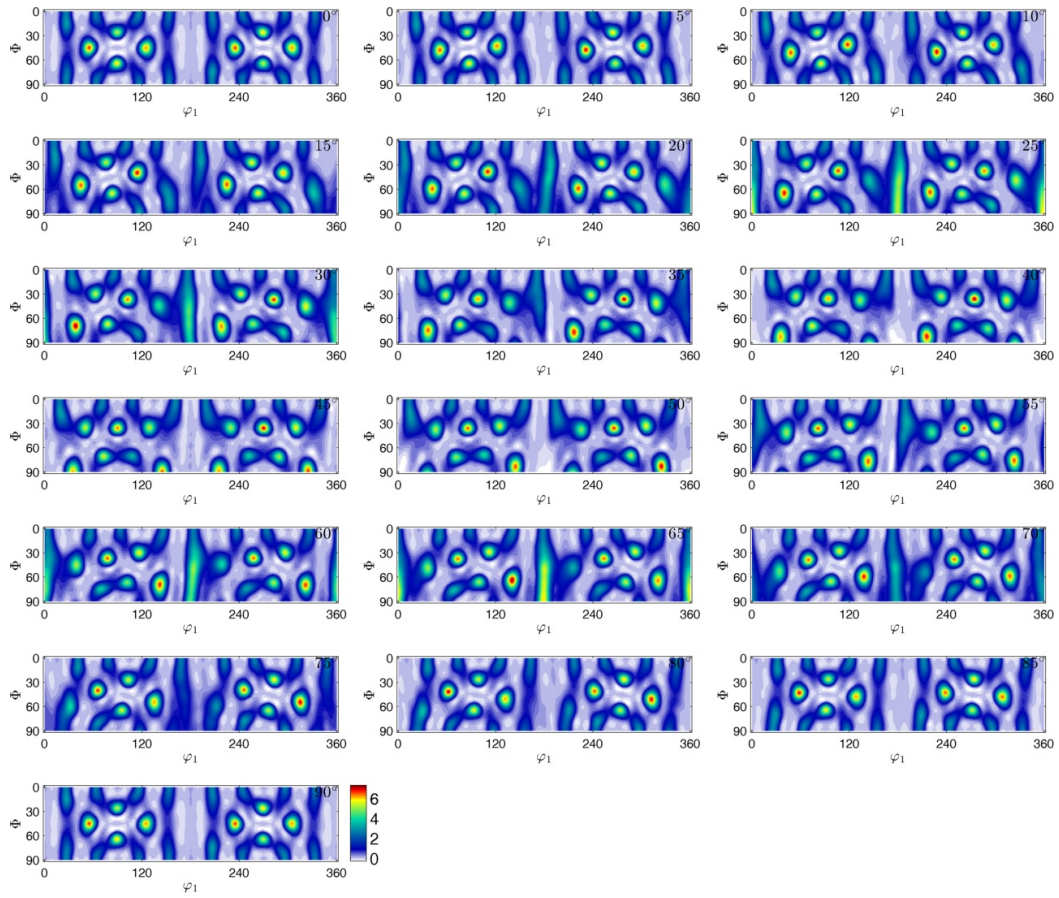
Figure D.20: Simulated ODF with weighting factors for nucleation mechanisms found in *ALSOFT*, by using Equation 2.6, 2.7 and 2.8.

D.2   Pole Figures

D.2.1   Deformed After Extrusion
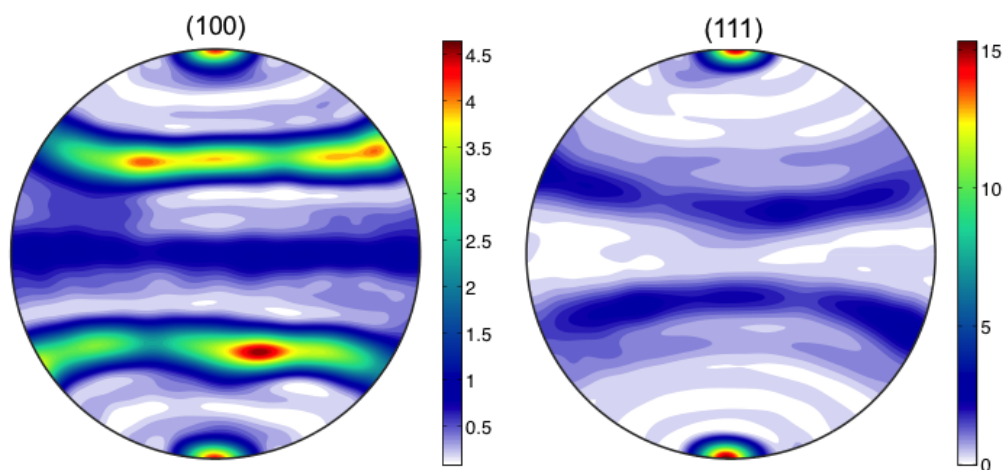
Figure D.21: (100) and (111) pole figures of deformed D04

D.2.2   Heat Treated Samples
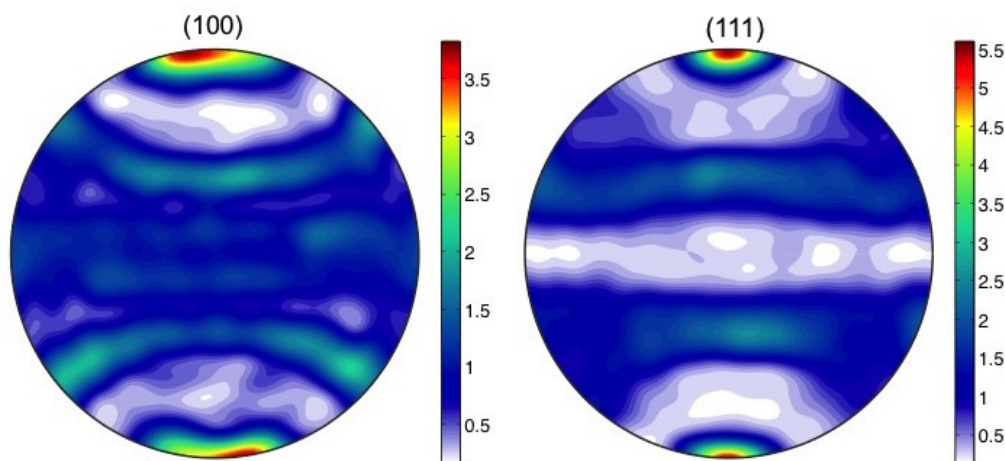
Figure D.22: (100) and (111) pole figures of heat treated D04 for 10s at 450°C
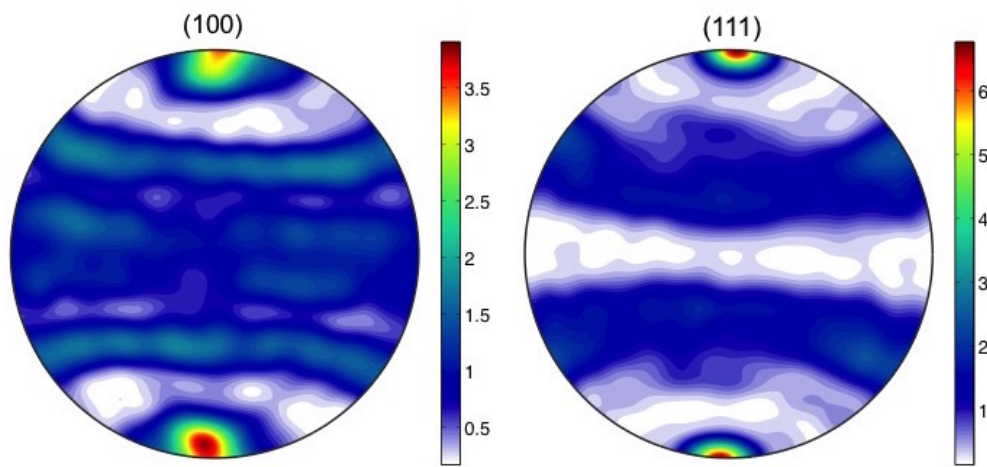
Figure D.23: (100) and (111) pole figures of heat treated D04 for 120s at 450°C
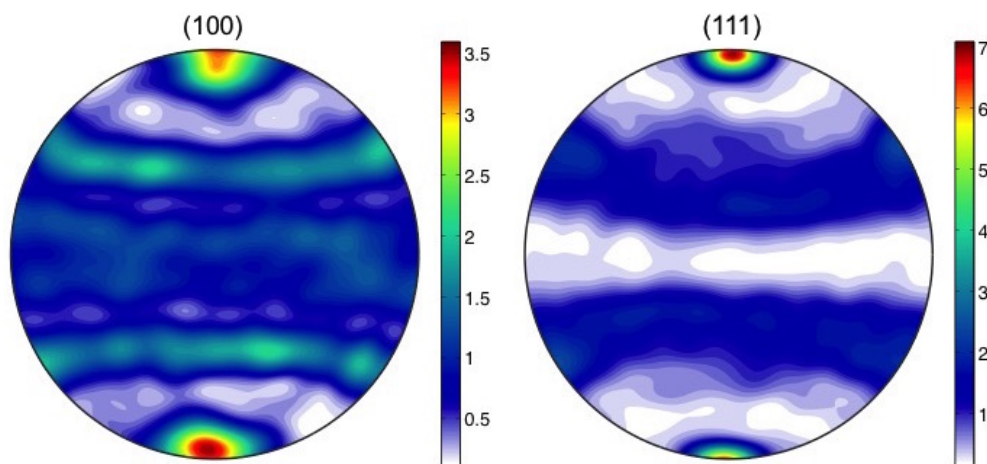
Figure D.24: (100) and (111) pole figures of heat treated D04 for 610s at 450°C
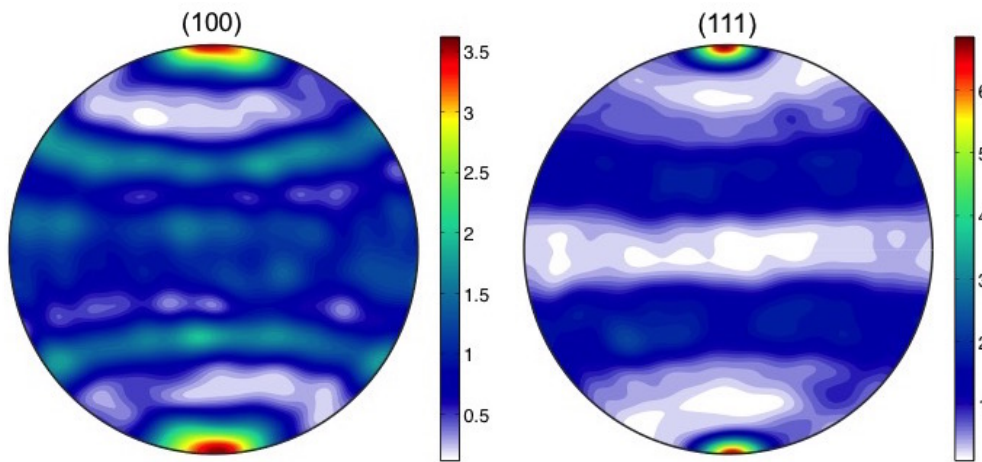
Figure D.25: (100) and (111) pole figures of heat treated D04 for 10s at 500°C

D.2.3   Spontaneously Recrystallised During Extrusion
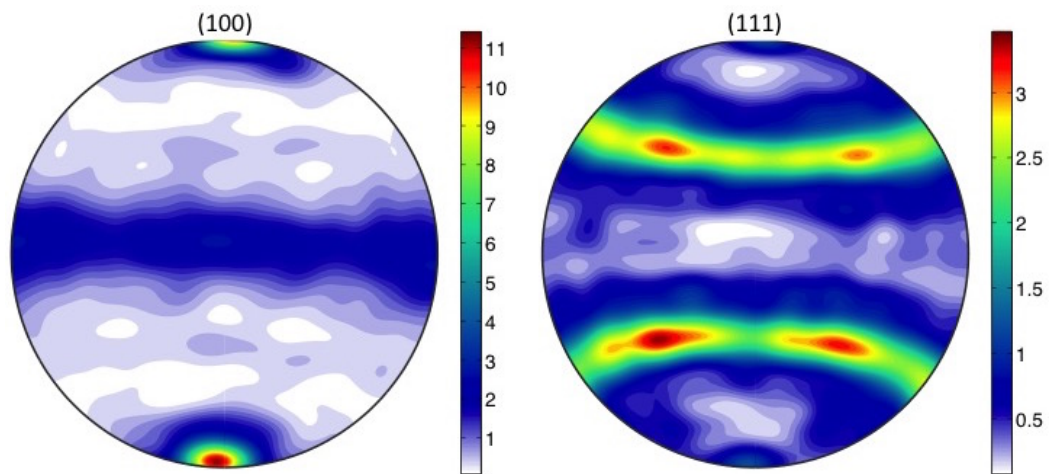
Figure D.26: (100) and (111) pole figures of spontaneously recrystallised E6
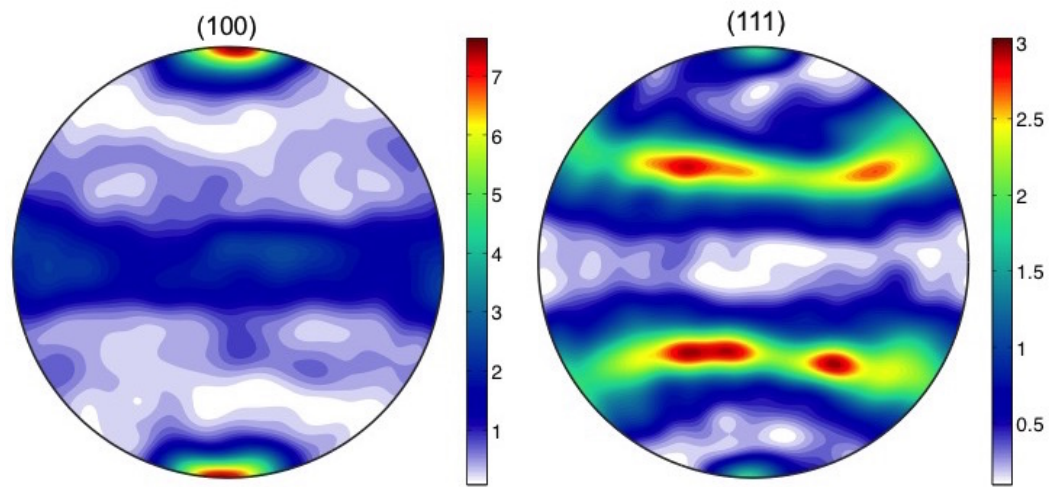
Figure D.27: (100) and (111) pole figures of spontaneously recrystallised B2 (tip)
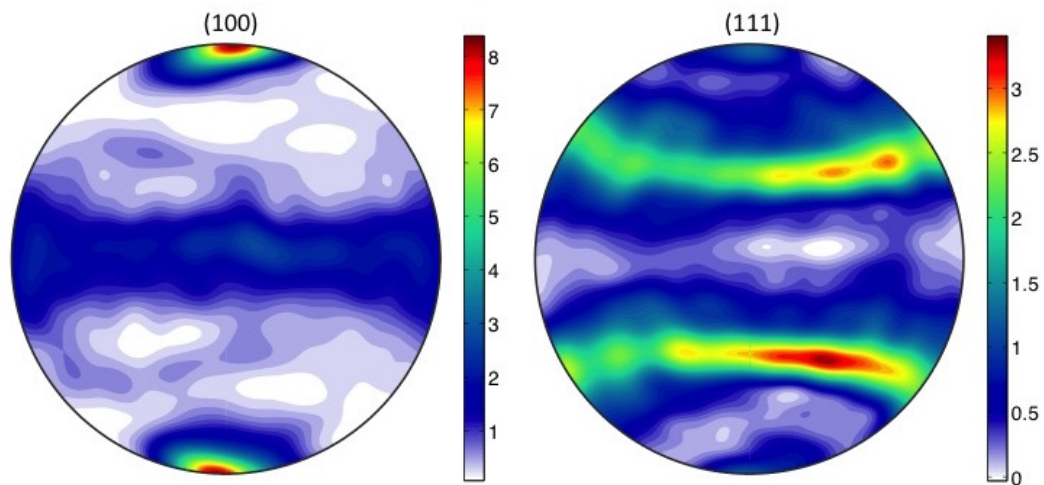
Figure D.28: (100) and (111) pole figures of spontaneously recrystallised B2 (die)

Figure D.29: (100) and (111) pole figures of spontaneously recrystallised E24

D.2.4   Simulated Recrystallised Texture
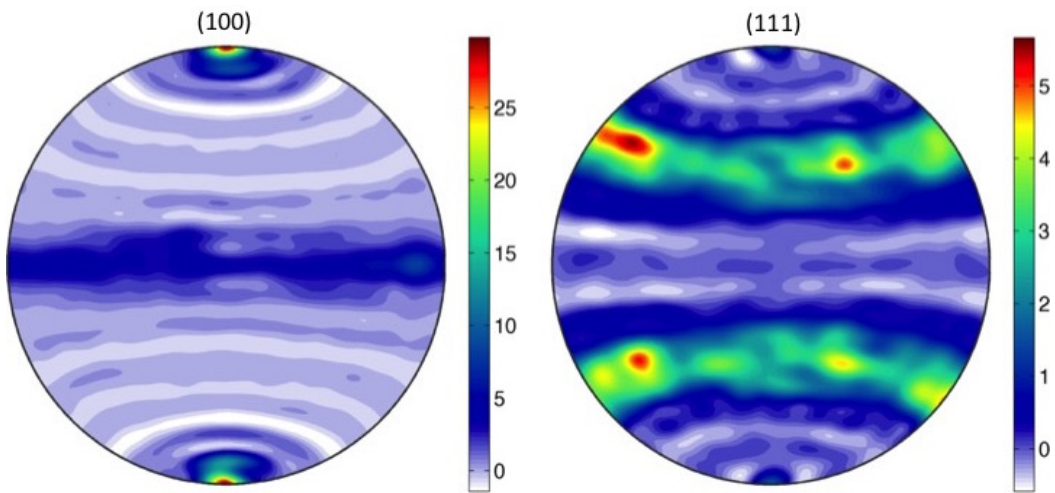
Figure D.30: Simulated (100) and (111) pole figures with 100% cube nucleation
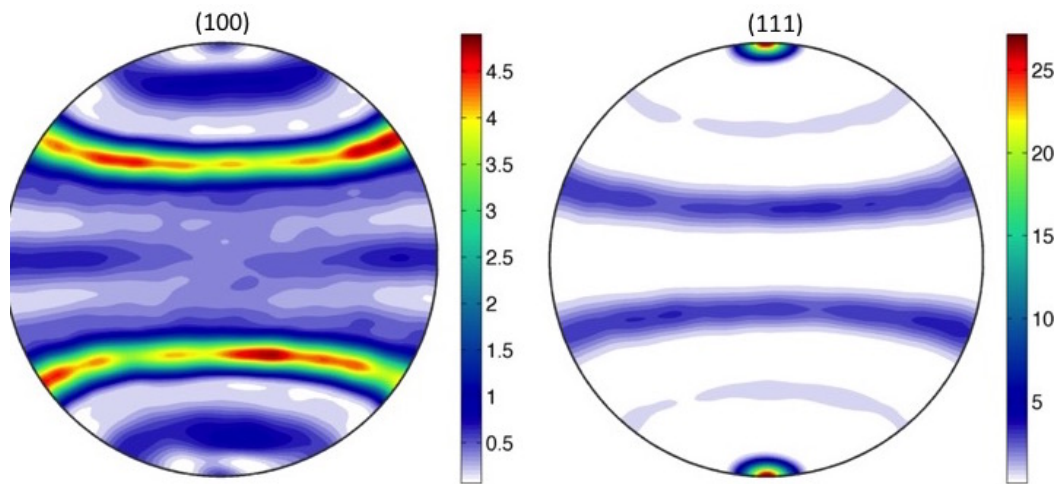
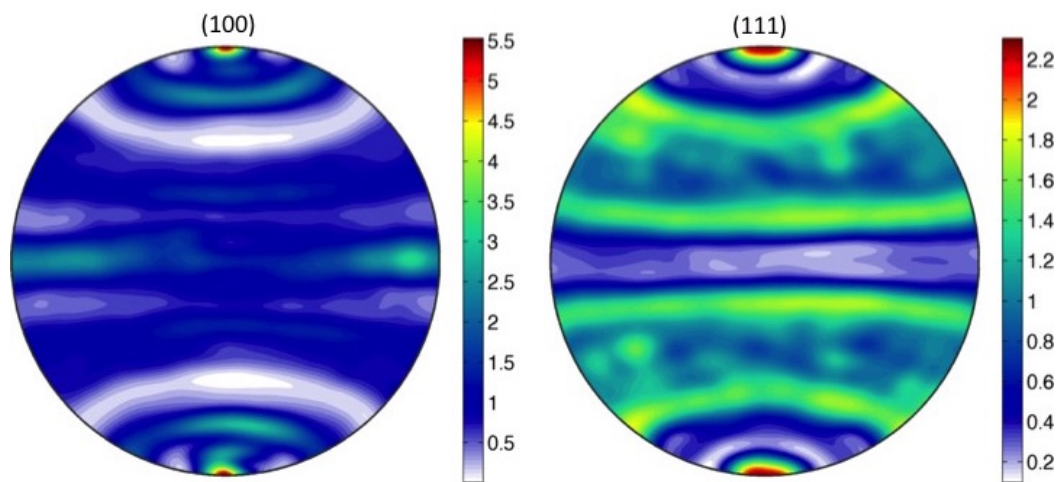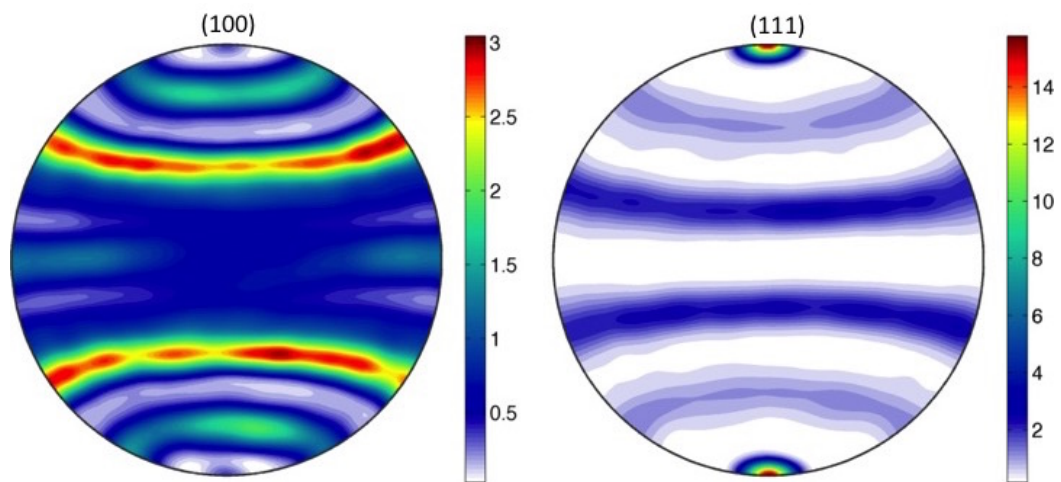**Figure D.31:** Simulated (100) and (111) pole figures with 100% grain boundary nucleation
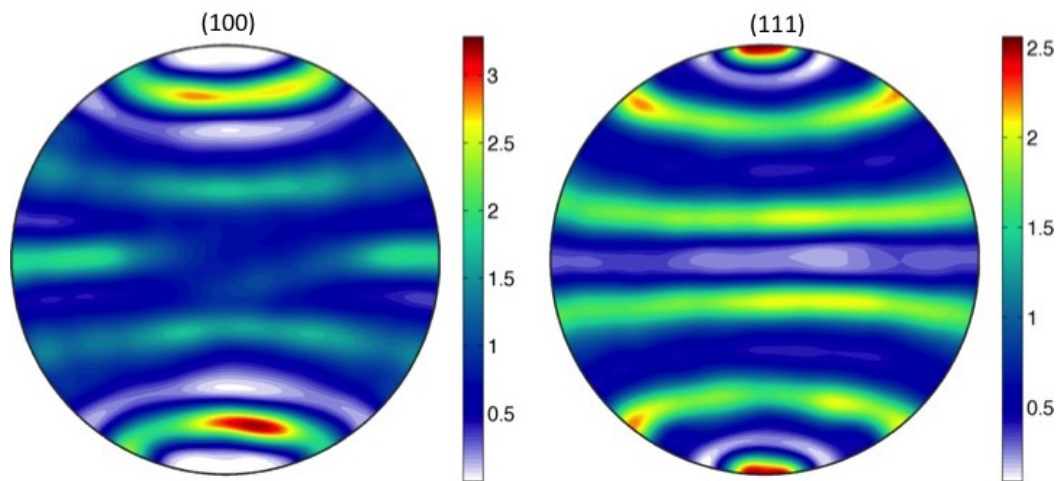
Figure D.32: Simulated (100) and (111) pole figures with 100% PSN
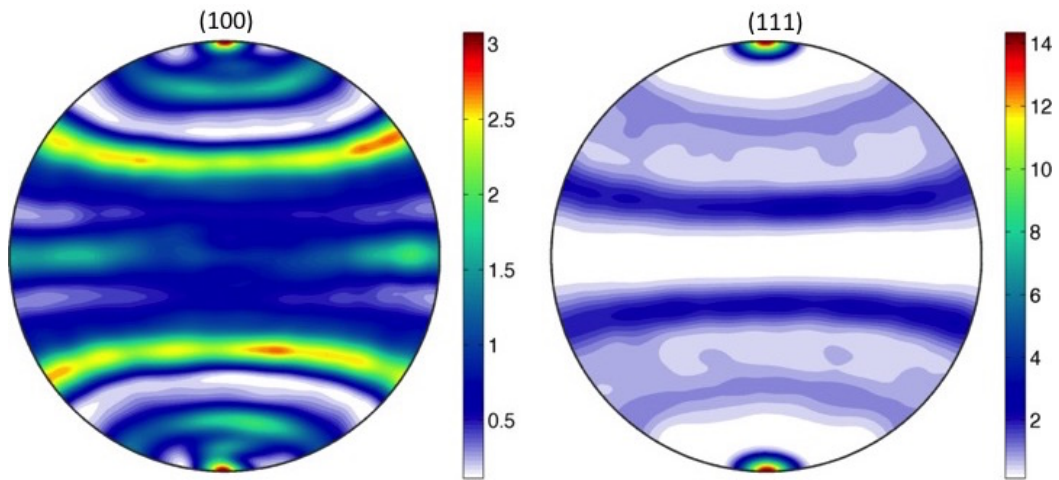
Figure D.33: Simulated (100) and (111) pole figures with 33% cube, 33% GB and 34% PSN
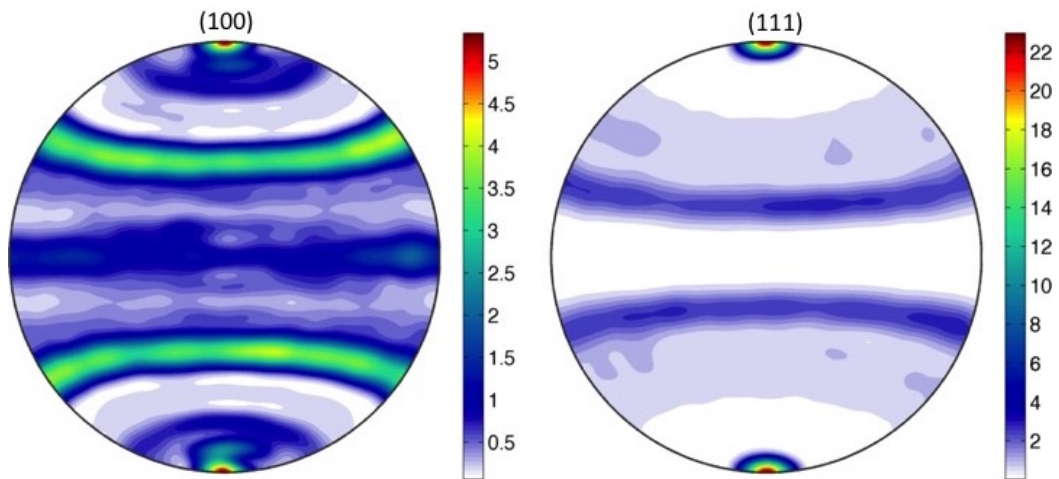
Figure D.34: Simulated (100) and (111) pole figures with 50% cube and 50% GB nucleation
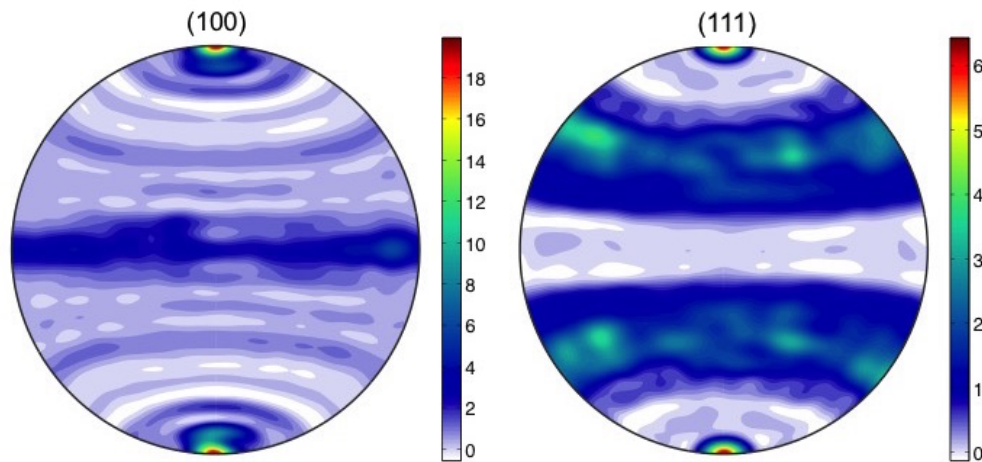
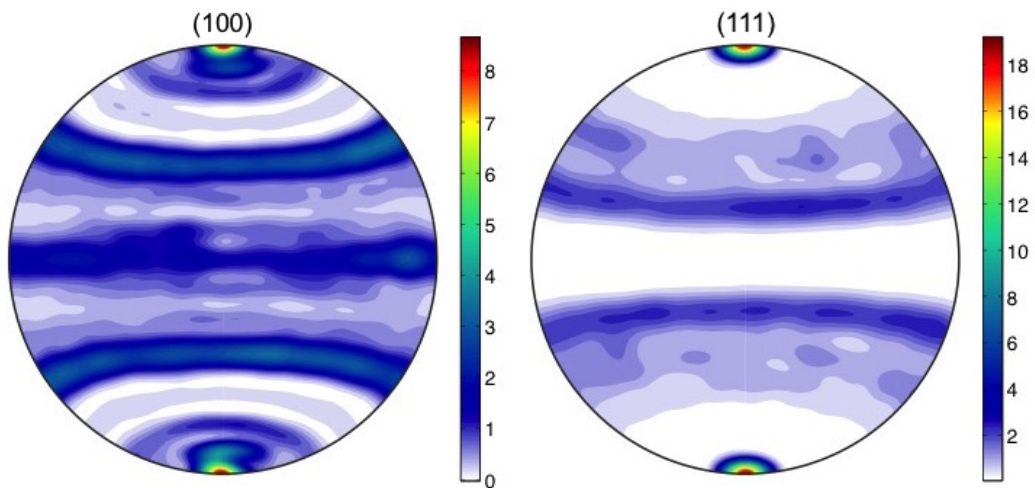**Figure D.35:** Simulated (100) and (111) pole figures with 50% cube and 50% PSN

Figure D.36: Simulated (100) and (111) pole figures with 50% GB and 50% PSN
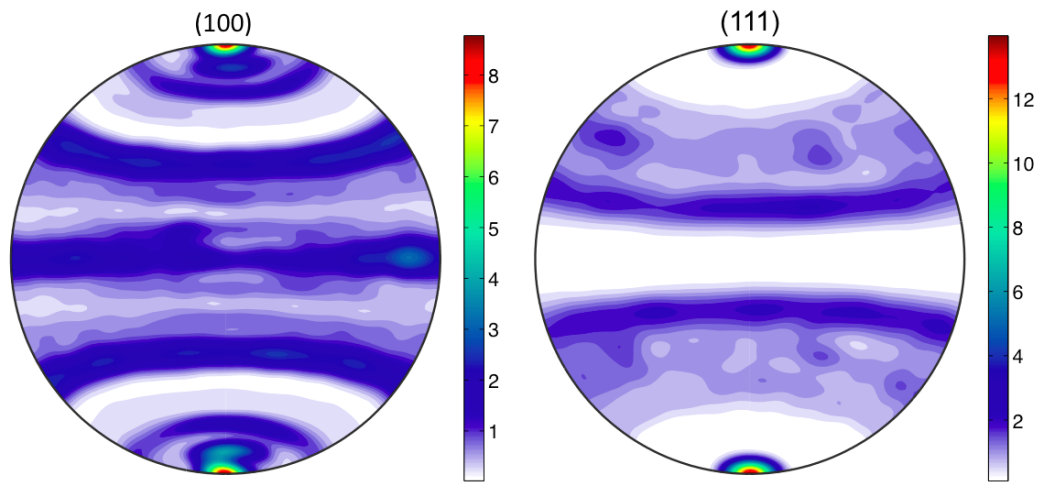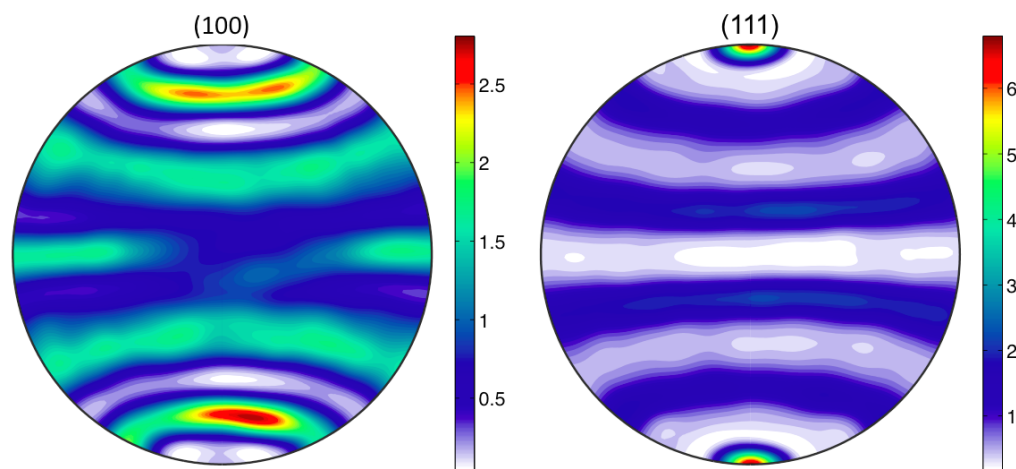
Figure D.37: Simulated (100) and (111) pole figures with weighting factors giving best fit when comparing with B2 (tip)

Figure D.38: Simulated (100) and (111) pole figures with weighting factors giving best fit when comparing with D04 heat treated for 610s at 450°C

Figure D.39: Simulated (100) and (111) pole figures with weigthing factiors giving best fit when comparing with D04 heat treated for 10s at 500°C

Figure D.40: Simulated (100) and (111) pole figures with weighting factors for nucleation mechanisms found in *ALSOFT*